Thesis presented to the Instituto Tecnológico de Aeronáutica, in partial fulfillment of the requirements for the degree of Doctor of Science in the Graduate Program of Physics, Field of Atomic and Molecular Physics.

Claudio Ribeiro da Silva

THEORETICAL STUDY OF ELECTRONIC, OPTICAL, AND THERMODYNAMIC PROPERTIES OF GROUP IIIA SESQUIOXIDES In_2O_3, Ga_2O_3, Al_2O_3, AND THEIR POLYMORPHS

Thesis approved in its final version by signatories below:

gov.br Documento assinado digitalmente
MARCELO MARQUES
Data: 31/05/2025 21:26:25-0300
Verifique em https://validar.iti.gov.br

Prof. Dr. Marcelo Marques

Advisor

gov.br Documento assinado digitalmente
RAIMUNDO NOGUEIRA DA COSTA FILHO
Data: 02/06/2025 10:11:45-0300
Verifique em https://validar.iti.gov.br

Prof. Dr. Raimundo Nogueira da Costa Filho

Co-advisor

Campo Montenegro
São José dos Campos, SP - Brazil
2025

Cataloging-in Publication Data
Documentation and Information Division

da Silva, Claudio Ribeiro
Theoretical study of electronic, optical, and thermodynamic properties of group IIIA sesquioxides In_2O_3, Ga_2O_3, Al_2O_3, and their polymorphs / Claudio Ribeiro da Silva.
São José dos Campos, 2025.
155f.

Thesis of Doctor of Science – Course of Physics. Area of Atomic and Molecular Physics – Instituto Tecnológico de Aeronáutica, 2025. Advisor: Prof. Dr. Marcelo Marques. Co-advisor: Prof. Dr. Raimundo Nogueira da Costa Filho.

1. Semiconductor. 2. Sequioxides. 3. Computational simulation. 4. Computational physics. 5. Properties. I. Instituto Tecnológico de Aeronáutica. II. Title.

BIBLIOGRAPHIC REFERENCE

DA SILVA, Claudio Ribeiro. **Theoretical study of electronic, optical, and thermodynamic properties of group IIIA sesquioxides In_2O_3, Ga_2O_3, Al_2O_3, and their polymorphs**. 2025. 155f. Thesis of Doctor of Science – Instituto Tecnológico de Aeronáutica, São José dos Campos.

CESSION OF RIGHTS

AUTHOR'S NAME: Claudio Ribeiro da Silva
PUBLICATION TITLE: Theoretical study of electronic, optical, and thermodynamic properties of group IIIA sesquioxides In_2O_3, Ga_2O_3, Al_2O_3, and their polymorphs.
PUBLICATION KIND/YEAR: Thesis / 2025

Claudio Ribeiro da Silva
Praça Marechal Eduardo Gomes, 50 - Vila das Acácias
12.228-900 – São José dos Campos–SP

THEORETICAL STUDY OF ELECTRONIC, OPTICAL, AND THERMODYNAMIC PROPERTIES OF GROUP IIIA SESQUIOXIDES In_2O_3, Ga_2O_3, Al_2O_3, AND THEIR POLYMORPHS

Claudio Ribeiro da Silva

Thesis Committee Composition:

Prof. Dr.	Francisco Bolivar Correto Machado	President	-	ITA
Prof. Dr.	Marcelo Marques	Advisor	-	ITA
Prof. Dr.	Raimundo Nogueira da Costa Filho	Co-advisor	-	UFC
Prof. Dr.	Luiz Fernando de Araújo Ferrão	Internal Member	-	ITA
Prof. Dr.	Filipe Matusalém de Souza	Internal Member	-	ITA
Prof. Dr.	Teldo Anderson da Silva Pereira	External Member	-	UFMT
Prof. Dr.	Luiz Tadeu Fernandes Eleno	External Member	-	EEL-USP

ITA

To Débora, for her strength, love, and support in this endeavor. To me, for having managed to get this far.

Acknowledgments

I would like to express my gratitude to my advisor, Professor Marcelo Marques, whose guidance and support have been essential to this research.

I extend my appreciation to Professor Ivan Guilhon for his valuable tips on the usage of VASP, for the Density Functional Theory course, and for his courtesy in many other aspects of daily work; to Professor Lara Teles for the Solid State Physics course and for her assistance in other matters; and to Professors Franciso Machado, André Chaves, and Rene Spada, for their support in handling bureaucratic issues.

I am also grateful to Professor Friedhelm Bechstedt from Institut für Festkörpertheorie und -optik, Friedrich-Schiller-Universität Jena for his guidance, invaluable contributions, and insightful discussions during the writing of the papers that enriched the development of this thesis. Finally, I thank Professor Raymundo Costa from the Federal University of Ceará for accepting the co-advising role, which was a mandatory condition for the grant.

A special thanks goes to my fellow students, both within and outside the research group, whose camaraderie and shared experiences have made this academic journey both fulfilling and enjoyable. In particular, I am grateful to Débora (my loving wife), Túlio, Henrique, Vinícius (USP/Lorena), and Leonardo Fabrício for their support and collaboration.

I extend my thanks to all those who have contributed to the development of this thesis. Lastly, I acknowledge the financial support for this research from the Conselho Nacional de Desenvolvimento Científico e Tecnológico (CNPq) under grant 164765/2021-2.

"I prefer true but imperfect knowledge, even if it leaves much indetermined and unpredictable, to a pretence of exact knowledge that is likely to be false.".
— Friedrich A. Hayek

"If each individual is unique, how else can he be made "equal" to others than by destroying most of what is human in him and reducing human society to the mindless uniformity of the ant heap?".
— Murray N. Rothbard

Resumo

Óxidos semicondutores transparentes e óxidos metálicos isolantes, particularmente semicondutores transparentes de largo e ultra-largo band gap, têm ganhado um interesse acadêmico significativo devido ao seu potencial em tecnologias emergentes. Os principais focos de pesquisa incluem a engenharia do band gap para ajustar as propriedades dos materiais, juntamente com o desempenho e a disponibilidade, que aumentam sua relevância tecnológica.

Este estudo emprega cálculos de primeiros princípios baseados na Teoria do Funcional da Densidade (DFT) para investigar as propriedades estruturais, eletrônicas, ópticas, excitônicas e termodinâmicas dos polimorfos de In_2O_3, Ga_2O_3 e Al_2O_3. Uma limitação conhecida do DFT é a subestimação do band gap, particularmente em semicondutores, o que é ainda mais complicado em Ga_2O_3 e In_2O_3 devido aos níveis d deslocalizados. Correções precisas de quasipartículas, como GW e funcionais híbridos, são computacionalmente caras, restringindo sua aplicação a polimorfos mais simples. Consequentemente, estudos mais abrangentes frequentemente negligenciam aspectos complexos desses materiais.

Para superar os desafios impostos pelo polimorfismo nesses óxidos, é empregada uma combinação de técnicas. Primeiramente, é realizada uma análise dos parâmetros estruturais e de equilíbrio, seguida por cálculos de entalpia para investigar as transições de fase induzidas por pressão. Essa abordagem revela transições de fase previamente não reportadas. Na segunda parte, a técnica DFT+A é utilizada para corrigir as posições relativas dos níveis In $3d$ e Ga $3d$ nos polimorfos de In_2O_3 e Ga_2O_3 ajustando um potencial de auto-energia modificado (V_S) para alinhar com os dados experimentais disponíveis sobre estes níveis. Usando o princípio da transferibilidade, este potencial é então aplicado a polimorfos para os quais ainda não existem dados experimentais disponíveis para os níveis mencionados. Com essa primeira aproximação, a correção de quasipartícula DFT$-1/2$ é aplicada para determinar os band gaps de energia. Combinadas, essas abordagens garantem uma descrição mais precisa não apenas do gap de energia, mas também da estrutura eletrônica. Além disso, as propriedades eletrônicas, ópticas e excitônicas são extraídas e comparadas com cálculos DFT padrão em todos os polimorfos. A partir das propriedades estruturais obtidas na primeira parte,

juntamente com os cálculos de fônons, as propriedades vibracionais dos polimorfos são extraídas, a partir das quais suas estabilidades dinâmicas são inferidas. Da mesma forma, propriedades termodinâmicas importantes, como energia livre total, entropia vibracional e capacidade calorífica a volume constante, são derivadas, assim como suas frequências e temperaturas de Debye. Transições de fase induzidas por temperatura, não identificadas previamente em outros trabalhos, também são observadas.

Finalmente, os resultados são comparados entre diferentes óxidos e estruturas similares para fornecer uma perspectiva mais ampla sobre como a combinação de parâmetros relacionados ao polimorfismo desses materiais governa suas propriedades e serve como base para diversas aplicações.

Abstract

Transparent semiconducting oxides and insulating metal oxides, particularly wide and ultra-wide band gap transparent semiconductors, have gained significant academic interest for their potential in emerging technologies. Key research focuses include band gap engineering to tailor material properties, along with performance and availability, which enhance their technological relevance.

This study employs first-principles calculations based on Density Functional Theory (DFT) to investigate the structural, electronic, optical, excitonic, and thermodynamic properties of In_2O_3, Ga_2O_3, and Al_2O_3 polymorphs. A known limitation of DFT is the underestimation of the band gap, particularly in semiconductors, which is further complicated in Ga_2O_3 and In_2O_3 due to delocalized d levels. Accurate quasiparticle corrections, such as GW and hybrid functionals, are computationally expensive, restricting their application to simpler polymorphs. Consequently, more comprehensive studies often overlook complex aspects of these materials.

To overcome the challenges posed by polymorphism in these oxides, a combination of techniques is employed. Firstly, an analysis of structural and equilibrium parameters is conducted, followed by enthalpy calculations to investigate pressure-induced phase transitions. This approach reveals previously unreported phase transitions. In the second part, the DFT+A technique is used to correct the relative positions of the In $3d$ and Ga $3d$ levels in In_2O_3 and Ga_2O_3 polymorphs by adjusting a modified self-energy potential (V_S) to align with available experimental data. Using the principle of transferability, this potential is then applied to polymorphs for which no experimental data are yet available for the aforementioned levels. With this first approximation, the DFT$-1/2$ quasiparticle correction is applied to determine the energy band gaps. Combined, such approaches ensure an accurate description not only of the energy band gap but also of the electronic structure. Additionally, electronic, optical, and excitonic properties are extracted and compared with standard DFT calculations across all polymorphs. From the structural properties obtained in the first part, together with phonon calculations, the vibrational properties of the polymorphs are extracted, from which their dynamic stabilities are inferred. Similarly, important thermodynamic properties such as total free energy, vibrational entropy, and constant-volume heat

capacity are derived, as well as their frequencies and Debye temperatures. Temperature-induced phase transitions, not previously identified in other works, are also observed.

Finally, the results are compared across different oxides and similar structures to provide a broader perspective on how the combination of parameters related to the polymorphism of these materials governs their properties and serves as a foundation for various applications.

List of Figures

List of Tables

List of Abbreviations and Acronyms

QP	Quasiparticle.
DFT	Density Functional Theory.
PAW	Projector-Augmented Waves.
HF	Hartree-Fock.
KS	Kohn-Sham.
LDA	Local Density Approximation.
GGA	Generalized Gradient Approximation.
PBE	Perdew-Burke-Ernzerhof.
AM05	Armiento-Mattsson 2005.
GW	Green's function G and the screened Coulomb interaction W.
HSE	Heyd-Scuseria-Ernzerhof.
VASP	Vienna *Ab-initio* Package.
XC	Exchange and correlation
TSO	Transparent Semiconducting Oxides.
UWBG	Ultrawide Bandgap.
WBG	Wide Bandgap.
DFT+U	Density Functional Theory + Hubbard parameter.
DFT+A	Density Functional Theory + Amplitude modulation.
DFT$-1/2$	Density Functional Theory -1/2 QP correction.
Al	Aluminium.
In	Indium.
Ga	Gallium.
O	Oxygen.
B	Boron
Tl	Thalium
Nh	Nihonium
GaAs	Gallium Arsenide
AlN	Aluminium Nitride
Al_2O_3	Aluminium Oxide.
In_2O_3	Indium Oxide.

Ga_2O_3	Gallium Oxide.
LED	Light-emitting diode
GaN	Gallium Nitride
UV	Ultraviolet
UVC	Ultraviolet C
UV-vis	Ultraviolet to visible
DUV	Deep Ultraviolet
MOS	Metal Oxide Semiconductor
SQS	Special Quasirandom Structure
W	Watt
kV	Kilovolts
MW	Megawatts
cm	Centimeter
cm^2	Centimeter squared
s	Second
V·s	Volt second
K	Kelvin
NVS	Neuromorphic Vision System
RRAM	Resistive Random Access Memory
4H-SiC	Silicon Carbide four-Stacked with Cubic and Hexagonal Bonds
h-BN	Hexagonal Boron Nitride
GW	Green's function G and screened Coulomb interaction W
DG	Distributed Generation
θ_D	Debye temperature
ω_D	Debye frequency

List of Symbols

T	Temperature
p	Pressure
V	Volume
E_0	Equilibrium energy
V_0	Equilibrium volume
B_0	Bulk modulus
B'	First derivative of the bulk modulus
H	Enthalpy
S	Entropy
G	Gibbs free energy
F	Helmholtz free energy
E_{crit}	Critical electric field
E_g	Energy band gap
μ	Electron mobility
V_s	Electron saturation velocity
V_S	Self-energy potential
A	Amplitude of the self-energy potential
κ_{th}	Thermal conductivity
Å	Angstrom

Contents

1 General Introduction

1.1 Motivation

As the demand for energy-efficient and high-power electronic devices continues to grow (OKUMURA, 2015), the search for and development of wide band gap (WBG) and ultra-wide band gap (UWBG) semiconductor materials have become imperative for advancing technological frontiers and addressing the limitations of conventional semiconductors (TSAO *et al.*, 2018). These limitations arise due to inefficiencies introduced during the sequence of transformations that electricity undergoes in electronic devices, which are carried out by power electronics converters before the electricity can be efficiently utilized (GACHOVSKA; HUDGINS, 2018). A pivotal aspect with profound implications lies in the occurrence of power losses associated with both the conduction and switching of high currents.

In light of these conditions, adopting WBS and UWBS materials becomes imperative, prompting their operation at heightened switching frequencies. The objective is to decrease switching losses while simultaneously enhancing the power density of the converters (GUILLOD *et al.*, 2020). One of the main driving forces behind this argument is the fact that current power distribution systems need to handle voltages on the order of tens of kilovolts (kV) and powers on the order of megawatts (MW) (MAZUMDER *et al.*, 2023). Moreover, considering a law that states the critical electric field (E_{crit}) is directly proportional to the energy band gap (E_g) of the semiconductor, raised to a power of $\gamma = 1.83$ (SLOBODYAN *et al.*, 2022).

Yet another query surfaces: What societal necessity fuels the substantial demand for devices with high power and efficiency? One of the primary explanations lies in the emergence of Distributed Generation (DG), a system in which electricity is generated by numerous small- and medium-sized power plants rather than a few large-capacity ones (JUNIOR; FREITAS, 2022). These plants harness renewable energy sources such as solar radiation, wind, waves, and hydroelectric energy. By adopting DG systems, we not only enhance energy efficiency-avoiding losses caused by long transmission and distribution lines-but also contribute to the reduction of greenhouse gases. This approach offers a

pathway to introduce less environmentally harmful energy sources, addressing the escalating urgency to mitigate climate-related issues (TANG *et al.*, 2022).

Highlighting the essential requirements of advanced materials and strategies in the design and implementation of power systems, the focus is on achieving optimal efficiency and performance through WBS and UWBS. Key requirements encompass electron mobility $\mu \left[\mathrm{cm}^2 \cdot (\mathrm{V} \cdot \mathrm{s})^{-1}\right]$, electron saturation velocity V_s ($\sim 10^7\,\mathrm{cm} \cdot \mathrm{s}^{-1}$), thermal conductivity κ_{th} $\left[\mathrm{W} \cdot (\mathrm{cm} \cdot \mathrm{K})^{-1}\right]$, and critical electric field E_{crit} ($\mathrm{MV} \cdot \mathrm{cm}^{-1}$), which are essentially related to the energy band gap (E_g) (SHI *et al.*,). These materials exhibit significantly larger E_g values than traditional semiconductors such as silicon (Si) and gallium arsenide (GaAs). Generally, their band gaps are above 3.4 eV for WBG and above 4 eV for UWBG (HIGASHIWAKI *et al.*, 2021). This characteristic enables them to operate at higher breakdown voltages and withstand harsher environmental conditions.

From the perspective of materials science, another noteworthy characteristic of this class of materials is their application in optoelectronic devices. This trend began in 1994 with the introduction of the first high-efficiency light-emitting diode (LED) based on gallium nitride (GaN). Such a development marked a revolutionary breakthrough in the lighting and optoelectronics industry, leading to its inventors being awarded the 2014 Nobel Prize in Physics (NAKAMURA; KRAMES, 2013). Typically, WBS emits light in the blue and ultraviolet (UV) spectrum, while UWBS can emit in UVC (200–280 nm). This characteristic makes it appealing for expanding the operational wavelengths of photonic devices beyond the UV–visible (UV–vis) spectrum and opens up possibilities for applications in deep-UV (DUV) optoelectronics, among others (WONG *et al.*,). Further exploration in the literature reveals applications spanning resistive random access memory (RRAM) (WANG *et al.*, 2022), nonvolatile flash memory (KHANDELWAL *et al.*, 2023), optoelectronic synapses (ZHU *et al.*, 2022), and neuromorphic visual systems (NVSs) (LI *et al.*, 2023).

Two of the most important materials of this type are indium oxide ($\mathrm{In_2O_3}$) and gallium oxide ($\mathrm{Ga_2O_3}$), both of which have garnered considerable attention due to their properties that offer significant advantages in various applications, including their wide band gap, which endows them with superior electrical properties, making them particularly well-suited for high-power and high-frequency electronic devices. Besides that, both exhibit optical transparency, rendering them suitable candidates also for optoelectronics (SHI *et al.*,).

On the other hand, aluminum oxide ($\mathrm{Al_2O_3}$) is also essential for electronic devices due to its high dielectric constant, excellent thermal stability, and insulating properties. It serves as a crucial dielectric material in metal-oxide-semiconductor (MOS) devices, acting as gate dielectric layers, capacitors, and integrated circuits, ensuring reliable

performance (CALZOLARO *et al.*, 2022). Additionally, Al_2O_3 is employed for passivation, protecting semiconductor surfaces, and finds applications in sensors and optoelectronic devices, underscoring its versatility and significance in modern electronics (PARK *et al.*, 2021). In the field of optics, amorphous Al_2O_3 also stands out due to its excellent transparency across a wide spectral range, high refractive index, and low optical loss, making it an ideal material for antireflection coatings, optical waveguides, and protective layers in photonic devices (SHI *et al.*, 2018).

Considering the primary characteristics discussed above, a promising strategy for exploring new materials is to exploit the tunability of properties across different polymorphs of these oxides. By inducing controlled polymorphic transitions, the electronic structure can be modified to either widen or narrow the energy band gap, allowing for optimized tailoring of material properties. Moreover, a comprehensive understanding of these parameters is essential for achieving precise control over the gap, enabling systematic adjustments to meet specific technological demands. This approach holds significant potential for advancing materials science and device engineering, as it provides a framework for fine-tuning electronic properties to suit a wide range of applications. However, while gap control is often the primary focus in the context of semiconductors and insulating oxides, it is crucial to recognize that many other properties are of significant interest in emerging applications. A comprehensive understanding and careful identification of these additional parameters are essential for their effective exploitation. By thoroughly characterizing both the energy gap and other relevant material properties, researchers can develop strategies to optimize performance across a broader range of technological applications.

Although the energy band gap is not the sole factor in determining a material's semiconductor properties, given the significance of charge carrier mobility (HUANG *et al.*, 2020), a focused examination of the energy band gaps in commonly used semiconductor materials reveals promising prospects (Table 1.1), which can be strategically tuned for different applications. This is particularly evident within the oxide system comprising In_2O_3, Ga_2O_3, and Al_2O_3. Notably, the stable phases of these three oxides exhibit energy band gaps of approximately 3.1 eV for In_2O_3, 4.6 eV for Ga_2O_3, and 8.6 eV for Al_2O_3 making the diversity in their band gaps opens up new possibilities for a variety of high-performance devices, ranging from energy-efficient electronics to advanced sensors and power systems.

TABLE 1.1 – Comparative analysis of energy band gaps in widely studied materials.

	Commercially available				Research-grade UWBG devices			Group IIIA oxides		
Material	Si	GaAs	4H-SiC	GaN	Diamond	h-BN	AlN	In_2O_3	Ga_2O_3	Al_2O_3
E_g (eV)	1.12	1.42	3.23	3.4	5.5	5.9-6.4	6.2	3.1	4.6	8.6

In contemporary materials science, researchers employ a range of advanced techniques to investigate and exploit material polymorphism. These methodologies enable the systematic examination of the distinct crystalline phases that a solid can assume, with each polymorph exhibiting unique properties. Consequently, this approach facilitates the precise tuning of critical parameters such as band gap, carrier mobility, and optical response (ITO *et al.*, 2012; KNEIß *et al.*, 2019). However, the non-equilibrium growth techniques and specific conditions required to stabilize a desired polymorph can lead to challenges, including unexpected phase transitions or the coexistence of multiple phases, due to the sensitive balance of lattice parameters and thermodynamic factors (WALUKIEWICZ; ZIDE, 2020). Moreover, even when growing single crystals, these methods face technical limitations–such as contamination by atoms like oxygen, carbon, and hydrogen, as well as the need for ultra-high vacuum environments and precise temperature control–which increase the overall cost and complexity of the process (MILISAVLJEVIC; WU, 2020). Therefore, achieving a comprehensive understanding of the critical parameters involved in phase formation–such as the growth temperature or pressure at which a specific polymorph is stable, as determined from phase diagrams–is essential for engineering these semiconductor oxides for advanced device applications.

In this context, employing first-principles calculations provides a viable approach to predicting the properties of oxide polymorphs, thereby enabling the engineering of these materials. The initial step involves understanding the individual electronic structures of different polymorphs and describing their resultant properties, with particular emphasis on the energy band gap. Exploring their polymorphism introduces additional possibilities for tuning electronic and optical behavior. However, the primary technique for *ab-initio* calculations, Density Functional Theory (DFT), has an inherent limitation: a tendency to underestimate the energy band gap (BORLIDO *et al.*, 2019). Additionally, another constraint arises from the delocalization of d levels in gallium (FURTHMÜLLER; BECHSTEDT, 2016) and indium oxides (FUCHS; BECHSTEDT, 2008).

Various approaches have been explored to achieve an accurate depiction of these structures. In principle, advanced calculation techniques like GW (HEDIN, 1965) and hybrid functionals (BECKE, 1993) have the potential to provide the precision required for a more thorough understanding of the electronic structure of these oxides. Nevertheless, the substantial computational expenses associated with applying these methods restrict their applicability to structures with only a few atoms in the unit cell (FRIEDRICH *et al.*,

2012). This is essentially a limiting factor, considering that within the polymorphism of these oxides, unit cells with 10, 20, 40, and up to 160 atoms can be found (RATCLIFF *et al.*, 2022). An alternative strategy involves utilizing scissor operators. However, a notable drawback of this approach is the introduction of a semi-empirical correction. This correction may not comprehensively account for the complex electronic correlations present in specific materials, particularly those characterized by pronounced correlation effects (NADA, b). Additionally, the primary method offering an approximate solution for delocalized levels, DFT+U, also exhibits limitations due to the necessity of semi-empirically determining the U parameter (HIMMETOGLU *et al.*,).

Considering the issues outlined, this study aims to address several fundamental questions, including: (i) how can we offer a prompt and precise characterization of the polymorphism exhibited by these oxides? (ii) which distinctive individual properties of these oxides can be leveraged to tailor their structural and electronic behavior? (iii) how do phase stability and transitions occur among different polymorphs? (iv) what valuable thermodynamic insights can be derived from the phase diagrams of these oxide systems?

The literature has showcased various methods that, in theory, hold the potential to provide solutions to these queries. Ferreira *et al.* introduced a fast and easily applicable method, DFT$-1/2$, to address the underestimation of the semiconductor gap when employing standard DFT calculations (FERREIRA *et al.*, 2008; FERREIRA *et al.*, 2011). Similarly, Ataide *et al* demonstrated the correction of the delocalization issue of the d level in oxides containing shallow levels through the use of DFT+A (ATAIDE *et al.*, 2017). Besides, the understanding of the vibrational properties of a material can provide insights into the thermodynamics of a given system.

1.2 Objective

The primary objective of this work is to investigate the fundamental principles governing the structural and electronic tunability of group 13 (IIIA) semiconductor sesquioxide polymorphs, providing theoretical predictions of their properties through a robust combination of methods.

The secondary objectives are outlined as follows: i) Conduct an in-depth study of the structural, electronic, and optical properties of Ga_2O_3, In_2O_3, and Al_2O_3 polymorphs using quasiparticle approximate correction DFT$-1/2$ (for Al_2O_3) and quasiparticle approximate and semicore level correction using DFT+$A-1/2$ (for Ga_2O_3 and In_2O_3); ii) Present a comprehensive thermodynamic analysis that is essential for understanding the stability and temperature and pressure-induced phase transitions among the polymorphs of each oxide.

1.3 Organization

This introductory chapter provides an overview of the current research landscape that frames this work and offers a concise explanation of the materials studied. The importance of polymorphism in these oxides within the scientific community is emphasized, along with an overview of the current state of research on semiconductor sesquioxides. Furthermore, the challenges and difficulties inherent in achieving a rapid, reproducible, and accurate description of the structural and electronic properties of their polymorphs are discussed. The introduction also delineates the primary and secondary objectives of the work and outlines its structural organization.

The second chapter explores the theoretical foundations of the employed methodologies, providing a comprehensive analysis to equip the reader with a minimal theoretical framework. Within this chapter, discussions encompass the principles of DFT, the DFT$-1/2$ method for approximate quasiparticle correction, and the DFT$+A$ technique to address delocalized d levels. Additionally, the chapter sheds light on the simultaneous correction of the energy band gap and delocalized d levels present in Ga_2O_3 and In_2O_3 through the combined application of both methods.

In Chapter 3, the specific calculation methodology, such as computational parameters employed and the results for individual oxides and their respective polymorphs obtained through DFT$+A-1/2$ (In_2O_3 and Ga_2O_3) and DFT$-1/2$ (Al_2O_3) are presented and compared. The analysis focuses on five polymorphs of In_2O_3, five polymorphs of Ga_2O_3, and twenty four polymorphs of Al_2O_3, examining their structural, electronic, optical, excitonic and vibrational/thermodynamics properties in detail.

Chapter 4 presents a comparative analysis of oxides sharing identical space groups, investigating how variations in cations and crystalline structures lead to significant differences in their properties. This analysis not only explores how factors such as cation size, electronic configuration, and bonding environment influence key properties like band gap, optical, and thermodynamic properties, but also provides insights into the underlying structure–function relationships.

The concluding chapter, Chapter 5, emphasizes the contributions of this study to the existing literature and research on group IIIA sesquioxides. The key findings are concisely summarized, and the discussion explores perspectives and outlines directions for future research.

The final sections include appendices containing specific information about the methodology, and annexes. Annex A provides a list of published/submitted works in periodic journals, while Annex B presents details of participation in scientific events where partial results of this project were shared.

2 Theoretical Background

Much of the conceptual framework underlying this thesis is well-established in the literature. Therefore, this chapter presents a concise overview of the methodologies adopted in this study, while comprehensive mathematical proofs are provided in Appendix A. Methods that are less documented or involve specific nuances requiring further clarification are discussed in greater detail here. The aim is to lay a solid foundation for understanding how the results were obtained.

2.1 First Principles Calculations

The Schrödinger equation is foundational for determining the electronic wavefunctions and corresponding energy eigenvalues within a crystalline lattice. Its solutions provide critical insights into the energy band gaps and overall electronic structure of materials. However, the computational demands of directly solving the many-body Schrödinger equation escalate rapidly with system size, particularly due to the complexities introduced by electron-electron interactions. These many-body challenges render conventional computational approaches impractical for large systems. Density Functional Theory (DFT) reformulates the many-body problem by employing the electron density as the central variable, thereby reducing the computational complexity associated with directly handling many-body wavefunctions. As a first-principles, or "*ab-initio*" approach, DFT derives material properties solely from the fundamental laws of quantum mechanics, without relying on empirical parameters.

2.1.1 Density Functional Theory

The concept behind DFT was first introduced in 1927, when Llewellyn Hilleth Thomas (THOMAS, 1927) and Enrico Fermi (FERMI, 1927) underscored the significance of electron density in many-body problems. Several decades later, Hohenberg and Kohn formulated the foundational theorems of DFT (HOHENBERG; KOHN, 1964), which apply to electron systems subject to an external potential $V(\vec{r})$ and Coulomb interactions. These theorems

assert:

i) The external potential $V(\vec{r})$ felt by the electrons is a unique functional of the electron density $n(\vec{r})$, apart from a trivial additive constant;

ii) The density that minimises the total energy is the exact groundstate density.

Proofs of these assertions are provided in Appendix A. Both results rely on the Born-Oppenheimer approximation, which assumes that atomic nuclei move significantly slower than electrons due to their much larger masses. Consequently, the nuclei can be treated as fixed, while the electrons move rapidly around them. To properly account for the long-range behavior of Coulomb interactions, a functional $G[n(\vec{r})]$ is introduced, which encompasses both the kinetic and exchange-correlation energies. However, despite the validity of the Born-Oppenheimer approximation, an analytical form for $G[n(\vec{r})]$ remains elusive, and only through approximations can these statements be effectively applied (BURKE; WAGNER,). In practice, the Kohn-Sham equations offer a practical method for determining the electron density of a system.

2.1.2 Kohn-Sham equations

Walter Kohn and Lu Jeu Sham introduced a method to solve the Schrödinger equation for interacting many-body systems by transforming it into an equation for non-interacting particles subject to an effective potential (KOHN; SHAM, 1965). The Kohn-Sham equation, analogous to the Schrödinger equation, produces an electron density identical to that of the interacting system. This equation, governed by the effective potential v_{KS}, is expressed as:5

$$\hat{H}_{\mathrm{KS}}\psi_i(\vec{r}) = \left(-\frac{1}{2}\nabla^2 + v_{\mathrm{KS}}[n(\vec{r})]\right)\psi_i(\vec{r}) = \varepsilon_i\psi_i(\vec{r}), \tag{2.1a}$$

where the functions $\psi_i(\vec{r})$ are the eigenfunctions of the Kohn-Sham equation, $\hat{H}_{KS}$ is the Kohn-Sham Hamiltonian, and v_{KS} is the Kohn-Sham effective external potential given by:

$$v_{\mathrm{KS}} = \frac{1}{2}\int \frac{n(\vec{r})n'\vec{r}}{|\vec{r}-\vec{r'}|}d\vec{r} + v_{\mathrm{xc}}[n(\vec{r})] \tag{2.1b}$$

Note that, without loss of generality and also referring to $\hat{H} = \hat{T} + \hat{U} + \hat{V}_{\mathrm{ext}}$, where $\hat{H}$ is the Hamiltonian operator of the system, $\hat{U}$ is the Coulomb interaction and $\hat{T}$ is the total kinetic energy of electrons, and $\hat{V}_{ext}$ is the external potential, the $\hat{H}_{\mathrm{KS}}$ term in Eq. 2.1a can be more explicitly described as:

$$\hat{H}_{\mathrm{KS}} = -\frac{1}{2}\nabla^2 + v_{\mathrm{ext}}(\vec{r}) + v_{\mathrm{H}}(\vec{r}) + v_{\mathrm{xc}}[n(\vec{r})], \tag{2.2}$$

where the first term is related to the kinectic energy, $v_{\text{ext}}(\vec{r})$ is the external potential (usually the nuclei potential), $v_{\text{H}}(\vec{r})$ is called Hartree potential, which describes the classical Coulombic interaction among electrons, and $v_{\text{xc}}(\vec{r})$ is called exchange and correlation potential, which takes into account further quantum effects (see Appendix A).

2.1.2.1 Plane-wave basis

Plane-wave basis is a widely used method in electronic structure calculations, especially in simulations of periodic materials such as crystals (KRESSE; FURTHMüLLER, 1996). This approach expands the Kohn-Sham orbitals as a sum of periodic functions of the form of plane waves given by:

$$\phi_{\vec{G}}(\vec{r}) = e^{i\vec{G}\cdot\vec{r}}, \tag{2.3}$$

where $\vec{G}$ is the reciprocal lattice vector and $\vec{r}$, as usual, is the position in real space. These functions $\phi_{\vec{G}}(\vec{r})$ form an orthonormal basis, allowing the expansion of a wave function $\psi_i(\vec{r})$ as a sum of plane waves such as:

$$\psi_i(\vec{r}) = \sum_{\vec{G}} c_{i,\vec{G}} e^{i\vec{G}\cdot\vec{r}}, \tag{2.4}$$

where $c_{i,\vec{G}}$ are the expansion coefficients that need to be determined.

Such approach offers several advantages. First, it naturally fits periodic systems, allowing for the straightforward application of Bloch's theorem to implement periodic boundary conditions. Second, the plane-wave basis is inherently complete and orthonormal, which simplifies the numerical evaluation of operators like the kinetic energy operator. Additionally, its systematic convergence–achieved by adjusting the energy cutoff–provides a clear path to improving accuracy. Lastly, plane waves work efficiently with Fast Fourier Transform (FFT) algorithms, which can significantly speed up computations in large-scale simulations. Further details about plane-wave basis are found in Appendix A.

2.1.2.2 Bloch's theorem

Bloch's theorem is a fundamental principle in solid-state physics that directly supports the use of plane-wave bases in DFT calculations since it describes the periodicity of a crystal lattice through a function

$$u_{n\vec{k}}(\vec{r} + \vec{R}) = u_{n\vec{k}}(\vec{r}) \tag{2.5}$$

where $\vec{R}$ is any lattice vector and $\vec{k}$ is a vector in the reciprocal space. In other words, it states that in a periodic potential, the electronic wavefunctions can be written as the product of a plane-wave factor and a function with the same periodicity as the crystal lattice. This insight not only justifies the expansion of Kohn-Sham orbitals in terms of plane waves but also facilitates the imposition of periodic boundary conditions via Bloch's theorem. Consequently, the theorem underpins the efficiency and accuracy of using plane-wave bases, as it naturally aligns with the inherent symmetry of crystalline materials, thereby streamlining the computational treatment of electron behavior in DFT simulations. A brief formulation of it is presented in Appendix A.

2.1.2.3 Vienna *Ab initio* Simulation Package

Since the Kohn-Sham equations are solved self-consistently, several software packages, such as VASP (Vienna *Ab initio* Simulation Package), are available. VASP determines the electronic density $n(\vec{r})$ through an iterative and utilizes plane-wave basis sets in conjunction with the Projector Augmented-Wave (PAW) method to model the electronic structure of materials (KRESSE; HAFNER, 1993). Rather than employing traditional pseudopotentials, which approximate the electron-ion interaction by smoothing the core region, the PAW method reconstructs the full all-electron wave function from a smooth pseudo-wave function.

An initial density $n_0(\vec{r})$ is provided, from which the effective potential v_{KS} is calculated. The Kohn-Sham equation is solved for the wave functions $\psi_i(\vec{r})$, and the density $n(\vec{r})$ is recalculated. The process iterates until self-consistency is achieved. The final density is then used to calculate the system's observables (Fig. 2.1).

2.1.2.4 Projector Augmented-Wave Method

Blöchl's Projector Augmented-Wave (PAW) Method explicitly accounts for all electrons in the wave functions. In other words, within the Kohn-Sham framework, the PAW method reconstructs the all-electron wave functions from smooth pseudo wave functions, ensuring an accurate yet efficient treatment of both core and valence electrons (ANDERSEN, 1975; BLÖCHL, 1994; VANDERBILT, 1990; KRESSE; HAFNER, 1994; KRESSE; HAFNER, 1993; KRESSE; FURTHMÜLLER, 1996).

It employs a linear transformation on pseudofunctions to accurately reconstruct the true orbitals within the augmentation regions around atoms. In essence, the method establishes a mapping between the smooth wave functions, $|\tilde{\psi}_{n\mathbf{k}}\rangle$, and the corresponding "all-electron" wave functions, $|\psi_{n\mathbf{k}}\rangle$, through the use of projector operators and corrective terms. The PAW formalism comprises five main components: i) The smooth wave function

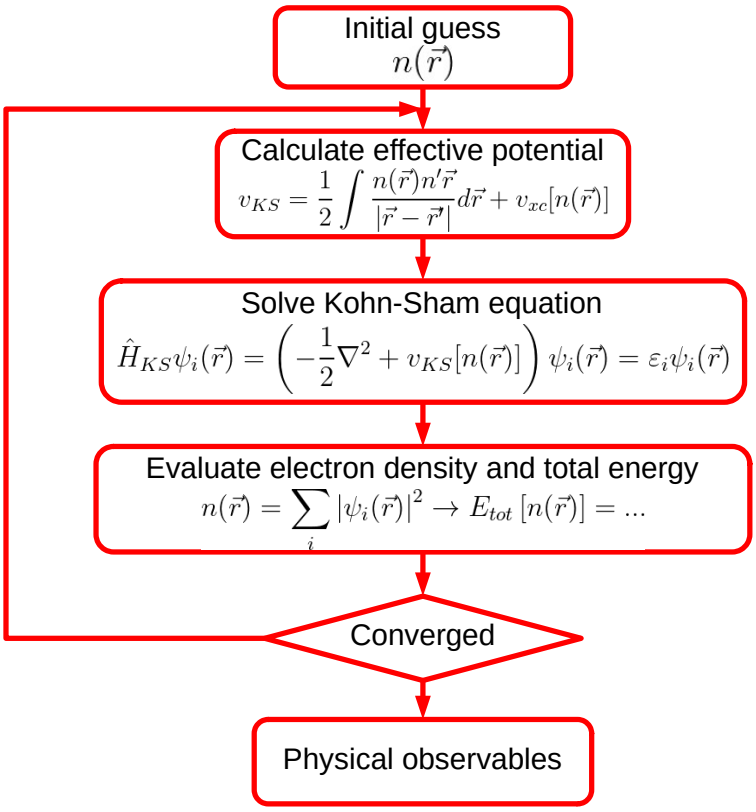

FIGURE 2.1 – Schematic representation of the self-consistency cycle in Kohn-Sham density functional theory calculations.

for valence electrons $|\tilde{\psi}_{n\mathbf{k}}\rangle$; ii) The reconstructed "all-electron" wave function $|\psi_{n\mathbf{k}}\rangle$; iii) Localized basis (partial) functions $|\phi_i\rangle$; iv) Smoothed basis (partial) functions $|\tilde{\phi}_i\rangle$; v) Projection functions $\langle\tilde{p}_i|$. The relationship between the smooth and "all-electron" wave functions is given by:

$$|\psi_{n\mathbf{k}}\rangle = |\tilde{\psi}_{n\mathbf{k}}\rangle + \sum_i \left(|\phi_i\rangle - |\tilde{\phi}_i\rangle\right)\langle\tilde{p}_i|\tilde{\psi}_{n\mathbf{k}}\rangle \tag{2.6}$$

The first term of the summation is the correction that adds the lost oscillations in the smoothed function, and the second term, $\langle\tilde{p}_i|\tilde{\psi}_{n\mathbf{k}}\rangle$, is the projection term of the smoothed wave function. The term $|\psi_{n\mathbf{k}}\rangle$ is the so-called pseudo orbitals, where $n\mathbf{k}$ is the band index and $\mathbf{k}$-point index. This formulation ensures that the rapid oscillations of the wave function near the nucleus are accurately captured, thereby restoring the true nodal behavior that is otherwise smoothed out in pseudopotential methods. The total energy within this framework is typically calculated as

$$E = \sum_n f_n \langle\psi_{n\mathbf{k}}| - \frac{1}{2}\nabla^2 |\psi_{n\mathbf{k}}\rangle + E_{\mathrm{H}}[n] + E_{\mathrm{XC}}[n] + E_{\mathrm{ion}}, \tag{2.7}$$

where f_n are the occupation numbers, $E_{\mathrm{H}}[n]$ represents the Hartree energy accounting for

classical electron-electron repulsion, $E_{\mathrm{XC}}[n]$ is the exchange-correlation energy functional capturing quantum mechanical interactions, and E_{ion} includes the contributions from the ion-ion interactions.

In VASP, the POTCAR file contains the PAW potentials for each element used in a simulation. It stores all the necessary data to reconstruct the all-electron wave functions from the smooth pseudo-wave functions as defined by the PAW method, including the partial waves, their smoothed counterparts, and the corresponding projector functions. Essentially, the POTCAR file is critical for implementing the PAW approach, as it provides the detailed information required to accurately describe the electron-ion interaction. These data allow VASP to reconstruct the "all-electron" wave functions and calculate electronic properties with high accuracy and moderate computational cost (KRESSE; FURTHMüLLER, 1996; BLÖCHL, 1994).

2.1.3 Approximations in Density Functional Theory

In Density Functional Theory (DFT), the exchange and correlation (XC) energy remains an unresolved challenge, necessitating the use of approximations. One widely adopted approach is the Local Density Approximation (LDA), introduced by Kohn and Sham (KOHN; SHAM, 1965). The LDA assumes that the XC energy depends solely on the local electron density, $n(\vec{r})$, thereby treating an inhomogeneous many-body system as if it were locally equivalent to a homogeneous electron gas. Accordingly, the XC energy in the LDA is given by:

$$E_{\mathrm{xc}}^{\mathrm{LDA}}[n(\vec{r})] = \int n(\vec{r})\varepsilon_{\mathrm{xc}}^{\mathrm{LDA}}[n(\vec{r})]d\vec{r}, \tag{2.8}$$

where $E_{\mathrm{xc}}^{LDA}[n(\vec{r})]$ represents the LDA exchange and correlation energy as a function of the electronic density $n(\vec{r})$ at each spatial position $\vec{r}$, and $\varepsilon_{\mathrm{xc}}^{LDA}[n(\vec{r})]$ is the exchange and correlation energy per electron for a homogeneous electron gas. This approximation leads to a systematic error cancellation: while it tends to overestimate the exchange energy, it simultaneously underestimates the correlation energy, often resulting in relatively accurate predictions for many systems (CAPELLE, 2006; BURKE; WAGNER,). However, when the electron density becomes highly inhomogeneous, the assumption of a locally uniform electron gas no longer holds, thereby diminishing the reliability of the LDA in such cases.

In real systems, the electron density $n(\vec{r})$ is inherently inhomogeneous, varying from one region to another. To account for this spatial variation, the Generalized Gradient Approximation (GGA) refines the Local Density Approximation (LDA) by incorporating the gradient of the charge density into the exchange-correlation functional $E_{\mathrm{xc}}[n(\vec{r})]$.

This enhancement leads to improved accuracy for systems with non-uniform electron distributions by taking into account both the local density and its rate of change, as expressed by the following relation:

$$E_{\mathrm{xc}}^{\mathrm{GGA}}[n(\vec{r})] = \int n(\vec{r})\varepsilon_{\mathrm{xc}}^{\mathrm{GGA}}[n(\vec{r}), \nabla n(\vec{r})]d^3r, \tag{2.9}$$

where $E_{xc}^{\mathrm{GGA}}[n(\vec{r})]$ denotes the total XC within the GGA as a function of the electron density $n(\vec{r})$, $\varepsilon_{xc}^{\mathrm{GGA}}[n(\vec{r}), \nabla n(\vec{r})]$ represents the XC energy per electron, which depends on both the density $n(\vec{r})$ and its gradient $\nabla n(\vec{r})$.

The LDA assumes local homogeneity, meaning that the electron density varies only minimally over small regions. While this assumption works reasonably well for systems with nearly uniform densities, it falls short in describing systems with significant density variations–such as molecules, surfaces, and strongly bonded materials. The GGA overcomes these limitations by incorporating the density gradient, thereby capturing spatial variations more effectively. As a result, GGA provides improved predictions for structural properties (including binding energies, molecular geometries, and lattice constants) and total energies. However, it tends to underestimate the band gaps of semiconductors and insulators. Overall, GGA is particularly well-suited for systems with complex electronic structures, as it offers a better description of chemical interactions and more accurate predictions of cohesive energies and formation enthalpies (PERDEW *et al.*, 1996a).

Numerous functionals have been developed for $E_{\mathrm{xc}}^{\mathrm{GGA}}$, each differing in its treatment of the density gradient and its modeling of exchange and correlation effects. Among the most widely used are those based on the works of Perdew and Wang, Perdew, Becke, Lee-Yang-Parr, and the Perdew-Burke-Ernzerhof (PBE) functional. In the context of oxides, where surface phenomena are critical to catalytic processes and chemical reactivity, the AM05 functional (ARMIENTO; MATTSSON, 2005) has demonstrated significant improvements. It effectively captures phenomena such as electric polarization resulting from charge separation between oxygen and metal atoms, thereby combining the strengths of both LDA and GGA/PBE approaches (MATTSSON *et al.*, 2008).

2.2 DFT$-1/2$

To overcome the well-known underestimation of energy band gaps in conventional DFT calculations, various computational approaches have been devised (HEDIN, 1999; BECKE, 1993; PERDEW *et al.*, 1996b; STEPHENS *et al.*, 1994; BECKE, 1988; LEE *et al.*, 1988; COHEN *et al.*, 2008; CROWLEY *et al.*, 2016). Although GW and hybrid functional methods have proven effective, their high computational cost often renders them impractical for

routine applications. The DFT$-1/2$ method, introduced by Ferreira, Marques, and Teles (FERREIRA *et al.*, 2011; FERREIRA *et al.*, 2008), was designed to fill this gap. It is based on the Slater-Janak approximation (SLATER, 1928; JANAK, 1978), where Janak's theorem (HEDIN, 1999) states that the derivative of the total energy $E(N)$ of a system with N electrons with respect to the occupation number f_i of a state α is equal to the Kohn-Sham eigenvalue, such as:

$$\frac{\delta E(N)}{\delta f_\alpha} = \varepsilon_\alpha(f_\alpha) \tag{2.10}$$

For a neutral atom $f_\alpha = 0$ and for a ionized atom $f_\alpha = -1$. Assuming that the eigenvalue depends linearly on the occupation level f_α and considering the midpoint rule, integrating between these two states we have:

$$E(f_\alpha = 0) - E(f_\alpha = -1) = \int_{-1}^{0} \frac{\delta E(N)}{\delta f_\alpha} df_\alpha = \int_{-1}^{0} \varepsilon_\alpha df_\alpha \approxeq \varepsilon_\alpha(-1/2) \tag{2.11}$$

Ferreira *et al* (FERREIRA *et al.*, 2011) demonstrated the physical meaning of the difference between the half-ion eigenvalue $\varepsilon_\alpha(-1/2)$ and the eigenvalue $\varepsilon_\alpha(0)$ at full occupation and provided a self-energy S_α as:

$$\frac{\delta \varepsilon_\alpha}{\delta f_\alpha} = 2S_\alpha \tag{2.12}$$

and a simpler expression for the afforementioned difference as:

$$\varepsilon_\alpha(-1/2) - \varepsilon_\alpha(0) = \int_{0}^{-1/2} \frac{\delta \varepsilon_\alpha}{\delta f_\alpha} = -S_\alpha \tag{2.13}$$

Finally, using Eq.2.13 in Eq.2.11:

$$E(-1) = E(0) - \varepsilon_\alpha(0) + S_\alpha \tag{2.14}$$

Which means that the ionization of electron α requires not only the negative of its eigenvalue energy but also includes the self-energy (FERREIRA *et al.*, 2011).

Note that S_α is the quantum mechanical average of a "self-energy potential" $V_\mathrm{s}(\vec{r})$, of a Kohn-Sham state α with electron density $n_\alpha(\vec{r})$ given by:

$$S_\alpha = \int n_\alpha(\vec{r}) V_\mathrm{s}(\vec{r}) d^3r, \tag{2.15}$$

where $V_\mathrm{s}(\vec{r})$ is the difference between the Kohn-Sham potentials for the ion and the atom.

$$V_\mathrm{s}(\vec{r}) \approx -V(f_\alpha = -1/2, r) + V(f_\alpha = 0, r) \tag{2.16}$$

The atomic potential $V_\mathrm{s}(\vec{r})$ is incorporated into the pseudopotentials as an external potential to facilitate self-consistent calculations. However, this approach is only

applicable to isolated atoms. For crystals, including the long-range atomic potential for all ions would lead to energy divergence when summed over the lattice. This divergence occurs because V_{s} decreases as $1/r$ at large distances. To avoid the penetration of self-energy Coulomb tails into neighboring atomic sites, the self-energy potentials are trimmed using a modified self-energy potential $\widetilde{V}_{\mathrm{s}}$, defined as:

$$\widetilde{V}_{\mathrm{s}} = \Theta(\vec{r})V_{\mathrm{s}}(\vec{r}), \tag{2.17}$$

where $\Theta(\vec{r})$ is a step-like cutting function given by:

$$\Theta(\vec{r}) = \Theta(r) = \begin{cases} A\left[1 - \left(\frac{r}{r_{\mathrm{cut}}}\right)^8\right]^3, & \text{if } r \leq r_{\mathrm{cut}}, \\ 0, & \text{if } r > r_{\mathrm{cut}} \end{cases} \tag{2.18}$$

Typically, for band gap corrections, the parameter A (amplitude) is set to one, as will be discussed in more detail in the next section. The r_{cut} parameter defines the range, in atomic units (a.u.), of the self-energy potential around elements. It is applied to corrections at the VBM and, in some cases, also at the conduction band minimum CBM. This parameter is determined variationally (Fig. 2.2) by identifying the value that maximizes the quasiparticle (QP) energy band gap. $E_{\mathrm{g}}^{\mathrm{QP}}$, as:

$$\frac{\delta E_{\mathrm{g}}^{\mathrm{QP}}}{\delta \widetilde{V}_{\mathrm{s}}(\vec{r})} = 0 \tag{2.19}$$

Thus, without empirical parameters the Kohn-Sham DFT$-1/2$ equation can be solved as:

$$\left[-\frac{1}{2}\nabla^2 + v_{\mathrm{KS}}(\vec{r}) + \widetilde{V}_{\mathrm{s,V}}(\vec{r}) - \widetilde{V}_{\mathrm{s,C}}(\vec{r})\right]\psi_i(\vec{r}) = \varepsilon_i\psi_i(\vec{r}) \tag{2.20}$$

where $\widetilde{V}_{\mathrm{s,V}}(\vec{r})$ or $\widetilde{V}_{\mathrm{s,C}}(\vec{r})$ are the trimmed self-energy potentials of the valence or conduction self-energies. Then, the difference between the eigenvalues $\varepsilon_c - \varepsilon_v$ gives the band gap DFT$-1/2$. And this calculation has the same computational cost as a standard DFT calculation.

Notice that all of this explanation can be simplified by considering that the fundamental band gap E_{g} is defined as the difference between the ionization potential $I(N)$ and the electron affinity $A(N)$, with the removal of the potential corresponding to half an electron.

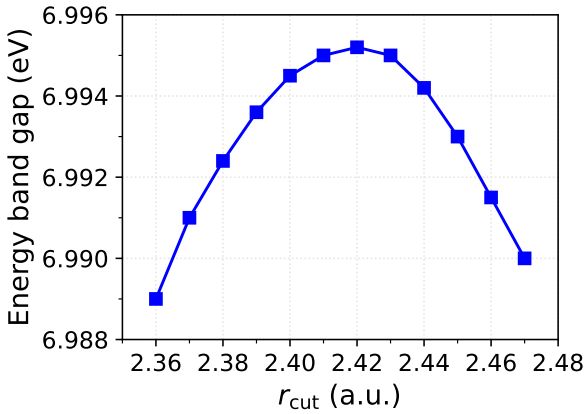

FIGURE 2.2 – Energy band gap as a function of the r_{cut} parameter. The chosen r_{cut} for the quasiparticle correction is the one that provides the maximum band gap value.

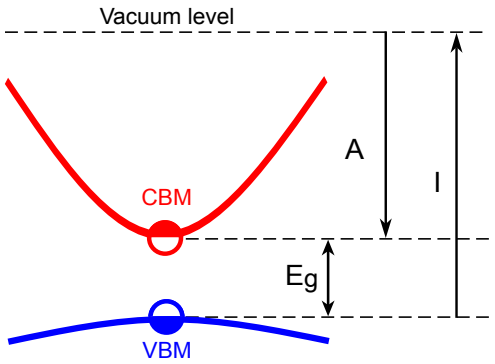

FIGURE 2.3 – Graphical representation of the DFT−1/2 method, showing self-energy corrections applied to the VBM, as used in this study. Half an electron is removed from the VBM to correct the ionization energy exclusively.

2.3 DFT+A

Accurate descriptions of a material's band structure, particularly its band gap, often require including semi-core levels in *ab-initio* calculations (SCHLEIFE *et al.*, 2006), as these levels influence the valence band. However, DFT methods like LDA and GGA struggle with localized electronic states due to limitations in handling the exchange interaction, which describes how electrons avoid overlap based on the Pauli Exclusion Principle. This non-local interaction, influenced by electron screening and material polarization, is poorly represented by local or semi-local functionals. Additionally, DFT methods fail to fully compensate for electrostatic self-interaction, where an electron incorrectly interacts with itself, causing significant errors for localized states. Consequently, these states are overestimated in energy, appearing at higher energies.

This issue is particularly critical for compounds with elements from group IIIA, starting from period 4, such as Ga and In. Semi-core levels in these elements not only affect band dispersion but also increase *pd* interactions with oxygen's 2*p* states (FUCHS;

BECHSTEDT, 2008; FURTHMÜLLER; BECHSTEDT, 2016), enhancing the d-character of the VBM. This exacerbates DFT's intrinsic underestimation of band gaps, yielding less accurate results.

To address these challenges, approaches such as the GW approximation (HEDIN, 1965) and DFT+U (DFT with a Hubbard parameter U) can be utilized (ANISIMOV *et al.*, 1991) or even both combined.

The GW method offers high accuracy but is computationally prohibitive for the systems considered in this work. Alternatively, DFT+U incorporates a correction term (U) to account for the underestimated electron correlation in strongly correlated systems (HIMMETOGLU *et al.*,). However, its systematic application is constrained by specific limitations, including:

i. Selection of the U Parameter: The proper determination of the U parameter is critical and often empirical. The absence of a systematic approach for identifying the optimal U value makes results highly sensitive to this choice;

ii. State Dependence: The value of U can vary depending on the specific electronic state, posing challenges for the universal application of DFT+U across different states and materials;

iii. Lack of Dynamic Treatment: DFT+U employs a static approach to electron correlation correction, failing to fully capture dynamic effects. This limitation becomes significant in systems where electronic dynamics play a crucial role;

iv. Issues with Transition States: The method can encounter challenges in accurately describing transition states, including electron holes and fractional charge states;

v. Sensitivity to Crystal Structure: The performance of DFT+U can be influenced by the choice of the initial crystal structure, which may restrict its applicability in studies involving materials across different phases.

Moreover, combining DFT+U with GW introduces additional complexities that warrant careful consideration. One of the primary concerns is the risk of double counting electronic correlations. DFT+U is designed to correct the local treatment of electron interactions–particularly for localized states such as d or f orbitals–by applying an effective Hubbard U correction. When GW is subsequently employed, it introduces many-body corrections aimed at refining quasiparticle energies. This overlap can inadvertently lead to the same correlation effects being included twice, potentially resulting in an overestimation that affects key properties like band gaps and electronic structures (SAMSONIDZE *et al.*, 2014).

Another significant difficulty stems from the sensitivity of the GW calculations to the choice of the U parameter used in the DFT+U step. Any imprecision or empirical uncertainty in determining U can propagate through the GW correction, thereby amplifying errors and reducing the reliability of the results. Additionally, methodological adjustments are often required because the standard GW formalism is based on certain assumptions regarding the underlying electronic structure. For exemple, GW assumes a quasiparticle picture where many-body effects are treated perturbatively using a one-particle Green's function and a dynamically screened Coulomb interaction, often computed via the random phase approximation (RPA) which neglects vertex corrections (WEN *et al.*, 2024). It also presumes that the starting point (typically from DFT or Hartree-Fock) provides a reasonable approximation to the ground state, with higher-order corrections being negligible (HARSHA *et al.*, 2024).

Thus, incorporating a DFT+U starting point means that the screening and self-energy calculations within the GW framework may need to be reformulated. Such modifications not only increase computational complexity but also add layers of uncertainty regarding the final electronic properties.

Similarly, the DFT+A method aims to achieve a band structure that accurately reflects the corrected position of a specific electronic level, which standard DFT calculations fail to capture. This concept is inherently aligned with the DFT$-1/2$ methodology, which relies on the principle of half-ionization. In the DFT+A approach, the modified potential, $\tilde{V_s}$, is adjusted using a step function defined by two parameters in Eq.2.17: the cutoff radius r_{cut}, which determines the range of the self-energy potential correction, and the amplitude A, which is directly associated with the linear increase in the binding energy of the electronic level (Fig.2.4).

It is important to note that when DFT$-1/2$ is used for gap correction, the parameter A is typically set to one. In other words, for quasiparticle correction, there is no need to determine a specific value for A. However, when correcting for a particular level, this parameter must be determined based on experimental data. Subsequently, by applying the concept of pseudopotential transferability (GOEDECKER; MASCHKE, 1992) (more precisely, the PAWs), the same values can be used for polymorphs for which experimental data is unavailable.

For the second parameter used in DFT+A, Pelá *et al.* (PELÁ *et al.*, 2012) demonstrated that r_{cut} exhibits a linear relationship with atomic charge radii, retaining its atomic character even in solids. This correlation is given by the expression $r_{\text{cut}} = -1.57 + 2.02R$, where R represents 90% of the atomic radius, as derived from fitting (PELÁ *et al.*, 2012).

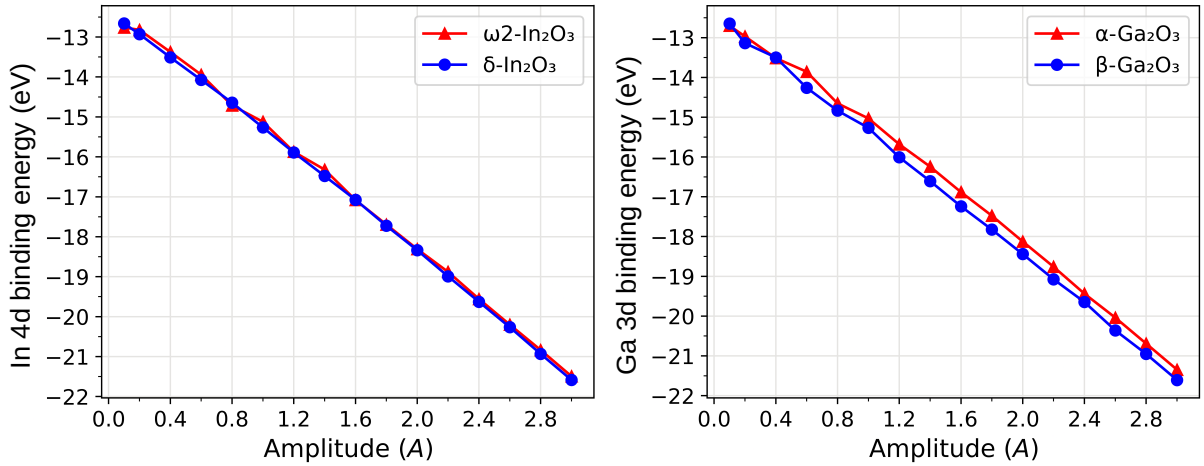

FIGURE 2.4 – Binding energy or relative position of the In $4d$ and Ga $3d$ levels (with respect to the VBM) as a function of the amplitude A parameter (with the Fermi level set to zero). The figure shows the binding energy of two polymorphs of In_2O_3 and two polymorphs of Ga_2O_3 studied in this work.

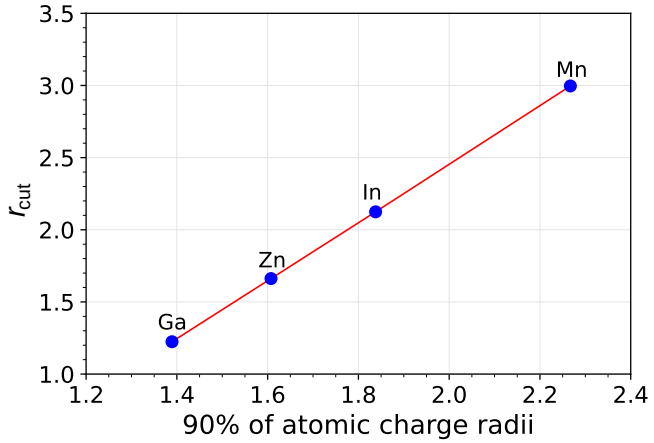

FIGURE 2.5 – Linear behavior of the parameter r_{cut} as a function of the 90% atomic charge radii used in d-level modulation within DFT+A approach. The fitting procedure results in $r_{\text{cut}} = -1.57 + 2.02R$. Adapted and reproduced from (PELÁ *et al.*, 2012).

2.3.1 DFT+$A-1/2$

Ataide *et al.* (ATAIDE *et al.*, 2017) demonstrated that correcting the d-level also affects the band gap. A reduction in the binding energy between the d-level and the VBM, i.e., an increase in their separation, leads to an increase in the band gap. Subsequently, quasiparticle corrections at the VBM result in a more pronounced band gap increase, accompanied by a slight rise in the d-level binding energy (Fig 2.6). Such behavior reinforces the relationship between the localized level and the valence band. It is important to note that defining the d-level binding energy, or its relative position, is only possible through an averaging procedure applied to the density of states for this level, which can be described as follows:

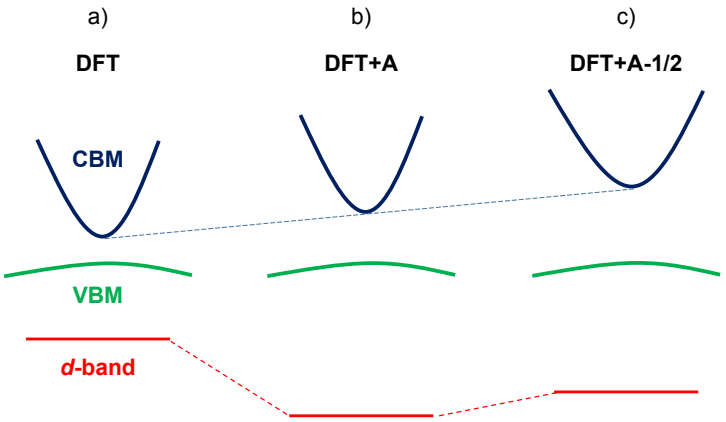

FIGURE 2.6 – Schematic representation of the application of the DFT+$A-1/2$ method, demonstrated in three steps: (a) a standard DFT calculation is performed; (b) the shallow d-level is adjusted to a position slightly below the target value based on experimental data; (c) the quasiparticle correction is applied using DFT$-1/2$ over DFT+A. The complete cycle is referred to as DFT+$A-1/2$.

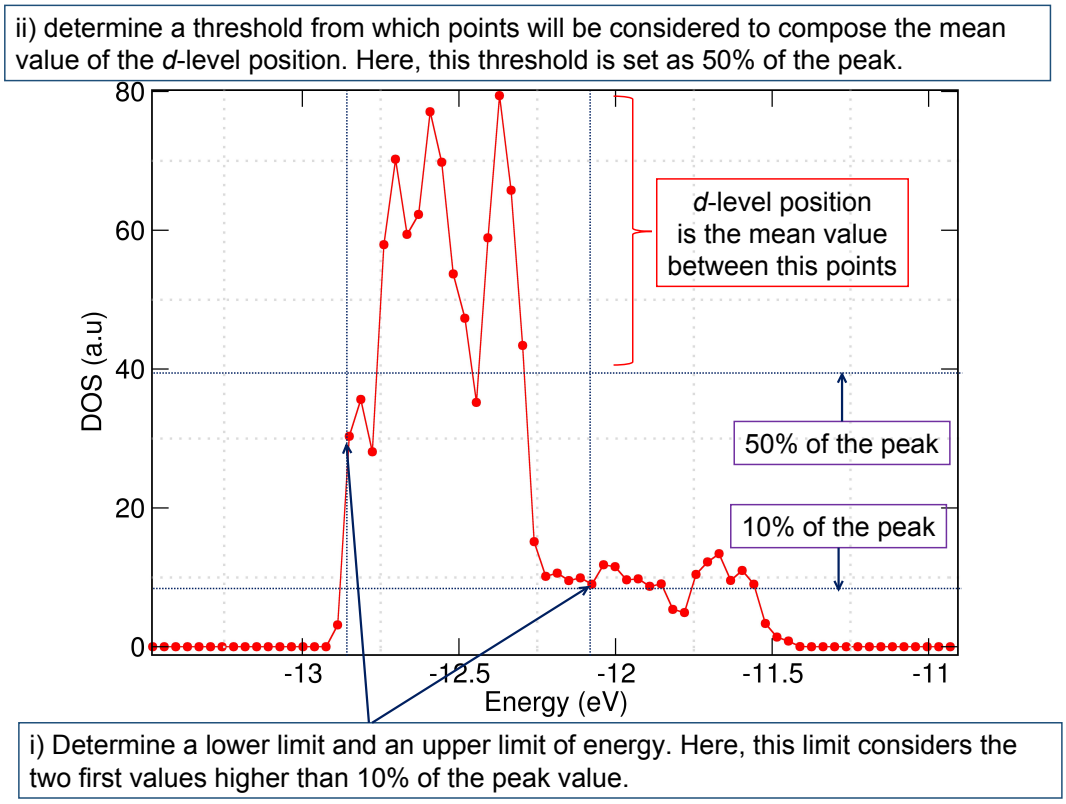

FIGURE 2.7 – Graphical representation of the averaging procedure used to establish a d-level position for its analysis and subsequent adjustment.

i) determine a lower and upper energy limit that defines where the level begins and ends;

ii) determine a threshold from which points will be considered to compose the mean value of the level's position;

iii) calculate the difference between the values obtained in i).

iv) calculate the average value between the points obtained according to the threshold established in ii);

The result obtained in iii) will be considered the average position of the level, and the result obtained in iv) is treated as the deviation from the position. A graphical representation of this procedure is illustrated in Fig 2.7.

In this way, by varying parameter A, the average position of a specific level is adjusted to align with literature values, when available. Subsequently, the QP correction at the VBM (and occasionally at the CBM) yields the final electronic structure, from which the corrected band gap is obtained. Reinforcing the concept of transferability, the same adjusted potential can be applied to other polymorphs of the same chemical species lacking experimental data, underscoring the method's efficiency and simplicity.

2.4 Phonons

Within the framework of quantum mechanics, phonons are bosonic quasiparticles that obey Bose-Einstein statistics (ZIMAN, 2001) and the thermodynamic properties of a solid, such as heat capacity, free energy, and entropy, can be derived from the phonon density of states (DOS) and the partition function. A key quantity governing these properties is the phonon energy dispersion relation, $\omega(\mathbf{q}, s)$, where ω is the phonon frequency, $\mathbf{q}$ is the wavevector, and s denotes the phonon branch.

To establish a connection between the characteristics of phonons and the thermodynamic properties of the system, the phonon density of states (DOS), $D(\omega)$, is introduced as a function of the vibrational frequency ω:

$$D(\omega) = \frac{1}{\hbar} \sum_{j,q} \delta \left[\omega - \omega_j(\mathbf{q})\right] \tag{2.21}$$

In other words, $D(\omega)$ represents the number of vibrational states available within a specific frequency range, where $\omega_j(\mathbf{q})$ denotes the phonon frequency associated with a given wavevector $\mathbf{q}$ and branch j. The Dirac delta function $\delta \left[\omega - \omega_j(\mathbf{q})\right]$ ensures that only the modes corresponding to the selected frequency ω are considered, while the prefactor $1/\hbar$ maintains dimensional consistency, given that the summation runs over discrete states.

In the harmonic approximation, the potential energy of the crystal is expanded up to second order in the atomic displacements, resulting in a set of coupled harmonic oscillators. This expansion leads to a dynamical matrix whose eigenvalues yield the

squared frequencies of the phonon modes, while the eigenvectors provide information about the polarization of these modes. Solving the eigenvalue problem for the dynamical matrix gives direct access to the phonon dispersion relation $\omega(\mathbf{q}, s)$ and underpins many first-principles methods, such as Density Functional Perturbation Theory (DFPT) or Finite Difference Method (FDM), for calculating vibrational properties. Details of how vibrational properties of the lattice to thermodynamical properties are provided in Appendix A.

3 Polymorphs of group IIIA oxides

This chapter presents the results of *ab initio* calculations on the oxides under investigation. The structural, electronic, excitonic, optical, and thermodynamic properties of various polymorphs are examined, along with a detailed overview of the calculation methodology. In addition to results validated by the literature, this chapter presents temperature- and pressure-induced phase transitions between polymorphs that have not yet been reported.

3.1 Introduction

Group IIIA sesquioxides are compounds that combine two atoms of a Group IIIA element with three oxygen atoms. The prefix "sesqui" refers to this 2:3 ratio. This group, also known as Group 13 or the boron family, includes boron (B), aluminum (Al), gallium (Ga), indium (In), thallium (Tl), and nihonium (Nh). These elements possess three valence electrons (ns^2p^1) and have higher ionization energies than Group IA and Group IIA, typically forming 3^+ cations.

This study focuses on the oxides of Al, Ga, and In, excluding others for specific reasons: (i) Nh is synthetic; (ii) Tl compounds are highly toxic; (iii) B behaves uniquely as a semimetal or metalloid, forming covalent bonds and exhibiting high insulating properties, unlike the predominantly ionic bonding in other Group IIIA oxides.

Although Al's most stable oxide exhibits high insulating properties, its bonding is primarily ionic with partial covalent character. The small size and high charge (+3) of the Al^{3+} ion result in a high charge density, allowing it to polarize nearby O^{2-} anions. This polarization induces partial covalent character in the predominantly ionic bond. In contrast, boron forms fully covalent bonds due to its small size and high electronegativity, whereas aluminum exhibits a gradual shift toward metallic behavior, which becomes more pronounced in heavier group elements (HOUSECROFT; SHARPE, 2018).

The filled d subshell in Ga and In, absent in B and Al, leads to distinct atomic properties. For example, although the atomic radius typically increases down the group,

Ga's is slightly smaller than Al's (≈2.33 Å for Ga, ≈2.39 Å for Al) (RAHM *et al.*, 2016). This anomaly arises from *d*-block contraction, where Ga's *d*-electrons poorly shield the nuclear charge, pulling the outer electrons closer (HOUSECROFT; SHARPE, 2018). This effect becomes more significant in heavier elements like In and must be considered when applying quasiparticle corrections to accurately describe the electronic structure of these oxides.

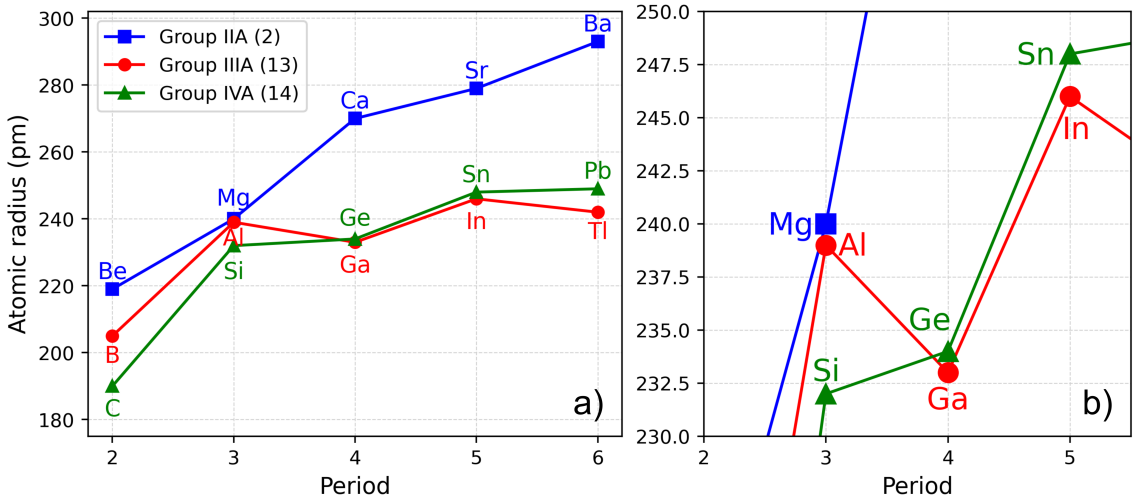

FIGURE 3.1 – Effect of *d*-block contraction on the atomic radius of Group IIIA elements based on *ab initio* calculations (RAHM *et al.*, 2016). (a) Comparison with Groups IIA and IVA; (b) Enlarged view highlighting the inversion in the trend of increasing atomic radius between Groups IIIA and IVA.

3.2 General methodology

Since several techniques were employed to obtain the desired properties, the specific parameters used in each one are listed in the next subsections.

3.2.1 Structural and electronic calculations

All results are based on DFT calculations as implemented in VASP (KRESSE; FURTHMüLLER, 1996; KRESSE; FURTHMÜLLER, 1996). The ground-state calculations, conducted to optimize atomic geometries and explore the total energies of polymorphs, utilized the PBE (PERDEW *et al.*, 1996a) and AM05 (ARMIENTO; MATTSSON, 2005) exchange-correlation (XC) functionals. To provide a more accurate representation of the structures, preference was given to the AM05 functional, as it yielded results that closely aligned with the available experimental data. Notably, this functional is recognized for its precision in determining lattice constants for group III nitrides and oxides

(FURTHMÜLLER; BECHSTEDT, 2016; ATAIDE *et al.*, 2017; CARVALHO *et al.*, 2011). Similarly, in this study, AM05 functional produced band gap values that closely match experimental data reported in the literature (Fig. 3.2).

The electron wave functions were described using the PAW method (BLÖCHL, 1994). The valence electrons include the shallow Ga $3d$ and In $4d$ core electrons. A plane-wave cutoff of 500 eV was chosen for the expansion of the wave functions between the cores for total energy, force, and electronic structure calculations. The atomic relaxations were performed under conditions allowing total energy changes of up to 0.01 meV/atom, with the Hellmann-Feynman forces constrained to be below 10 meV/Å. Monkhorst-Pack meshes were employed for standard **k**-point sampling of the Brillouin zone (BZ).

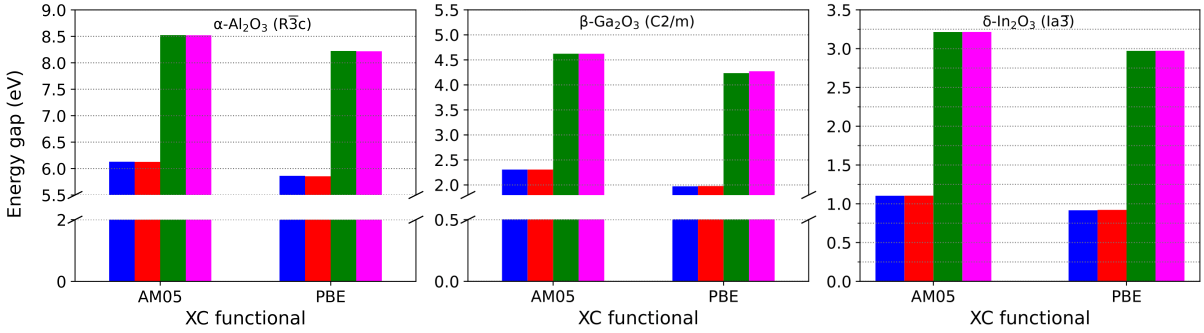

FIGURE 3.2 – Comparison of the PBE and AM05 exchange-correlation functionals and the effect of including SOC for the stable polymorphs of each oxide studied. Blue (red) represents the results without (with) SOC inclusion for standard DFT calculations, and green (magenta) corresponds to the results without (with) SOC inclusion for DFT$-1/2$ (Al_2O_3) and DFT$+A-1/2$ (In_2O_3 and Ga_2O_3) quasiparticle-corrected calculations. The first panel on the left shows the corundum phase of Al_2O_3, the central panel represents the monoclinic phase of Ga_2O_3, and the final panel depicts the bixbyite cubic phase of In_2O_3, with their respective space groups in parentheses.

Initial tests incorporating spin-orbit coupling (SOC) showed a negligible impact on band gaps, with variations of only 0.001 eV (Fig. 3.2). This behavior is consistent with the minimal relativistic effects and the ionic bonding character of the sesquioxides under study. Based on this analysis, SOC calculations were not employed, as this option significantly increases computational time (Fig. 3.3).

In order to deal with the binding energy of shallow core d-electrons in the case of In_2O_3 and Ga_2O_3, the DFT$+A$ approach was adopted (ATAIDE *et al.*, 2017), and band gap corrections were implemented using the standard DFT$-1/2$ method (FERREIRA *et al.*, 2008; FERREIRA *et al.*, 2011). More technical or specific details of the methodology employed for each oxide or polymorph are presented in their respective sections.

The behavior of the total energy, $E = E(V)$, as a function of volume, V, was analyzed using a fitting procedure based on four equations of state (EOS): Birch, Murnaghan, Birch-

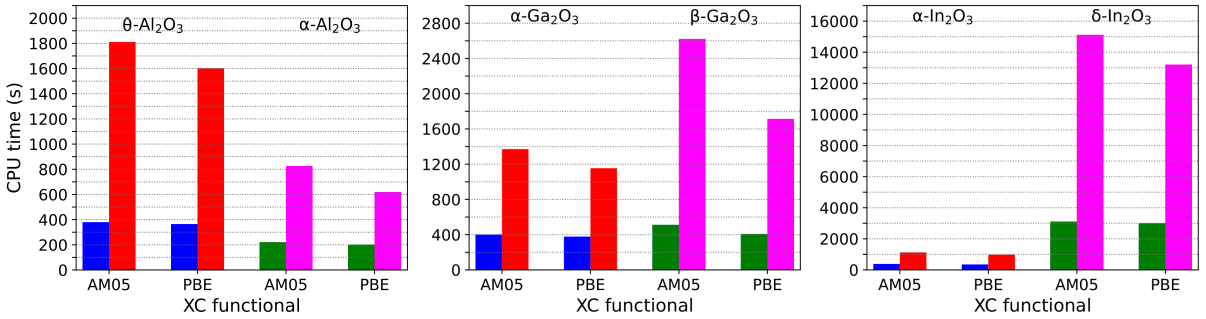

FIGURE 3.3 – Comparison of the total calculation time (in seconds) required for ionic relaxation to reach convergence, both with and without the inclusion of SOC, for the PBE and AM05 functionals applied to different polymorphs of the analyzed oxides. In each panel, a metastable polymorph is represented on the left, with blue bars (without SOC) and red bars (with SOC) alongside the stable polymorph of each oxide, represented by green bars (without SOC) and magenta bars (with SOC). From left to right, the results correspond to the polymorphs of Al_2O_3, Ga_2O_3, and In_2O_3, respectively.

Murnaghan, and Vinet. These were employed to determine the equilibrium volume, V_0, energy, $E_0 = E(V_0)$, isothermal bulk modulus, B_0, and its pressure derivative, B_0'. The Vinet EOS was exclusively adopted in all cases due to its superior ability to accurately describe the volume-energy relationship, particularly at high pressures, where it more effectively captures the material's behavior (VINET *et al.*, 1987; LATIMER *et al.*, 2018), given the consistency of the results and for the sake of simplicity.

3.2.2 Enthalpy calculations

By defining the hydrostatic pressure as $p = -\frac{d}{dV}E(V)$, the results of the fitting procedure using the EOS, which describes energy as a function of volume, enable the expression of the enthalpy H of a given polymorph as a function of pressure p using the relation $H(p) = E + pV$, where E is the equilibrium internal energy and V is the equilibrium volume of the system. The derivation of this relation is provided in the Appendix B.

To directly visualize the transition pressures, the electronic contribution to the enthalpy $H = H(p)$ as a function of hydrostatic pressure p is used. The crossing points of the $H(p)$ curves of different polymorphs mark the conditions where phase stability shifts, indicating pressure-induced structural transformations.

3.2.3 Phonon calculations

Lattice vibrations were investigated using the finite difference method (FDM) (PARLINSKI *et al.*, 1997), as implemented in the PHONOPY (TOGO, 2023; TOGO *et al.*,

2023) package within the VASP framework. To minimize edge effects and accurately capture the crystal structure, supercells with lattice parameters between 10 and 15 Åwere constructed, with atomic displacements of 0.01 Å. The computed total energies were used to construct the system's dynamical matrix, from which the second derivatives of energy with respect to atomic positions were obtained. These derivatives, representing the interatomic force constants, form the basis of the force-constant approach (KRESSE *et al.*, 1995) to phonon calculations. By solving the eigenvalue problem of the dynamical matrix, phonon modes, their frequencies, and the phonon density of states (DOS) were determined, providing direct insights into phonon behavior and thermodynamic properties.

The non-analytical contribution to the dynamical matrix (BARONI *et al.*, 2001), arising from the long-range electric field due to dipole formation between cations and anions, was not considered. Consequently, the splitting between longitudinal optical (LO) and transverse optical (TO) phonon modes was omitted, primarily affecting phonon frequencies in polar materials at long wavelengths ($q \to 0$), where Coulomb interactions dominate. However, neglecting this contribution reduces the computational cost by avoiding explicit Born effective charge (BORN; HUANG, 1988) and dielectric tensor calculations, while also preventing numerical ambiguities in phonon dispersion interpolation. Moreover, for thermodynamic calculations such as heat capacity and entropy, the phonon DOS is more relevant than the LO-TO splitting, making this approximation reasonable for Brillouin zone integration.

3.2.4 Optical and excitonic properties calculations

The optical properties of the material were calculated using the Independent Particle Approximation (IPA) within the Random Phase Approximation (RPA) (GAJDOŠ *et al.*, 2006), as implemented in the VASP code. The calculations were performed by enabling the `LOPTICS = .TRUE.` tag, which computes the dielectric response based on electronic transitions described by Kohn-Sham wavefunctions from DFT. This approach assumes independent electronic excitations, neglecting quasiparticle and excitonic effects. From the dielectric function $\varepsilon(\omega)$, derived from the material's linear response to electromagnetic radiation, several optical properties were extracted, including the real and imaginary parts of the dielectric tensor, optical absorption, and the energy loss function. For a broader analysis, results from the IPA/RPA approach were compared with those from the independent quasiparticle (QP) approach within DFT+$A-1/2$, which incorporates QP effects but excludes excitonic interactions over a wide spectral range.

As will be discussed in the sections on the electronic structures of oxides, the valence band generally exhibits relatively low energy dispersion within the bandgap region due

to weak overlap of atomic orbitals. This characteristic hinders the precise determination of hole effective masses, leading to higher values, as the effective mass is inversely proportional to the band curvature. Consequently, this affects the calculation of the bound state of excitons formed by electron-hole pairs. To determine the exciton binding energy E_b and the excitonic Bohr radius r_B of these oxides, the Wannier-Mott model was adopted (BECHSTEDT, 2014). In cases where the hole mass is significantly larger than the electron mass, this model assumes that the internal motion of the exciton can be described as the movement of the electron around the hole. Moreover, within the effective medium approximation, a large, single optical dielectric constant $\varepsilon \approx \varepsilon_\infty$ accounts for the background effect of the host material. In this hydrogen-like quasiparticle model, only the electron mass is considered, and the exciton binding energy E_b is given by:

$$E_b = \frac{R_H m^*}{m_e \varepsilon_\infty^2}, \tag{3.1}$$

where $R_H = 13.605$ eV is the hydrogen Rydberg constant, m^* is the average electron effective mass relative to the electron rest mass, $m_e = 9.109 \times 10^{-31}$ kg, and ε_∞ is obtained from the real part of the dielectric function, $\mathrm{Re}\,\varepsilon(\omega)$, extracted from the optical properties calculations. Similarly, the excitonic Bohr radius was calculated using the following relation:

$$r_B = \frac{a_B \varepsilon_\infty}{m^*}, \tag{3.2}$$

where $a_B = 0.529$ Å is the Bohr radius.

3.3 Indium oxide porlymorphs

Indium oxide exhibits a rich polymorphism that significantly influences its physical and chemical properties. Such polymorphism is fundamentally linked to variations in its crystalline structure, particularly in the arrangement of the oxygen sublattice and the coordination of indium atoms. In the literature is found that, under ambient conditions, the cubic bixbyite structure is the most prevalent (SPENCER *et al.*, 2022), where indium atoms reside in a distorted octahedral environment coordinated by oxygen atoms. This structure is characterized by a complex oxygen framework that can accommodate intrinsic defects such as oxygen vacancies, which have a notable impact on the material's electronic and optical properties.

In addition to the cubic phase, a rhombohedral form of In_2O_3 has been reported under certain synthesis conditions (SPENCER *et al.*, 2022). In the rhombohedral phase, the symmetry is reduced compared to the cubic bixbyite structure, resulting in distinct atomic positions and slightly different bond lengths and angles. These subtle structural modifications can lead to variations in properties such as band gap and conductivity.

In this study, we investigate the structural, electronic, optical, and thermodynamic properties of five In_2O_3 polymorphs: the stable cubic bixbyite phase (δ-In_2O_3), the metastable corundum-type rhombohedral/hexagonal phase (α-In_2O_3, also known as rh-In_2O_3), and three metastable orthorhombic phases (ω1-, ω2-, and ω3-In_2O_3). Table 3.1 summarizes the structural information related to symmetry, and Figure 3.4 illustrates the complexity of the cells employed in this study. For the α and δ polymorph, both primitive and non-primitive cells are used.

TABLE 3.1 – General information of In_2O_3 polymorphs. In the α and δ cases, primitive (10 and 40 atoms) and non-primitive (30 and 80 atoms) unit cells are provided, respectively.

Polymorph	Crystal system	Structure / name or model	Space group	Atoms per unit cell
α-In_2O_3	Rhombohedral	Corundum	R$\bar{3}c$	10/30
δ-In_2O_3	Cubic	Bixbyite	Ia$\bar{3}$	40/80
ω1-In_2O_3	Orthorhombic	Rh_2O_3 (II)	Pbcn	20
ω2-In_2O_3	Orthorhombic	U_2S_3	Pnma	20
ω3-In_2O_3	Orthorhombic	Enstatite	Pbca	40

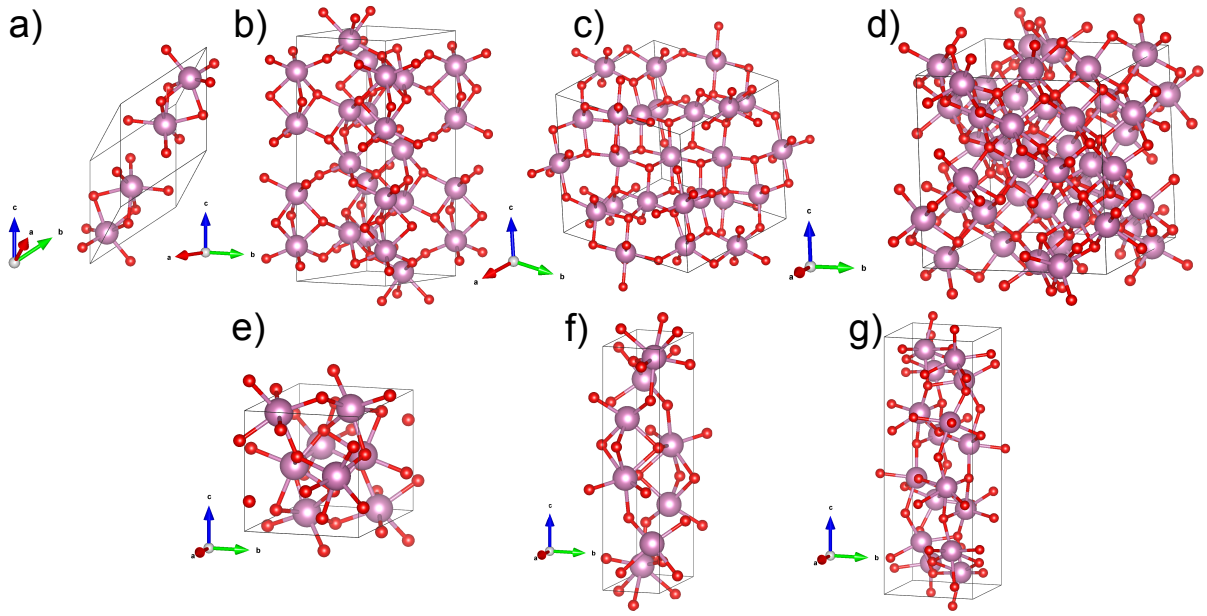

FIGURE 3.4 – Structural representations of In_2O_3 polymorphs: (a) α-In_2O_3, trigonal (rhombohedral) primitive 10-atom unit cell (R$\bar{3}$c); (b) its hexagonal counterpart with 30 atoms (R$\bar{3}$c); (c) δ-In_2O_3, cubic bixbyite 40-atom unit cell (Ia$\bar{3}$); (d) the 80-atom alternative cell of the cubic bixbyite (Ia$\bar{3}$); (e) ω1-In_2O_3, 20-atom orthorhombic phase (Pbcn); (f) ω2-In_2O_3, orthorhombic phase with 20 atoms (Pnma); and (g) ω3-In_2O_3, orthorhombic variant with 40 atoms (Pbca). The In atoms are shown in purple, and the O atoms in red.

The primitive cell of α-In_2O_3 adopts a trigonal (rhombohedral) structure containing 10 atoms, representing the minimal repeating unit required to fully describe the crystal symmetry. This cell is defined within the R$\bar{3}$c space group, which is characterized by

threefold rotational symmetry combined with inversion symmetry. Consequently, this trigonal primitive cell constitutes the most fundamental unit of the crystal lattice, from which the entire structure can be generated via translational symmetry operations. Alternatively, the structure can also be described using a hexagonal representation containing 30 atoms. This hexagonal cell is a multiple of the primitive unit and is typically chosen to better visualize the crystal symmetry and facilitate comparisons with related hexagonal structures.

Similarly, the δ-phase is described using unit cells containing either 40 or 80 atoms, reflecting different choices in crystallographic representation. A 40-atom unit cell represents the fundamental repeating unit that preserves the essential symmetry and structural features of the phase. Its structure arises from a more complex arrangement of the indium and oxygen sublattices, often associated with ordered oxygen vacancies or distortions that necessitate a larger 80-atoms unit cell to fully capture the system's periodicity. In the case of the orthorhombic phases, only primitive cells were considered.

3.3.1 In_2O_3 - Structural properties

The atomic coordinates and lattice constants for the polymorphs were obtained by minimizing the total energy (E) and atomic forces. Table 3.2 summarizes the structural parameters of the five polymorphs, including both primitive and non-primitive cells for the α- and δ-phases. Ensuring the accuracy and reliability of the calculations starts with comparing the obtained results against available experimental data or well-established theoretical calculations from the literature. The results presented align well with experimental data and other calculated results.

TABLE 3.2 – Lattice constants (a, b, and c) in Å and mutual angles (α, β, and γ) in degrees (°) for the In_2O_3 polymorphs. For the α and δ phases, both primitive and non-primitive (np) unit cells are presented. In the reference values, experimental results are marked with (*), while theoretical calculations are indicated with (†).

	Lattice constants (Å)						Angles (°)		
	This work			Reference			This work		
Polymorph	a	b	c	a	b	c	α	β	γ
α-In_2O_3	5.735	5.735	5.735				58.95	58.95	58.95
α-In_2O_3 (np)	5.516	5.516	14.597	5.478	5.478	14.51[a*]	90.00	90.00	120.00
δ-In_2O_3	8.816	8.816	8.816				109.47	109.47	109.47
δ-In_2O_3 (np)	10.181	10.181	10.181	10.118	10.118	10.118[a*]	90.00	90.00	90.00
ω1-In_2O_3	7.976	5.529	5.621	7.929	5.482	5.597[a*]	90.00	90.00	90.00
ω2-In_2O_3	5.721	3.171	12.132	5.473[†]	3.003[†]	11.618[†]	90.00	90.00	90.00
ω3-In_2O_3	5.525	5.716	15.956	5.433	5.569	15.626[b†]	90.00	90.00	90.00

[a](SPENCER *et al.*, 2022), [b](GARCíA-DOMENE *et al.*, 2014).

3.3.2 In_2O_3 - Stability and equilibrium parameters

The curves shown in Fig.3.5 for $E(V)$ confirm that In_2O_3 crystallizes in the cubic bixbyite structure under ambient conditions, consistent with well-established results. In contrast, the $\omega 2$ phase is considerably less stable than the other polymorphs, suggesting that it may represent an intermediate phase between two other phases. Indeed, the transformation from one phase to another can involve the formation of metastable intermediate phases that provide lower-energy pathways for the transition. The ordering of the δ, α, $\omega 3$, $\omega 1$, and $\omega 2$ phases at the lowest energies, $E_0 = E(V_0)$, is directly related to their equilibrium volumes, V_0, as shown in Tab.3.3.

TABLE 3.3 – Equilibrium parameters of In_2O_3 polymorphs, normalized per formula unit, calculated using the Vinet EOS. The equilibrium energy E_0 (in eV/f.u.), equilibrium volume V_0 (in Å^3), bulk modulus B_0 (in GPa), and bulk modulus derivative B_0' are listed.

Polymorph	$-E_0$ (eV/f.u.)	V_0 (Å^3/f.u.)	B_0 (GPa)	B_0'
α-In_2O_3	28.56	64.31	169.68	4.41
δ-In_2O_3	28.69	66.09	161.23	4.70
$\omega 1$-In_2O_3	28.47	62.12	175.16	4.47
$\omega 2$-In_2O_3	27.58	59.66	175.25	4.69
$\omega 3$-In_2O_3	28.50	63.12	168.72	4.61

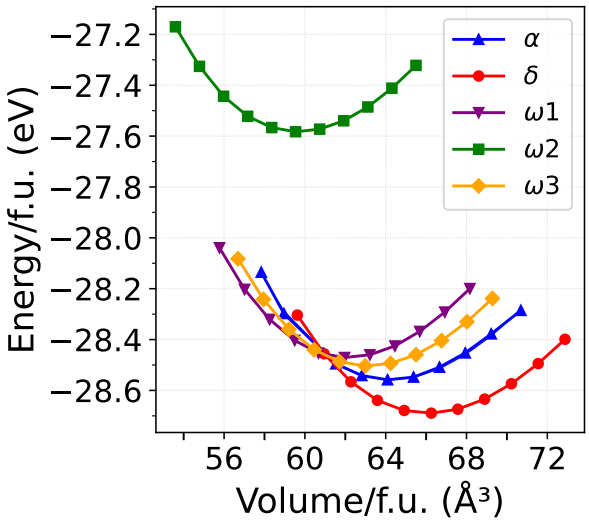

FIGURE 3.5 – Normalized total energy versus volume per formula unit of In_2O_3 for the five polymorphs under consideration.

3.3.3 In_2O_3 - Pressure-induced phase transitions

The enthalpies, H, were analyzed using a thermodynamic model to investigate pressure-induced phase transitions among polymorphs, based on data from the Vinet

EOS. The derivation of the enthalpy expression as a function of pressure, $H = H(p)$, is provided in Appendix B, Section B.3. Phase transitions were analyzed by examining enthalpy differences, $\Delta H(p) = H(p) - H_\delta(p)$, where $H_\delta(p)$ represents the enthalpy of the stable phase δ under standard temperature and pressure conditions. This representation, based on enthalpy variations, allows for the direct observation of pressure-induced phase transitions at specific pressures.

From this analysis, important phase transitions can be identified, as indicated by the arrows and labeled with letters in Fig. 3.6: (i) δ to α at $p_t \approx 10.0$ GPa, labeled as "a"; (ii) δ to $\omega 1$ at $p_t \approx 8.0$ GPa, labeled as "b"; (iii) δ to $\omega 3$ at $p_t \approx 8.5$ GPa, labeled as "d"; (iv) δ to $\omega 2$ at $p_t \approx 22.5$ GPa, labeled as "c"; (v) α to $\omega 1$ at $p_t \approx 6.5$ GPa, labeled as "f"; and (vi) α to $\omega 3$ at $p_t \approx 7.0$ GPa, labeled as "e". Earlier studies reported the $\omega 3$ phase as most

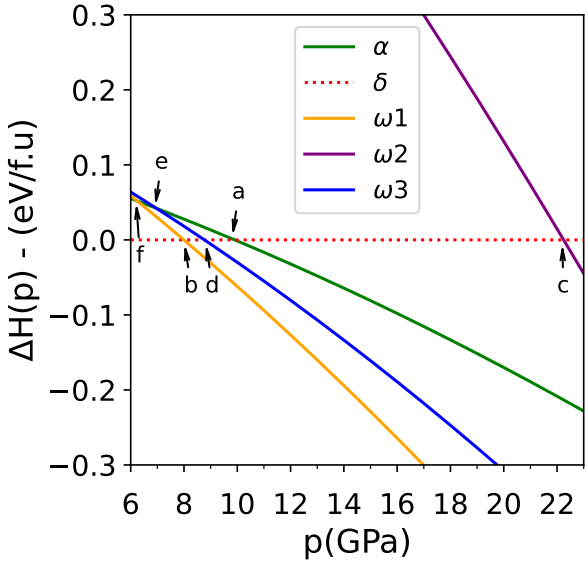

FIGURE 3.6 – Enthalpy per formula unit of In_2O_3 as a function of hydrostatic pressure for the five polymorphs under consideration. The arrows labeled "a" to "f" indicate the phase transitions between two polymorphs.

stable at 8 GPa, whereas our study identifies it at 8.5 GPa. Similarly, the $\omega 1$ phase is the closest in stability to the stable phase at 6.5 GPa. Despite these slight differences, both studies agree that an orthorhombic phase stabilizes below 9 GPa (GARCíA-DOMENE *et al.*, 2014)–a result not solely predicted by its E_0 energy. Moreover, our findings regarding the α phase transition align with previous studies, which reported it at 9 GPa (BEKHEET *et al.*, 2013); here, it appears at 10 GPa.

Nonetheless, both results deviate from experimental data, suggesting that the transition may require substantial energy to break bonds and reorganize atoms. In chemical kinetics, this corresponds to an activation energy barrier that must be overcome. Importantly, the barrier is determined not by the energy difference between the initial and final states, but by the energy required to reach the activated state.

Consequently, even if the final state is more stable, a high kinetic barrier may prevent the transformation unless extra energy is supplied, implying that the process may occur with increased thermal energy during slow transitions (HOUSECROFT; SHARPE, 2018).

3.3.4 In_2O_3 - Electronic structure

The critical parameters of the DFT+$A-1/2$ scheme, specifically the amplitude A and the cutoff radius r_{cut}, are examined in greater detail to accurately determine the quasiparticle self-energy potential, V_{s}. This analysis focuses on the fundamental gap and the d-level position of the equilibrium phase δ-In_2O_3. As is customary in QP self-energy correction calculations, the process begins with a standard DFT calculation.

A direct comparison between the band gaps and the average position of the In $4d$ level obtained from the standard DFT calculation and the experimental reference values reported in the literature reveals that both are underestimated. Therefore, the first step in obtaining an accurate electronic structure is to adjust and correct the localized d level.

3.3.4.1 In_2O_3 - d-level position

By analyzing the densities of states using the procedure for calculating the average position described in Sec.2.3.1, two main conclusions can be drawn. First, the d-derived occupied bands exhibit bandwidths of less than 1 eV. Second, as anticipated, the In $4d$ levels are delocalized by approximately 2 eV in terms of binding energy. By modulating the amplitude of the A level, it was possible to adjust the average position of the $4d$ bands, aligning them with experimental data. This adjustment shifted the average position from approximately 12.5 eV, as reported in (KING *et al.*, 2009), to around 14.6 eV (Tab.3.4).

Furthermore, leveraging the transferability of pseudopotentials (GOEDECKER; MASCHKE, 1992), the same parameters were applied to polymorphs for which no experimental data are currently available in the literature. This methodology facilitated the adjustment of energy levels, resulting in slight variations in the VBM O $2p$ states, which, in turn, directly influence the final band gap. A direct comparison of the results is illustrated in Fig. 3.7.

3.3.4.2 In_2O_3 - Energy band gaps

The conduction band is primarily composed of In $5s$ states, with its minimum (CBM) located at the Γ point, where dispersion is notably high. In contrast, the uppermost valence bands, predominantly derived from O $2p$ states, exhibit a much flatter dispersion. As a result, the energy at Γ is only slightly lower than the valence

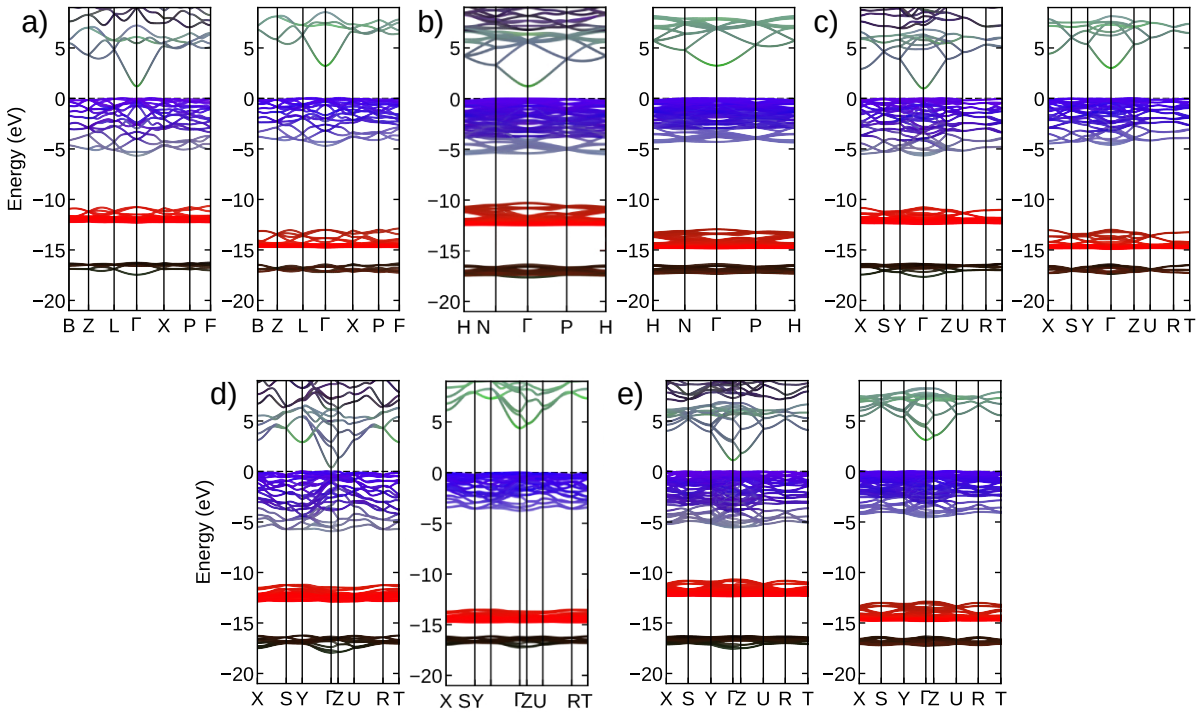

FIGURE 3.7 – Electronic band structure of In_2O_3 polymorphs. In red, In d levels; in blue, O p levels; and in green, In s levels. The five structures are shown using standard DFT (left panels) and DFT+A-1/2 (right panels) as follows: (a) α-In_2O_3, (b) δ-In_2O_3, (c) $\omega 1$-In_2O_3, (d) $\omega 2$-In_2O_3, and (e) $\omega 3$-In_2O_3. A progressive decrease in the d-level binding energy is clearly observed, ranging from approximately 12.2 eV to 14.6 eV.

band maximum along the gap direction. This small energy difference classifies all polymorphs as indirect semiconductors, with their indirect band gaps only marginally smaller than their direct or quasi-direct gaps at Γ. In the δ-phase, although discrepancies exist among published results (Tab. 3.4), all studies agree that the energy difference between the valence band at Γ and any global or local maximum outside Γ does not exceed 50 meV, a value that falls within or even below the typical accuracy range of QP calculations, thereby rendering the differences almost indistinguishable.

TABLE 3.4 – In $4d$ binding energy E_d (in eV), along with their respective deviations from the average position and energy band gaps (in eV), for all In_2O_3 polymorphs. Indirect gaps are distinguished from direct ones in parentheses. As of the conclusion of this work, no references were found for $\omega 2$- and $\omega 3$-In_2O_3.

	E_d (eV)		Band gap (eV)		Band gap (eV) - Ref.	
Polymorph	DFT	DFT+$A-1/2$	DFT	DFT+$A-1/2$	Calculated	Experimental
α-In_2O_3	12.0±0.8	14.6±0.5	1.153 (1.207)	3.162 (3.306)	3.10 [a]	(3.10) [b]
δ-In_2O_3	12.6±0.5	14.6±0.4	1.210 (1.219)	3.214 (3.371)	3.26 [a]	(3.25) [b]
$\omega 1$-In_2O_3	12.1±0.9	14.6±0.5	0.957 (0.964)	2.983 (2.295)	(2.92) [b]	(2.87)
$\omega 2$-In_2O_3	12.5±1.0	14.4±0.8	0.398 (0.361)	2.334 (2.334)	-	-
$\omega 3$-In_2O_3	12.0±0.9	14.6±0.6	1.079 (1.079)	3.088 (3.113)	-	-

[a](FUCHS; BECHSTEDT, 2008), [b](BOER *et al.*, 2016).

3.3.5 In_2O_3 - Effective masses

Determining the effective masses in In_2O_3 is particularly challenging due to the low crystal symmetry of its polymorphs. This complexity arises from several factors, including the need to analyze tensors in appropriate coordinate systems, the nonparabolicity of bands near extrema, and, in the case of hole masses, the identification of van Hove singularities in **k**-space as well as the inherent flatness of the valence bands, which lead to exceptionally large hole masses and even sign variations. Moreover, QP effects significantly influence electron masses, further complicating their determination. Given these challenges, only the electron effective masses for the CBM at the Γ point are presented in Table 3.5.

TABLE 3.5 – Electron effective masses m^* (in units of free electron mass m_0) for de In_2O_3 polymorphs provided for two directions in the BZ within DFT and DFT+$A-1/2$ framework. DFT+$A-1/2$ are provided in parentheses. For comparison, theoretical and experimental values from the literature are also listed.

	Effective masses				Effective masses - Ref.	
Polymorph	Direction	DFT (DFT+$A-1/2$)	Direction	DFT (DFT+$A-1/2$)	Calculated	Experiment
α-In_2O_3	ΓL	0.165 (0.311)	ΓX	0.170 (0.312)	0.19 [a]	0.18–0.4 [b]
δ-In_2O_3	ΓN	0.176 (0.333)	ΓP	0.178 (0.355)	0.22 [a]	0.18–0.24 [c]
ω1-In_2O_3	ΓY	0.148 (0.298)	ΓZ	0.148 (0.297)	0.17 [a]	–
ω2-In_2O_3	ΓY	0.155 (0.280)	ΓZ	0.132 (0.286)	–	–
ω3-In_2O_3	ΓY	0.157 (0.307)	ΓZ	0.151 (0.301)	–	–

[a](BOER *et al.*, 2016), [b](FENEBERG *et al.*, 2016), [c](SCHERER *et al.*, 2012).

3.3.6 In_2O_3 - Optical, dielectric, and excitonic properties

The calculations yielded various optical properties, including the real and imaginary parts of the refractive index and dielectric function, as well as the energy loss function. For clarity, and due to the extensive dataset, here are presented only the averaged dielectric constants (ε_∞), since these values were used for determining the excitonic Bohr radius r_B (in Å) and the excitonic binding energies E_B (in eV). Additional results can be found in App. D and (SILVA *et al.*, 2025).

From the comparison between the corrected dielectric function and the experimentally obtained dielectric function reported in the reference, it is noted that the corrected value is approximately 6% lower than the reference value. On the other hand, an analysis of Table 3.5, which presents the corrected values for the effective masses, reveals a compensation effect between the values of E_b and a_B. However, both the experimentally obtained m^* values and those of ε_∞ fall within the range of values

corresponding to the uncorrected and QP-corrected cases. This observation suggests that these corrected values provide a reasonable prediction for both properties.

TABLE 3.6 – Averaged electron effective masses m^* (in units of the free electron mass m_0), averaged electronic dielectric constants ε_∞, excitonic Bohr radii r_B (in Å), and exciton binding energies E_b (in eV) for the In_2O_3 polymorphs. For ε_∞, a comparison with the experimental reference value from the literature is also provided. These quantities are computed using the Wannier-Mott model without dynamical corrections to dielectric screening. Results from DFT+$A-1/2$ are presented, with standard DFT values given in parentheses.

Polymorph	$m^*(m_0)$	ε_∞	ε_∞ - Ref.	E_b (eV)	r_B
α-In_2O_3	0.312 (0.168)	4.94 (3.17)	–	0.174 (0.094)	8.38 (15.56)
δ-In_2O_3	0.333 (0.177)	4.52 (3.04)	4.8 [a]	0.222 (0.118)	7.18 (13.51)
$\omega1$-In_2O_3	0.298 (0.148)	5.22 (3.24)	–	0.146 (0.074)	9.27 (18.66)
$\omega2$-In_2O_3	0.283 (0.144)	7.07 (3.65)	–	0.077 (0.039)	13.22 (25.97)
$\omega3$-In_2O_3	0.304 (0.154)	5.09 (3.19)	–	0.160 (0.081)	8.86 (17.48)

[a](FENEBERG *et al.*, 2016)

3.3.7 In_2O_3 - Phonons and thermodynamic properties

The relationship between structural polymorphism and its lattice dynamics was explored through computational phonon studies. Phonon dispersion spectra and density of states were calculated, enabling the characterization of temperature-dependent properties including heat capacity, vibrational entropy, and contributions to free and internal energy. Dynamic stability across polymorphic phases was evaluated by analyzing the dispersion profiles of acoustic phonon modes. Imaginary frequencies were found only in the $\omega2$ polymorph, indicating the presence of soft-modes that suggest structural instability. Therefore, this phase was not considered in further analyses. The phonon spectrum along with their DOS for the dynamically stable polymorphs are shown in Fig. 3.7.

TABLE 3.7 – Parameters of the Debye law for the dinamically stable In_2O_3 polymorphs: the Debye temperature θ_D and the Debye frquency ν_D compared with experimental values found in the literature.

Polymorph	θ_D (K)	ν_D (THz)	θ_D (K) - Refe.
α-In_2O_3	658.24	13.72	–
δ-In_2O_3	685.36	14.28	420 [a], 700 [b], 650–810 [c]
$\omega1$-In_2O_3	646.44	13.47	–
$\omega3$-In_2O_3	650.24	13.55	–

[a](BACHMANN *et al.*, 1981), [b](PREISSLER *et al.*, 2013), [c](SOBOTTA *et al.*, 1990)

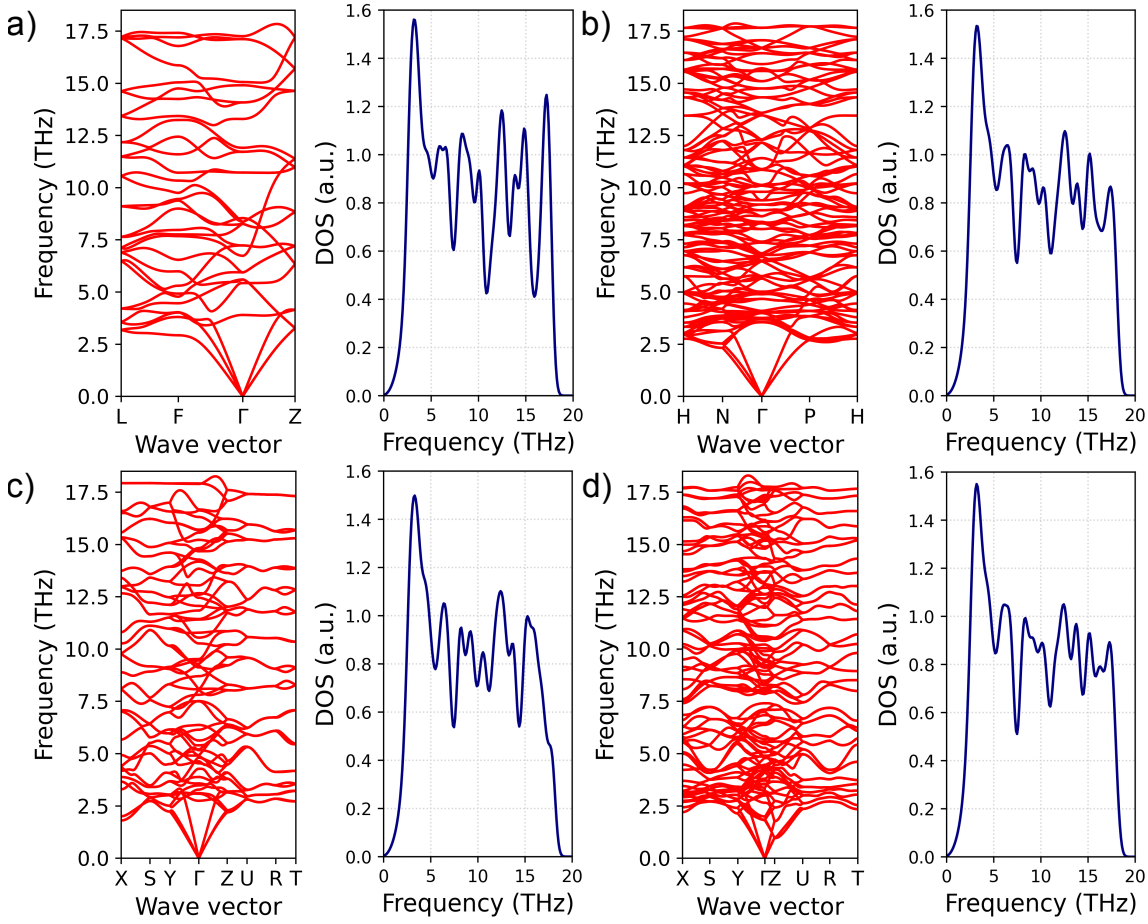

FIGURE 3.8 – Phonon dispersion relations vs. high-symmetry lines (left panels) and phonon density of states (DOS) vs. frequency for the statically and dynamically stable polymorphs. (a) α (trigonal, R$\bar{3}$c, 10 atoms), (b) δ (cubic bixbyite, Ia$\bar{3}$, 40 atoms), (c) $\omega 1$ (orthorhombic, Pbcn, 20 atoms), and (d) $\omega 3$ (orthorhombic, Pbca, 40 atoms). Smoothed curves were obtained artificialy applying Gaussian broadening.

The Debye T^3 formalism provided the theoretical framework for interpreting low-temperature heat capacity trends. This approach models atomic vibrations as quantized phonon modes with a well-defined frequency spectrum, effectively capturing the cubic temperature dependence of the molar heat capacity at constant volume ($C_V \propto T^3$) observed in solids at cryogenic temperatures. By applying Debye's theory, the Debye temperatures and Debye frequencies were extracted. The obtained values are presented in Table 3.7.

3.3.7.1 In_2O_3 - Temperature-induced phase transitions

Using the quasi-harmonic approximation, the temperature DOS $D(\omega)$ dependent is investigated. Specifically, the the total free energy $F(T)^{\text{tot}} = F(T)^{\text{el}} + F(T)^{\text{vib}}$ and its variation, $\Delta F(T)^{\text{tot}} = F(T)^{\text{tot}}_p - F(T)^{\text{tot}}_\delta$, which represents the difference between the free energy of a given polymorph p and that of the most stable phase δ. Using this

approach, we identified three significant temperature-induced phase transitions between the stable δ phase and the metastable phases at room temperature. These transitions are illustrated in Fig. 3.8. A phase transition from the δ to the α phase was identified at 515 K,

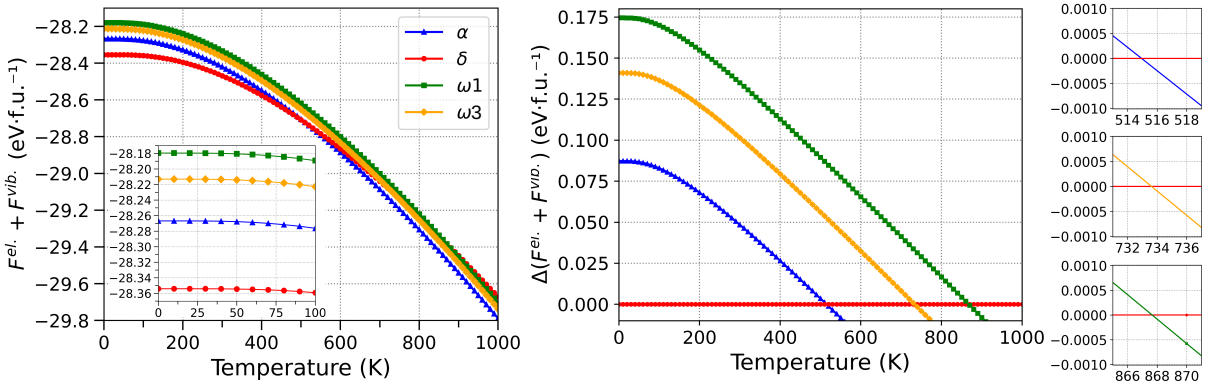

FIGURE 3.9 – Total free energy as a function of temperature for the four dynamically stable phases. The left panel shows $F(T)^{\text{tot}} = F(T)^{\text{el}} + F(T)^{\text{vib}}$ in eV·f.u.$^{-1}$. The middle panel displays the variation $\Delta F(T)^{\text{tot}} = F(T)^{\text{tot}}_{p} - F(T)^{\text{tot}}_{\delta}$ (eV·f.u.$^{-1}$). The three panels on the right provide zoomed-in views of the temperature region where the phase transitions occur.

indicating that the α phase becomes thermodynamically more stable in this temperature range. Additional transitions were found from δ to $\omega 3$ at 733.5 K and from δ to $\omega 1$ at 867.6 K, suggesting that these phases have lower free energy at higher temperatures. This stabilization is likely influenced by entropic contributions, such as enhanced thermal vibrations and disorder, favoring these structures.

3.4 Gallium oxide porlymorphs

Following the approach used for In_2O_3, this part of the study examines the electronic, optical, excitonic, and thermodynamic properties of five Ga_2O_3 polymorphs. The phases analyzed include the monoclinic β-phase (space group C2/m), the most thermodynamically and structurally stable; the metastable rhombohedral α-phase with a corundum-like structure (space group R$\bar{3}$c); the defective spinel cubic γ-phase (space group Fd$\bar{3}$m); the cubic δ-phase, which adopts a bixbyite structure (space group Ia$\bar{3}$); and the orthorhombic κ-phase (space group Pna2$_1$). As with the In_2O_3 polymorphs, both primitive and non-primitive unit cells were considered for the α and δ phases. Similarly, the atomic arrangement of the β-phase is described using either a primitive cell–comprising 10 atoms and representing the smallest repeating unit that fully captures the crystal's symmetry and lattice parameters–or and a conventional cell, commonly used in theoretical studies, which contains 20 atoms to emphasize the lattice centering and complete symmetry.

The crystalline structure of Ga_2O_3 polymorphs is notably complex due to the interplay of several interrelated factors. First, gallium atoms can adopt different coordination numbers–generally ranging between four and six–resulting in distinct bonding environments that influence the formation of varied structures. Moreover, the arrangement of oxygen atoms within the crystal lattice is not unique; these arrangements can vary, thereby altering both the symmetry and the overall structural connectivity of the material.

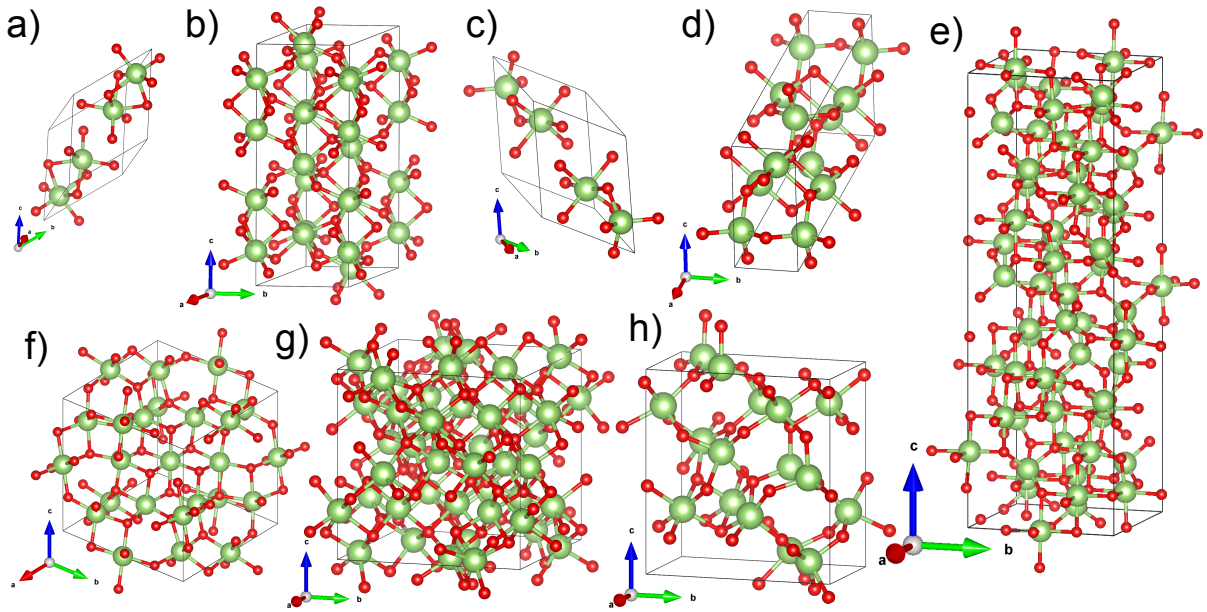

FIGURE 3.10 – Structural representations of Ga_2O_3 polymorphs: (a) α-Ga_2O_3, trigonal (rhombohedral) primitive 10-atom unit cell ($R\bar{3}c$); (b) its hexagonal counterpart with 30 atoms ($R\bar{3}c$); (c) the primitive β-Ga_2O_3 monoclinic unit cell (C2/m); (d) its conventional cell; (e) the defective cubic spinel structure of the γ-phase ($Fd\bar{3}m$); (f) the cubic bixbyite δ-phase in its primitive unit cell and (g) its conventional cell; and (h) the orthorhombic κ-phase ($Pna2_1$). Gallium atoms are shown in purple, and oxygen atoms in red.

TABLE 3.8 – General information of Ga_2O_3 polymorphs. In the α, β, and δ cases, primitive (10, 10, and 40) and non-primitive (30, 20, and 80) atoms per unit cells were calculated, respectively.

Polymorph	Crystal system	Structure / name or model	Space group	Atoms per unit cell
α-Ga_2O_3	Rhombohedral	Corundum	$R\bar{3}c$	10/30
β-Ga_2O_3	Monoclinic	Muscovite	C2/m	20
γ-Ga_2O_3	Cubic	Defective spinel	$Fd\bar{3}m$	160
δ-Ga_2O_3	Cubic	Bixbyite	$Ia\bar{3}$	40/80
κ-Ga_2O_3	Orthorhombic	Enstatite	$Pna2_1$	40

This diversity in atomic configurations contributes significantly to the existence of different polymorphs and not only explains the observed structural diversity but also

suggests that precise control of synthesis parameters may be an effective strategy for obtaining phases with properties optimized for electronic and optoelectronic applications. A comparative overview of the structural models, space groups, and atomic compositions is provided in Table 3.8, and the complex geometries of these structures are illustrated in Figure 3.10.

Keeping in mind that the band alignment and material properties associated with the crystal space group differ slightly among the polymorphs, and that the coordination number of Ga^{3+} ions also varies among these phases, this part of the study investigates the structural, electronic, optical, excitonic, and thermodynamic characteristics of the five aforementioned polymorphs.

3.4.1 Ga_2O_3 - Structural properties

The atomic coordinates and lattice constants of the polymorphs were determined by minimizing the total energy and forces. The difference in minimal energies between calculations with and without SOC is negligible. Given that the combined effect of SOC and the AM05 functional remains within the expected DFT accuracy–and considering the additional computational cost–the results presented here are based on calculations without SOC, as the computational expense does not yield significantly different outcomes.

TABLE 3.9 – Lattice constants (a, b, and c) in Å, mutual angles (α, β, and γ) in degrees (°) and atoms per cell of Ga_2O_3 polymorphs. In the case of α and δ phases primitive and non-primitive unit cells are presented containing 10 and 30 atoms in the (triclinic and hexagonal) cell. Experimental results (SPENCER *et al.*, 2022) are provided for reference.

	Lattice constants (Å)						Angles (°)		
	This work			Reference			This work		
Polymorph	a	b	c	a	b	c	α	β	γ
α-Ga_2O_3	5.333	5.333	5.333				55.88	55.88	55.88
α-Ga_2O_3 (np)	5.002	5.002	13.467	4.98	4.98	13.43	90.00	90.00	120.00
β-Ga_2O_3	6.342	6.342	6.342				103.31	103.31	27.83
β-Ga_2O_3 (np)	12.621	3.155	5.814	12.23	3.03	5.80	90.00	103.74	90.00
γ-Ga_2O_3	8.238	8.238	24.713	8.237	8.237	8.237	90.00	90.00	90.00
δ-Ga_2O_3	8.048	8.048	8.048				109.47	109.47	109.47
δ-Ga_2O_3 (np)	9.301	9.301	9.301	9.52	9.52	9.52	90.00	90.00	90.00
κ-Ga_2O_3	5.061	8.687	9.291	5.066	8.70	9.261	90.00	90.00	90.00

Lattice parameters obtained using the AM05 functional differ only slightly from available experimental data, likely due to gradient corrections in the XC functional,

similar to what is observed in In_2O_3. The largest average deviation, approximately 0.2 Å, is observed in the β phase, while the smallest deviation, around 0.001 Å, occurs in the γ phase. Table 3.9 summarizes the structural parameters of the five polymorphs under study.

It is worth mentioning that, due to the complex cubic defective-spinel structure of the γ phase, a perfectly cubic cell fails to preserve the system's stoichiometry because in an ideal spinel structure, cations and anions are arranged in a highly ordered manner that maintains the correct stoichiometric ratios. However, intrinsic defects–such as cation vacancies and local distortions–disrupt this order. To address this issue, a $1\times1\times3$ supercell was employed in the calculations, following the model proposed by Ratcliff *et al* (RATCLIFF *et al.*, 2022).

3.4.2 Ga_2O_3 - Stability and equilibrium parameters

A fit procedure using four EOS (Birch, Murnaghan, Birch-Murnaghan and Vinet), was used in order to investigate the behavior of the total energy $E = E(V)$ as a function of volume V. From the same calculations the equilibrium volume V_0, energy $E_0 = E(V_0)$, isothermal bulk modulus B_0, and its pressure derivative B_0' were obtained. Tab. 3.10 presents these results for the five polymorphs.

TABLE 3.10 – Equilibrium parameters of Ga_2O_3 polymorphs calculated using Vinet EOS. All results presented are related to the largest non-primitive unit cells.

Polymorph	$-E_0$ (eV/f.u.)	V_0 (Å^3/f.u.)	B_0 (GPa)	B_0'
α-Ga_2O_3	30.83	48.74	215.72	4.55
β-Ga_2O_3	30.91	53.05	193.66	4.51
γ-Ga_2O_3	30.75	53.41	190.87	4.53
δ-Ga_2O_3	30.78	50.31	205.54	4.75
κ-Ga_2O_3	30.83	51.30	201.86	4.66

Despite the results obtained from the four EOS exhibiting values in good agreement, with only negligible differences–as observed in In_2O_3 polymorphs–only those derived from the Vinet EOS, which yielded the lowest $E_0 = E(V_0)$, were considered. The $E(V)$ curves shown in Fig. 3.9 confirm that Ga_2O_3 crystallizes in a monoclinic structure under ambient conditions, as well established in the literature. The energetic ordering of the β, κ–α, δ, and γ phases at their lowest energies $E_0 = E(V_0)$ correlates with their equilibrium volumes V_0, as presented in Table 3.10 and illustrated in Fig.3.11.

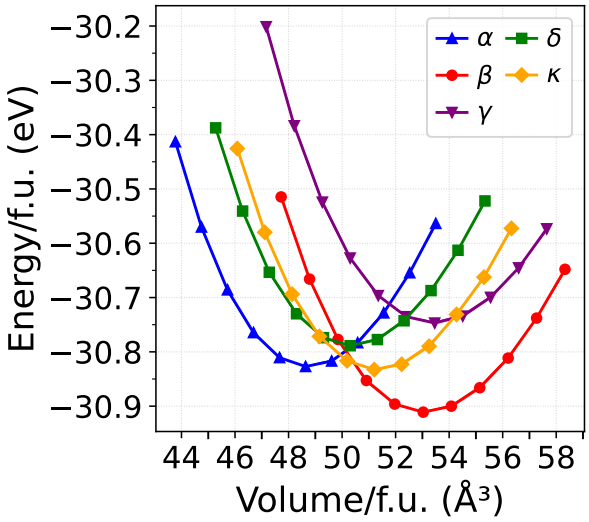

FIGURE 3.11 – Normalized total energy versus volume per formula unit of Ga_2O_3 for the five polymorphs under consideration.

3.4.3 Ga_2O_3 - Pressure-induced phase transitions

Using the data acquired from EOS and following the same procedure as the employed in In_2O_3 polymorphs, the enthalpies H were analyzed. The derivation of the expression used for obtaining the enthalpies as function of pressure $H = H(p)$ is presented in Appendix B Sec. B.3. The differences $\Delta H(p) = H(p) - H_\beta(p)$ are considered, where $H_\beta(p)$ represents the enthalpy of the stable phase at room temperature. With this procedure it was possible to considerably reduce the error bars, allowing a better graphical representation of the phase transitions. The $H(p)$ versus pressure p, is displayed in Figure 3.12 and the most important pressure induced phase transitions observed between polymorphs are listed as: (i) between β and α phases around p_t=3.8 GPa, labeled as "a"; (ii) between β to κ and/or δ around p_t=8.7 GPa; and (iii) between α and κ.

The sequence of phase transitions demonstrates that the relative stability of the polymorphs is governed by a delicate balance between statical internal equilibrium energy (E_0) and equilibrium statical equilibrium volume (V_0). Initially, the β phase exhibits the highest energetic stability under ambient conditions; however, its larger volume results in an increasing penalty from the pV term as pressure rises. Consequently, above 3.8 GPa, the β phase loses its stability in favor of the α phase, which has a smaller volume, and at even higher pressures (8.7 GPa), the lower-volume phases (δ or κ) become preferentially stable. Moreover, the transition between the α and κ phases, observed at 0.63 GPa, underscores how minor volumetric differences can dictate relative stability when the E_0 values are nearly identical.

Although the intrinsic energies of the phases are very close, the kinetic barriers associated with structural reorganization can either facilitate or hinder specific

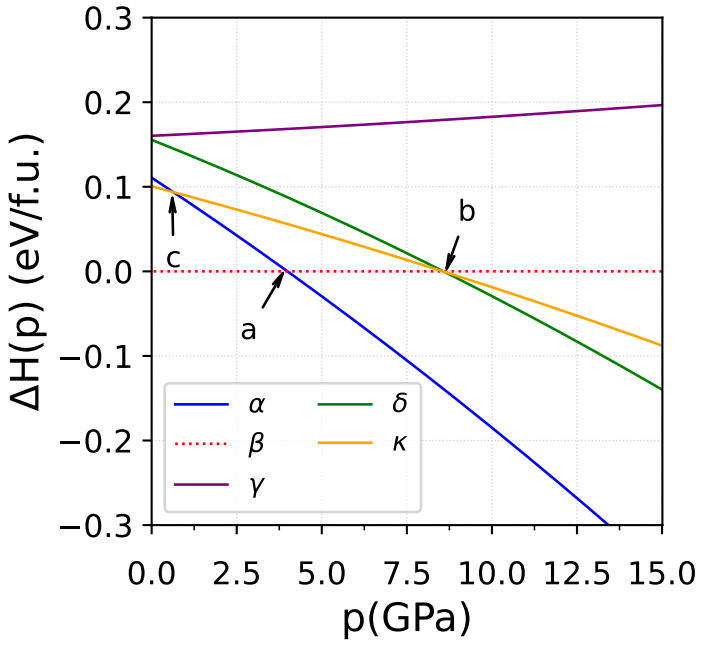

FIGURE 3.12 – Enthalpy per formula unit of Ga_2O_3 as a function of hydrostatic pressure for the five polymorphs under consideration. The arrows labeled by "a" to "f" indicate the phase transition between two polymorphs.

transitions. This factor helps explain why the β-to-α transition occurs at a considerably lower pressure than the transitions to the δ or κ phases. Additionally, dynamic contributions–such as vibrational effects and (zero point energy) ZPE–can modify the relative stability of the polymorphs at nonzero temperatures, thereby affecting the transition pressures. In summary, the stability and phase transitions are determined not solely by the balance between E_0 and pV_0, but by a combination of thermodynamic and kinetic factors. Among these, compressibility plays a crucial role, as a less compressible phase will maintain a more pronounced volumetric difference under pressure, potentially altering the stability order predicted from the initial V_0 values.

3.4.4 Ga_2O_3 - Electronic structure

As in the case of In_2O_3, even with the AM05 XC functional, both the energy band gaps E_g and d-electron binding energies E_B^d with respect to the VBM are underestimated within standard DFT approach. In order to deal with the both issues, in a first step, as usual, the determination of the amplitude A was carried out by comparing the average position of the Ga $3d$ level considering experimental data available, in general, only for the stable phase. The second step was evaluate the fundamental energy band gap (indirect) E_g^{ind} and perform the quasi-particle self-energy correction calculations.

3.4.4.1 Ga_2O_3 - *d*-level position

Using the procedure, described in Chap. 2, section 2.3.1, the average position of the d-level was determined and compared to the experimental results available. The d-derived occupied bands exhibit band widths less than 1 eV, similarly as in the case of In_2O_3 and also, as expected, the Ga $3d$ levels are delocalized. In this case, much more delocalized than In $4d$ levels in In_2O_3 and of about 7.3 eV in terms of binding energy. The A level amplitude was adjusted to the average position of the d bands based on experimental data (NAVARRO-QUEZADA *et al.*, 2015; SWALLOW *et al.*, 2020). Since there is the possibility of transferability of pseudopotentials (GOEDECKER; MASCHKE, 1992), the pseudopotential A-modulated could be applied to polymorphs without experimental data available in the literature. Such procedure also cause a small variation in the VBM O $2p$ levels that directly influence the final band gap improving it. The results obtained are presented in Table 3.11.

3.4.4.2 Ga_2O_3 - Energy band gaps

For all polymorphs one observes strong dispersion around Γ, and, on the other hand, O$2p$-derived uppermost valence bands exhibit a much weaker dispersion. Except for κ-Ga_2O_3 all other four polymorphs exhibit indirect fundamental band gaps with a VBM out of Γ, more especifically between ΓX (α-Ga_2O_3), ML (β-Ga_2O_3), VR (γ-Ga_2O_3), and ΓN (δ-Ga_2O_3). The inclusion of the excitation aspect, the quasiparticle effects, is most important for the final energy gap and the quasiparticle gap opening amounts to nearly 2.1-2.3 eV.

TABLE 3.11 – Ga $3d$ binding energy E_d in eV with their respective deviation from the average position, and energy band gaps in eV for all Ga_2O_3 polymorphs. Indirect gaps are distinguished from direct ones in parenthesis. Refs: a) (FURTHMÜLLER; BECHSTEDT, 2016) calculations using HSE03/06+GW, b) (HILFIKER *et al.*, 2022), c) (YOSHIOKA *et al.*, 2007), d) (MENGLE *et al.*, 2016), e) (RATCLIFF *et al.*, 2022), f) (NADA, a), g) (PAVESI *et al.*, 2018), and (KATO *et al.*, 2023).

	E_d (eV)		Band gap (eV)		Band gap (eV) - Ref.	
Polymorph	DFT	DFT+$A-1/2$	DFT	DFT+$A-1/2$	Calculated	Experimental
α-Ga_2O_3	12.3±0.5	19.8±0.3	2.800 (3.014)	5.087 (5.228)	5.387 (5.625) [a]	5.44-6.04 [b]
β-Ga_2O_3	12.6±2.2	19.9±0.3	2.297 (2.320)	4.644 (4.786)	5.038 (5.046) [a]	4.4 [c] (4.4-5.0) [d]
γ-Ga_2O_3	12.9±1.6	20.1±1.5	2.382 (2.385)	4.606 (4.623)	4.65 [e]	5.17 [e]
δ-Ga_2O_3	12.8±0.5	19.8±0.5	2.549 (2.648)	4.709 (4.762)	-	4.3–4.9 [h]
κ-Ga_2O_3	12.5±0.8	20.0±0.6	2.418 (2.418)	4.676 (4.676)	4.48 [f]	4.6–4.7 [g]

The comparison of fundamental band gap with references for the five polymorphs are presented in Table 3.11 and the electronic band structures are depicted in Figure 3.13. In Figure 3.13 one can clearly observe the shallow d-level (in red) of about 12.5 eV decreasing

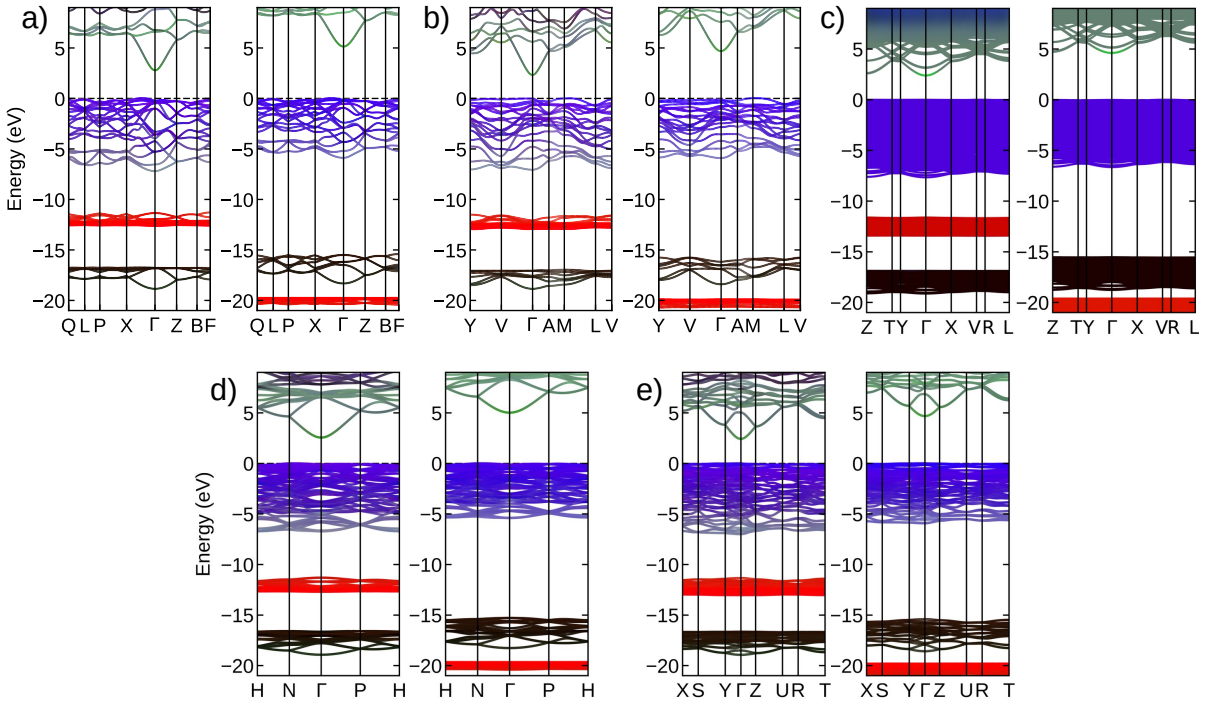

FIGURE 3.13 – Electronic band structure of Ga_2O_3 polymorphs. In red, Ga $3d$ levels, in blue, O p levels, and In s levels in green. The five polymorphs are represented in standard DFT (left panels) and DFT+$A-1/2$ (right panels) as (a) α-Ga_2O_3, (b) β-Ga_2O_3, (c) γ-Ga_2O_3, (d) δ-Ga_2O_3, and (e) κ-Ga_2O_3. Explicitly is demonstrated the decreasing of the d-level binding energy from about 12.5 eV to about 20.0 eV.

to about 20.0 eV after the corrections. Also, in the case of γ-Ga_2O_3 is evident the high density of grouped bands due the number of atoms in the unit cell (160 atoms) used in the calculations.

3.4.5 Ga_2O_3 - Effective masses

A common characteristic among all Ga_2O_3 polymorphs is the high dispersion of the valence band maximum (VBM). In some cases, this results in nearly flat bands, leading to unrealistically large hole effective masses. Additionally, the low crystalline symmetry of these polymorphs further complicates the determination of effective masses. Another relevant factor is the quasiparticle (QP) correction, which slightly reduces the parabolicity at the extrema of both the VBM and the conduction band minimum (CBM). Due to these challenges, only the electron effective masses were computed, with the corresponding values presented in Table 3.12.

For the α-, β-, and κ-polymorphs, the effective masses obtained within standard DFT show good agreement with previous theoretical predictions from the literature. The DFT+$A-1/2$ corrected values (in parentheses) are systematically higher than the

standard DFT values, improving agreement with experimental results, particularly for the β phase.

TABLE 3.12 – Electron effective masses m^* (in units of free electron mass m_0) for de Ga_2O_3 polymorphs provided for two directions in the BZ within DFT and DFT+$A-1/2$ framework. For comparison, theoretical and experimental values from the literature are also listed.

	Effective masses				Effective masses - Ref.	
Polymorph	Direction	DFT (DFT+$A-1/2$)	Direction	DFT (DFT+$A-1/2$)	Calculated	Experiment
α-Ga_2O_3	ΓX	0.238 (0.374)	ΓZ	0.234 (0.396)	0.21 [a], 0.256 [b]	0.276–0.297 [c]
β-Ga_2O_3	ΓY	0.231 (0.405)	ΓV	0.237 (0.400)	0.21 [a], 0.268 [b]	0.311 [c], 0.44 [d]
γ-Ga_2O_3	ΓY	0.264 (0.422)	ΓZ	0.263 (0.426)	–	–
δ-Ga_2O_3	ΓN	0.240 (0.396)	ΓP	0.241 (0.396)	–	–
κ-Ga_2O_3	ΓY	0.235 (0.394)	ΓZ	0.235 (0.405)	0.23 [e]	–

[a](FAN *et al.*, 2022), [b](FURTHMÜLLER; BECHSTEDT, 2016), [c](KNIGHT *et al.*, 2018), [d](PEARTON *et al.*, 2018), [e](WANG *et al.*, 2020)

3.4.6 Ga_2O_3 - Optical, dielectric, and excitonic properties

Extensive computational investigations on Ga_2O_3 were conducted to understand its optical characteristics across various polymorphs. These analyses provided detailed information on the refractive index, dielectric function, and energy loss function, offering insights into the material's response to electromagnetic fields, electronic structure, and behavior under high-energy excitation, which is crucial for optoelectronic and plasmonic applications.

Given the large volume of data generated in these calculations, a decision was made to focus on the averaged dielectric constants, ε_∞. These values are pivotal in assessing the optical properties of Ga_2O_3 and were instrumental in calculating the excitonic properties of the material. Specifically, the excitonic Bohr radius (r_B in Å) and the excitonic binding energies (E_b in eV) were determined. The exciton properties provide valuable insights into the material's optical response, particularly with regard to its absorption and emission spectra. By focusing on these averaged dielectric constants, the report streamlines the presentation, highlighting the most critical parameters that govern the material's optical behavior, while minimizing the complexity of the data.

The complete spectral analysis, along with additional results and a more in-depth discussion of the computational methods, can be found in Appendix E and in the study by (SILVA *et al.*, 2025). Table 3.13 provides the specific values used in the computation of the excitonic properties for the various Ga_2O_3 polymorphs, offering a clear view of the input parameters and their influence on the calculated excitonic characteristics.

TABLE 3.13 – Averaged electron effective masses m^* (in units of the free electron mass m_0), averaged electronic dielectric constants ε_∞ (derived exclusively from DFT+$A-1/2$), excitonic Bohr radii r_B (in Å), and exciton binding energies E_b (in eV) for the Ga_2O_3 polymorphs. For ε_∞, a comparison with the experimental reference value from the literature is also provided. These quantities are computed using the Wannier-Mott model without dynamical corrections to dielectric screening. Results from DFT+$A-1/2$ are presented, with standard DFT values given in parentheses.

Polymorph	$m^*(m_0)$	ε_∞	ε_∞ - Ref.	E_b (eV)	r_B
α-Ga_2O_3	0.385 (0.236)	4.02	3.75 [b]	0.324 (0.199)	5.52 (9.01)
β-Ga_2O_3	0.402 (0.234)	4.09	3.95 [a]	0.327 (0.190)	5.38 (9.25)
γ-Ga_2O_3	0.424 (0.264)	4.01	–	0.359 (0.223)	5.00 (8.04)
δ-Ga_2O_3	0.396 (0.241)	4.23	–	0.301 (0.183)	5.65 (9.28)
κ-Ga_2O_3	0.400 (0.235)	4.21	–	0.307 (0.180)	5.57 (9.48)

[a](SCHUBERT *et al.*, 2016), [b](FENEBERG *et al.*, 2018)

3.4.7 Ga_2O_3 - Phonons and thermodynamic properties

The investigation of structural polymorphism and its impact on lattice dynamics was conducted through computational phonon calculations. Phonon dispersion spectra and DOS were obtained, enabling a detailed evaluation of temperature-dependent thermodynamic properties such as heat capacity, vibrational entropy, and contributions to free and internal energy. The absence of imaginary frequencies in all analyzed phases confirmed their dynamical stability, indicating no soft modes that could lead to structural instabilities. However, the γ phase was excluded from the calculations due to the computational challenges posed by its large unit cell, which contains 160 atoms. Constructing the dynamical matrix for this phase would require over 900 individual displacements, making phonon calculations prohibitively expensive.

To further investigate the low-temperature heat capacity behavior of Ga_2O_3, the Debye T^3 formalism was employed. This approach is particularly effective in capturing the cubic temperature dependence of the molar heat capacity at constant volume ($C_V \propto T^3$), which is commonly observed in solids at cryogenic temperatures. The model assumes that atomic vibrations can be described as quantized phonon modes, each with a well-defined frequency spectrum. By applying Debye's theory, it was possible to extract the Debye temperatures and frequencies for the various polymorphs of Ga_2O_3. These quantities provide valuable insights into the vibrational properties of the material at low temperatures. The extracted Debye temperatures and frequencies for the polymorphs under consideration are summarized in Table 3.14. Additionally, the phonon spectra and their corresponding density of states (DOS) for the different phases are presented in Figure 3.14.

TABLE 3.14 – Parameters of the Debye law for the dinamically stable In_2O_3 polymorphs: the Debye temperature θ_D and the Debye frquency ν_D compared with experimental values found in the literature.

Polymorph	θ_D (K)	ν_D (THz)	θ_D (K) - Refe.
α-Ga_2O_3	787.5	16.41	–
β-Ga_2O_3	770.9	16.06	738 [a]
δ-Ga_2O_3	779.8	16.25	–
κ-Ga_2O_3	738.7	15.39	–

[a](GUO *et al.*, 2015)

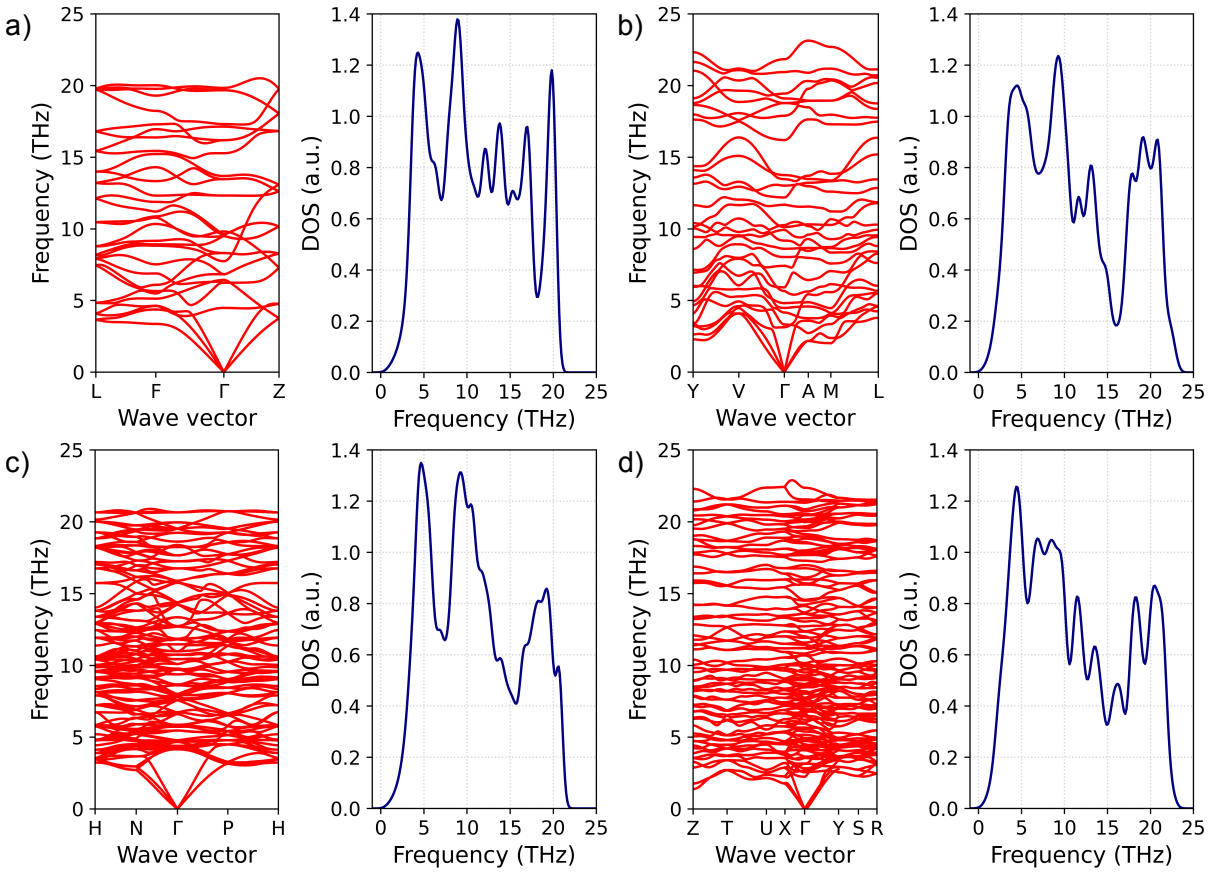

FIGURE 3.14 – Phonon dispersion relations vs. high-symmetry lines (left panels) and phonon density of states (DOS) vs. frequency for the statically and dynamically stable polymorphs. (a) α (trigonal, R$\bar{3}$c, 10 atoms), (b) β (monoclinic, C2/m, 20 atoms), (c) δ (cubic bixbyite, Ia$\bar{3}$, 40 atoms), and (d) κ (orthorhombic, Pna2_1, 40 atoms). Smoothed curves of DOS were obtained artificialy applying Gaussian broadening.

3.4.8 Ga_2O_3 - Temperature-induced phase transitions

From the DOS $D(\omega)$ of phonons the total free energy $F(T)^{\text{tot}}$ of the five polymorphs calculated and its variations $\Delta F(T)^{\text{tot}}$ were obtained to analyse temperature-induced phase transitions. These values across different polymorphs as a function of the

temperature (in K) are exhibited in Figure 3.13. From these relations a phase transition between the β to κ phase is found about 3048 K.

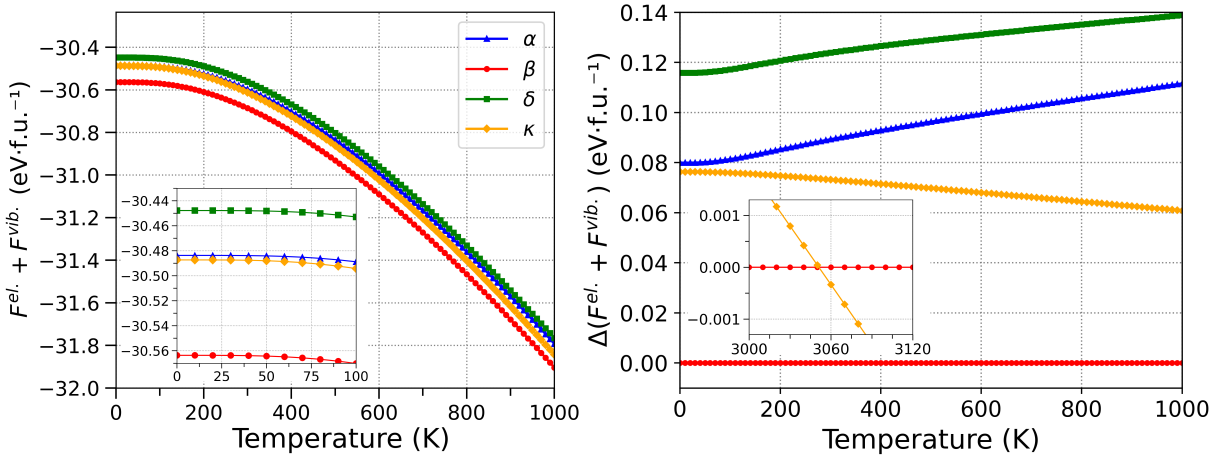

FIGURE 3.15 – Total free energy as a function of temperature for the four dynamically stable phases analysed. The left panel shows $F(T)^{\text{tot}} = F(T)^{\text{el}} + F(T)^{\text{vib}}$ in eV·f.u.$^{-1}$. The total free energy at 0 K is displayed as a zoomed-in view. The right panel displays the variation $\Delta F(T)^{\text{tot}} = F(T)^{\text{tot}}_{p} - F(T)^{\text{tot}}_{\delta}$ (eV·f.u.$^{-1}$). The $\beta \rightarrow \kappa$ phase transition is shown as an inset.

3.5 Aluminum oxide porlymorphs

Aluminium oxide (Al_2O_3), is another group III sesquioxide with diverse applications, and manifests in two principal forms: α-alumina (stable), commonly known as corundum, and γ-Al_2O_3 (metastable), referred to as activated alumina (ROUQUEROL *et al.*, 1999). In its various forms, holds a position of remarkable significance across a spectrum of scientific disciplines, from terrestrial geology to the vast expanse of planetary science (LIESHOUT *et al.*, 2016). Its crystalline manifestation as corundum gives rise to gemstones of exceptional beauty and utility, most notably sapphire and ruby (CHAIWONG *et al.*, 2005). Sapphire, prized for its hardness and optical properties, finds applications in high-durability windows, electronic substrates, and even as a component in laser technology (YANG *et al.*, 2024). In the other hand, ruby has historically been valued for its gemological appeal but has also found critical use in the development of the first lasers (MAIMAN, 1960). Beyond these well-known gemstones, Al_2O_3 is a fundamental constituent of numerous minerals, contributing to the composition of Earth's crust and mantle. Its presence in various geological formations provides invaluable insights into the planet's history and the processes that have shaped it over eons (MIYAZAKI; KORENAGA, 2022).

Al_2O_3 also demonstrates extensive polymorphism (LEVIN; BRANDON, 1998) and various crystal growth techniques have been applied to Al_2O_3, including techniques at

room temperature (CORTES-VEGA *et al.*, 2018). In this section of the study, the structural, electronic and optical properties of twenty-four polymorphs of Al_2O_3 were investigated. The polymorphs under study are listed in Tab. 3.15 and the phases found to be dynamically stable are illustrated in Figure 3.16.

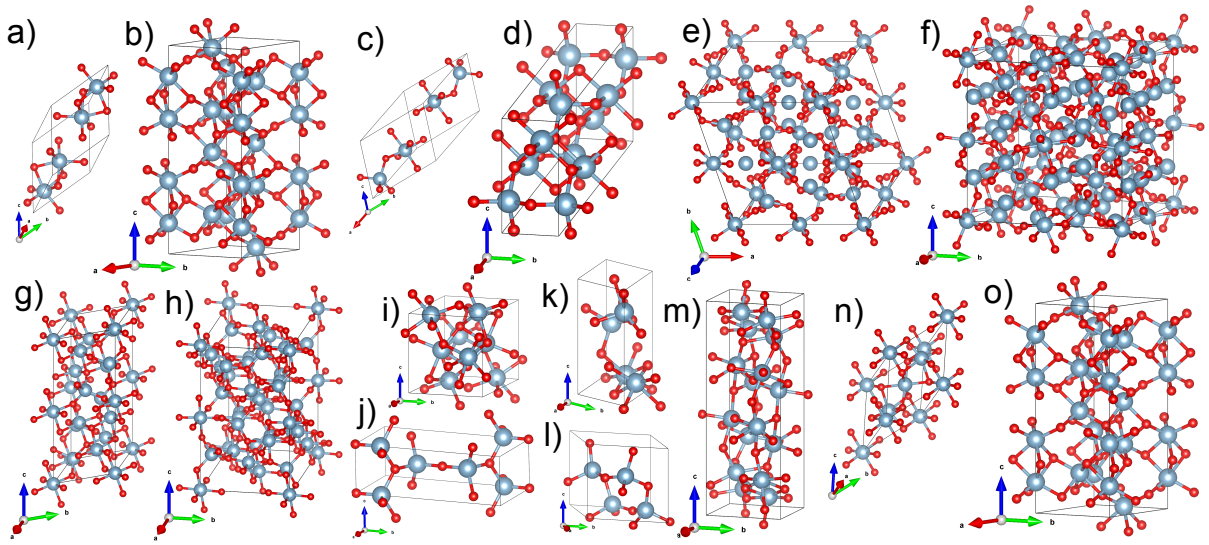

FIGURE 3.16 – Structural representations of the ten dynamically stable polymorphs of Al_2O_3: (a, b) α-phase (R$\bar{3}$c, trigonal rhombohedral) with 10 and 30 atoms, respectively; (c, d) θ-phase (C2/m, monoclinic) with 10 and 20 atoms; (e, f) δ-phase (Ia$\bar{3}$, cubic bixbyite) with 40 and 80 atoms; (g, h) θ2-phase (C2/c, monoclinic) with 40 and 80 atoms; (i) ω3-phase (Pbcn, orthorhombic, 20 atoms); (j) ω2-phase (Pnnm, orthorhombic, 10 atoms); (k) γ'-phase (P1, triclinic, 10 atoms); (l) ω1-phase ($Cmc2_1$, orthorhombic, 10 atoms); (m) ω4-phase (Pbca, orthorhombic, 40 atoms); and (n, o) α'-phase (R$\bar{3}$, trigonal rhombohedral) with 10 and 40 atoms. Aluminum (Al) and oxygen (O) atoms are represented as blue and red spheres, respectively.

3.5.1 Al_2O_3 - Structural properties

The procedure of minimizing energies and forces, previously established for determining structural parameters in other oxides, was applied to the Al_2O_3 polymorphs. The variations in lattice parameters between calculations with and without the inclusion of SOC were on the order of 10^{-3} Å. Consequently, the results obtained without SOC were selected for presentation, justified by the better agreement with available experimental data, the compatibility with the intrinsic precision of DFT calculations, and low computational effort. These results are listed in Table 3.16. Additionally, the predictive capability of the PBE and AM05 functionals was compared and to keep the consistency with the results of the other oxides, only the results obtained using the AM05 was considered, confirming the better performance in all the cases.

TABLE 3.15 – General information on Al_2O_3 polymorphs. Given the multiplicity of polymorphs, their structural description is based on space group symmetry. When applicable, representative mineral names are used to simplify notation. For polymorphs where the number of atoms per unit cell is given with a separating slash, this indicates that both primitive and non-primitive cells were considered in the calculations. Additionally, to facilitate the identification of structures, some notations not found in the literature have been introduced based on structural similarity or closely related names.

Polymorph	Crystal system	Structure / name or model	Space group	Atoms per unit cell
γ'-Al_2O_3	Triclinic	Nordstrandite $Al(OH)_3$	P1	10
θ-Al_2O_3	Monoclinic (base-centered)	β-Ga_2O_3	C2/m	10/20
$\theta 2$-Al_2O_3	Monoclinic (base-centered)	Tenorite (CuO)	C2/c	10/20
λ-Al_2O_3	Monoclinic (simple)	Bismite (α-Bi_2O_3)	$P2_1/c$	20
κ-Al_2O_3	Orthorhombic (simple)	LGO ($LiGaO_2$)	$Pna2_1$	40
$\omega 1$-Al_2O_3	Orthorhombic (base centered)	Saltpeter (KNO_3)	$Cmc2_1$	10
$\omega 2$-Al_2O_3	Orthorhombic (simple)	Ferroselite ($FeSe_2$)	Pnnm	10
$\omega 3$-Al_2O_3	Orthorhombic (simple)	Rh_2O_3 (II)	Pbcn	20
$\omega 4$-Al_2O_3	Orthorhombic (simple)	Enstatite ($MgSiO_3$)	Pbca	40
$\omega 5$-Al_2O_3	Orthorhombic (base centered)	U_2S_3	Pnma	20
$\omega 6$-Al_2O_3	Orthorhombic	$CaIrO_3$	Cmcm	10
τ-Al_2O_3	Tetragonal	α-cristobalite (SiO_2)	$P4_12_12$	160
τ'-Al_2O_3	Tetragonal (simple)	Mawsonite ($Cu_6Fe_2SnS_8$)	$P\bar{4}m2$	5
α'-Al_2O_3	Trigonal (rhombohedral)	Ilmenite ($FeTiO_3$)	$R\bar{3}$	10/30
α-Al_2O_3	Trigonal (rhombohedral)	Corundum	$R\bar{3}c$	10/30
χ''-Al_2O_3	Hexagonal	α-quartz (SiO_2)	$P3_121$	15
χ'-Al_2O_3	Hexagonal	ZrS_2	$P\bar{3}m1$	5
κ'-Al_2O_3	Hexagonal	Wurtzite (Zn, Fe)S_2	$P6_3mc$	5
χ-Al_2O_3	Hexagonal	WC-type (WC)	$P\bar{6}m2$	5
δ-Al_2O_3	Cubic (body centered)	Bixbyite (δ-In_2O_3)	$Ia\bar{3}$	40/80
γ''-Al_2O_3	Cubic (simples)	Perovskite ($SrFeO_3$)	$Pm\bar{3}m$	5
$\delta\delta$-Al_2O_3	Cubic (simples)	Double diamond cuprite (Cu_2O)	$Pn\bar{3}m$	10
γ-Al_2O_3	Cubic ($1\times1\times3$) [a]	Defective spinel (γ-Ga_2O_3)	$Fd\bar{3}m$	160
δ'-Al_2O_3	Cubic (body centered)	Garnet [$X_3Y_2(SiO_4)_3$]	$Ia\bar{3}d$	80/160

[a] A similar scheme used in γ-Ga_2O_3 was used to reproduce the cubic defective-spinel $1\times1\times3$ supercell in accordance with the model demonstrated by Ratcliff *et al* (RATCLIFF *et al.*, 2022).

The computational simplicity of the calculations for Al_2O_3, compared to In_2O_3 and Ga_2O_3, is due to the absence of d-levels in aluminum, whose electronic configuration is [Ne] $3s^2$ $3p^1$. Thus, for Al_2O_3, only the QP (quasiparticle) correction to the oxygen s-level in the VBM (valence band maximum) was considered.

TABLE 3.16 – Lattice parameters of 24 Al_2O_3 polymorphs from all seven crystal systems as optimized by means of the AM05 XC functional and their respective a, b, and c (in Å) and the angles α, β, and γ (in °). The polymorphs are labeled with Greek letters following their introduction in Table 3.15. Those marked with (np) correspond to non-primitive unit cells, which represent alternative representations of the same crystal structure. The reference lattice parameters, included for comparison, are sourced from (SPENCER *et al.*, 2022).

	Lattice constants (Å)						Angles (°)		
	This work			Reference			This work		
Polymorph	a	b	c	a	b	c	α	β	γ
γ'-Al_2O_3	4.74	2.87	6.75				100.73	94.88	90.87
θ-Al_2O_3	6.09	6.09	5.64				76.38	103.62	152.26
θ-Al_2O_3 (np)	11.81	2.93	5.64	11.81	2.91	5.62	90.00	104.06	90.00
λ-Al_2O_3	3.19	12.09	5.16				90.00	105.09	90.00
κ-Al_2O_3	4.85	8.34	8.96	4.6	8.18	8.87	90.00	90.00	90.00
ω1-Al_2O_3	5.60	5.60	4.95				90.00	90.00	90.00
ω2-Al_2O_3	4.61	9.59	3.10				90.00	90.00	90.00
ω3-Al_2O_3	7.03	4.81	4.95				90.00	90.00	90.00
ω4-Al_2O_3	4.80	5.05	13.99				90.00	90.00	90.00
ω5-Al_2O_3	4.89	7.27	4.75				90.00	90.00	90.00
ω6-Al_2O_3	4.63	4.63	6.94				90.00	90.00	90.00
τ-Al_2O_3	7.93	7.93	23.74	5.6	5.6	23.66	90.00	90.00	90.00
τ'-Al_2O_3	3.29	3.29	4.73				90.00	90.00	90.00
α'-Al_2O_3	5.28	5.28	5.28				54.27	54.27	54.27
α'-Al_2O_3 (np)	4.78	4.78	13.04				90.00	90.00	120.00
α-Al_2O_3	5.14	5.14	5.14				55.33	55.33	55.33
α-Al_2O_3 (np)	4.77	4.77	13.03	4.75	4.75	12.97	90.00	90.00	120.00
χ''-Al_2O_3	5.09	5.09	8.28				90.00	90.00	120.00
χ'-Al_2O_3	3.00	3.00	7.84				90.00	90.00	120.00
κ'-Al_2O_3	6.87	6.87	4.60				90.00	90.00	120.00
χ-Al_2O_3	2.87	2.87	9.29				90.00	90.00	120.00
δ-Al_2O_3	7.72	7.72	7.72				109.47	109.47	109.47
δ-Al_2O_3 (np)	8.91	8.91	8.91				90.00	90.00	90.00
γ''-Al_2O_3	3.60	3.60	3.60				90.00	90.00	90.00
$\delta\delta$-Al_2O_3	4.58	4.58	4.58				90.00	90.00	90.00
γ-Al_2O_3	7.97	7.97	23.93	7.9	7.9	7.9	89.60	90.35	90.00
δ'-Al_2O_3	9.86	9.86	9.86				109.47	109.47	109.47
δ'-Al_2O_3 (np)	11.39	11.39	11.39				90.00	90.00	90.00

[a] xx

3.5.2 Al_2O_3 - Stability and equilibrium parameters

The 0 K static equilibrium volume (V_0), static energies (E_0), bulk modulus (B_0), and their respective derivatives (B') of the phases were determined using four different equations of state: Birch, Murnaghan, Birch-Murnaghan, and Vinet. The calculations in this work demonstrate significant concordance with results reported in the literature, thereby confirming previous well-established findings that identify the alpha corundum

phase as the most energetically favorable (ZHOU *et al.*, 2024). However, our calculations suggest the existence of other previously unreported polymorphs that may overcome even the most favorable second phase documented in the literature. This implies a revised stability sequence, encompassing α-, κ-, δ-, θ-, ω4-, and γ- Al_2O_3 phases, arranged sequentially as the most stable phases. The results are listed in Tab. 3.17.

TABLE 3.17 – Equilibrium parameters of Al_2O_3 polymorphs calculated using Vinet and Birch-Murnaghan EOS (in parentesis).

Space group	Label	$-E_0$ (eV)	V_0 (Å^3)	B_0 (GPa)	B'
P1	γ'	37.690 (36.970)	48.790 (45.972)	213.883 (217.053)	4.527 (4.083)
C2/m (prim.)	θ	38.221 (37.351)	47.338 (48.162)	215.971 (207.628)	4.104 (4.159)
C2/m (conv.)	θ	38.215 (37.350)	47.357 (48.325)	218.128 (211.205)	3.644 (3.769)
$P2_1/c$	λ	37.935 (37.064)	48.052 (49.050)	214.135 (205.969)	3.911 (4.081)
C2/c (prim.)	$\theta 2$	37.751 (36.924)	58.941 (59.444)	168.671 (163.292)	3.798 (4.087)
C2/c (conv.)	$\theta 2$	38.149 (37.405)	42.940 (43.836)	243.654 (233.838)	3.734 (3.935)
$Pna2_1$	κ	38.238 (37.319)	45.381 (46.296)	227.589 (218.690)	3.944 (3.986)
$Cmc2_1$	$\omega 1$	37.878 (37.182)	66.752 (67.648)	150.996 (146.783)	4.100 (4.085)
Pnnm	$\omega 2$	37.410 (36.712)	68.459 (69.436)	149.004 (144.530)	4.201 (4.403)
Pbcn	$\omega 3$	37.954 (36.933)	41.941 (42.861)	247.311 (236.573)	3.946 (3.968)
Pbca	$\omega 4$	38.171 (37.163)	42.464 (43.403)	243.648 (233.422)	4.042 (4.001)
Pnma	$\omega 5$	37.606 (36.601)	42.265 (43.400)	241.205 (231.321)	4.232 (4.016)
Cmcm	$\omega 6$	37.059 (36.000)	41.036 (42.194)	245.603 (232.713)	4.143 (4.224)
$P4_12_12$	τ	38.225 (37.322)	46.780 (47.691)	218.785 (210.314)	3.973 (3.971)
$P\bar{4}m2$	τ'	34.989 (34.084)	51.310 (52.430)	187.881 (178.660)	4.014 (4.262)
$R\bar{3}$ (prim.)	α'	38.061 (37.075)	45.139 (46.072)	224.059 (214.358)	4.270 (4.205)
$R\bar{3}$ (conv.)	α'	38.066 (37.402)	45.277 (43.824)	228.072 (232.442)	3.958 (4.104)
$R\bar{3}c$ (prim.)	α	38.402 (37.404)	42.931 (43.825)	243.063 (232.581)	3.967 (4.169)
$R\bar{3}c$ (conv.)	α	38.401 (37.404)	42.922 (43.824)	242.726 (232.448)	3.949 (4.118)
$P3_121$	χ''	37.579 (36.881)	61.897 (62.839)	160.805 (158.631)	3.608 (3.281)
$P\bar{3}m1$	χ'	36.931 (36.207)	60.941 (61.675)	166.245 (161.488)	3.867 (4.332)
$P6_3mc$	κ'	35.826 (34.913)	47.157 (48.606)	208.449 (197.527)	3.674 (4.025)
$P\bar{6}m2$	χ	37.340 (36.380)	66.179 (67.590)	147.224 (141.562)	4.163 (4.516)
$Ia\bar{3}$ (prim.)	δ	38.225 (37.253)	44.309 (45.235)	230.108 (220.079)	4.153 (4.206)
$Ia\bar{3}$ (conv.)	δ	38.223 (37.254)	44.350 (45.328)	227.892 (222.138)	3.773 (3.359)
$Pm\bar{3}m$	γ''	32.468 (31.479)	46.558 (47.709)	198.078 (187.254)	3.964 (4.076)
$Pn\bar{3}m$	$\delta\delta$	33.977 (33.046)	48.202 (49.275)	193.261 (185.390)	3.371 (3.805)
$Fd\bar{3}m$	γ	38.143 (37.248)	47.204 (48.126)	215.778 (207.563)	4.029 (4.056)
$Ia\bar{3}d$ (prim.)	δ'	36.714 (35.803)	46.264 (47.209)	215.830 (206.094)	4.224 (4.265)
$Ia\bar{3}d$ (conv.)	δ'	36.718 (35.807)	46.206 (47.245)	217.564 (210.134)	3.263 (3.756)

Only the curves obtained using the Vinet EOS are considered to ensure consistency with the calculations of other oxides. Additionally, thes results yield slightly lower values

for E_0, althougth the differences between the various EOS types are only about 0.01 eV. These curves are illustrated in Fig. 3.17.

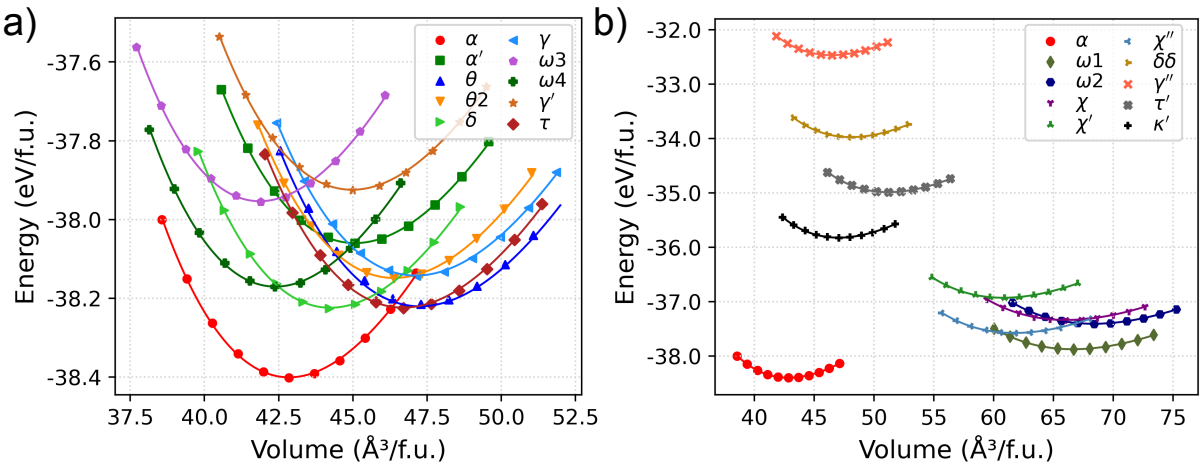

FIGURE 3.17 – Calculated total energies vs. volume for selected Al_2O_3 polymorphs. The solid lines represent fits using the Vinet EOS. Energies are normalized per formula formula unit. Panel (a) groups polymorphs with comparable and moderate volumes, while panel (b) includes less energetically stable polymorphs, including those with low atomic density.

3.5.3 Al_2O_3 - Pressure-induced phase transitions

The same methodology used to identify pressure-induced phase transitions for the In_2O_3 and Ga_2O_3 polymorphs was applied, i.e., the enthalpies as function of pressure $H = H(p)$ and their differences $\Delta H(p)$ were determined. Both curves are shown in Fig. 3.15. Two main groups of phase transitions are identified: one occurring at pressures above 50 GPa and another at negative pressures. The latter can be further divided into two main groups, with the first occurring at pressures between -4 and -13 GPa and the second at pressures below -15 GPa.

Phase transitions induced by negative pressures occur when a material undergoes structural changes under tensile stress rather than compression. In physical terms, this means that the material's crystal structure becomes energetically unstable under expansion, leading to a reconfiguration into a new phase with lower free energy. These transitions can happen naturally in geological processes, such as in minerals subjected to tectonic stress, inclusions within expanding host minerals, or porous materials experiencing ice formation (ERVINE; OSBORN, 1951). Experimentally, they are observed in thin films under tensile strain (JEURGENS *et al.*, 2002), porous materials like aerogels during liquid evaporation, systems undergoing rapid expansion after mechanical constraints are removed, and this behaviour may nearly describe pseudomorphic growth on a substrate with larger lattice constants. In these cases, the epitaxial layer is forced

to expand to match the substrate, generating a state of strain that can induce structural changes (WAN *et al.*, 2021). This is particularly relevant in thin film growth, where lattice adaptation can lead to metastable phases that would not occur under normal equilibrium conditions.

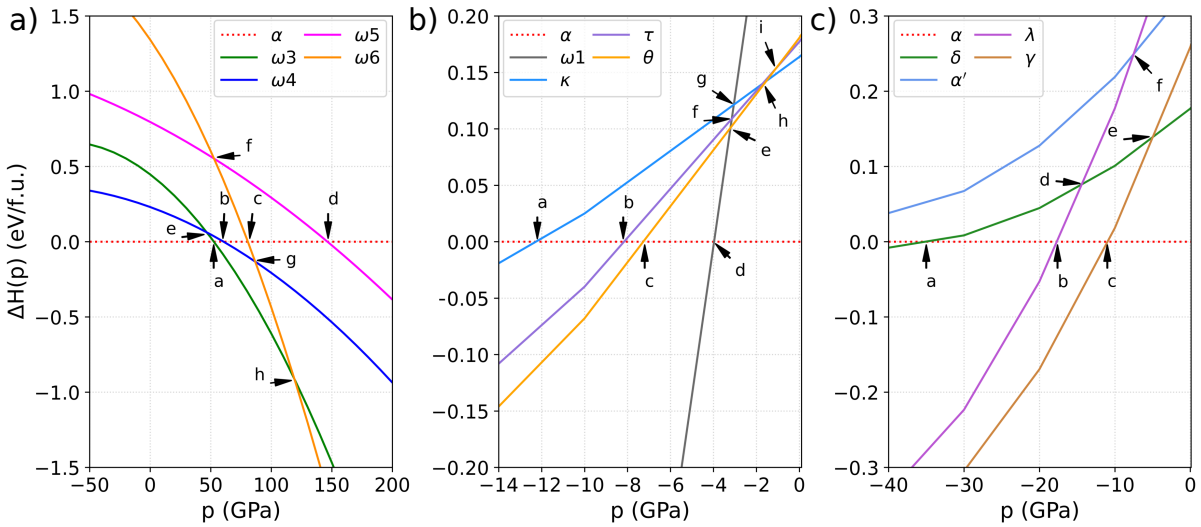

FIGURE 3.18 – Difference in enthalpy per formula unit, $\Delta H(p) = H(p) - H_\alpha(p)$, as a function of hydrostatic pressure p for the most energetically stable polymorphs. Here, $H_\alpha(p)$ denotes the enthalpy of the most stable polymorph, the α corundum polymorph, chosen as the reference (indicated by the red dashed zero line). Arrows indicate phase transitions between different polymorphs.

3.5.4 Al_2O_3 - Phonons and thermodynamics properties

The enthalpy curves, their differences, and the E_0 values provide strong evidence of dynamic instability. To systematically assess thermodynamic stability and subsequently investigate other properties, we analyze the impact of polymorphism on lattice dynamics through phonon calculations and their corresponding density of states (DOS). To evaluate the accuracy of our phonon calculations for Al_2O_3 polymorphs, we compare the results with experimental data from inelastic neutron scattering for the stable α-corundum phase (SCHOBER *et al.*, 1993). In this comparison, a non-primitive hexagonal cell containing 30 atoms was employed. The strong agreement with experimental results, as shown in Figure 3.19, validates the reliability of our computational approach.

Phonon spectra were obtained for all polymorphs, except for those with 160 atoms, where the required number of displacements would lead to over 900 calculations, rendering the task computationally prohibitive. As a result of the phonon analysis, the number of dynamically stable polymorphs was significantly reduced to just ten–i.e., those that did not exhibit imaginary frequencies and were thus considered in all subsequent analyses.

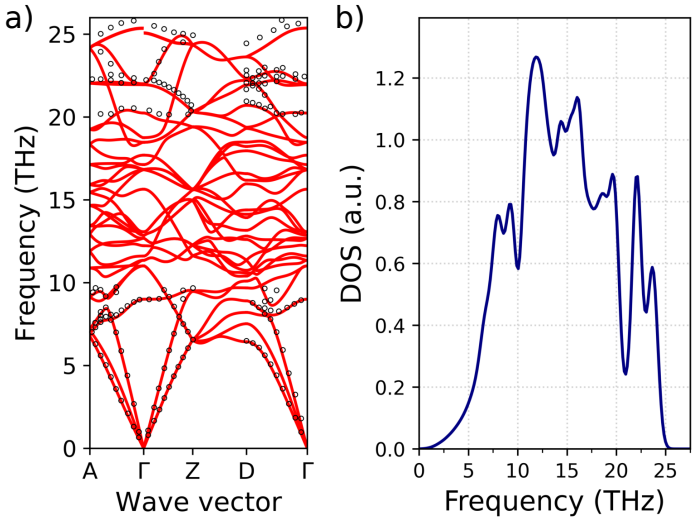

FIGURE 3.19 – Phonon dispersion curves (a) and vibrational density of states (b) for α-corundum, calculated using a non-primitive hexagonal unit cell with 30 atoms. In (a), the red open circles represent experimental data from inelastic neutron scattering (SCHOBER *et al.*, 1993).

These stable polymorphs include the trigonal-rhombohedral α-corundum and α' phases, as well as the monoclinic θ and $\theta 2$ phases, the cubic bixbyite δ, the cubic γ', and four orthorhombic phases: $\omega 1$, $\omega 2$, $\omega 3$, and $\omega 4$.

The phonon spectra and the corresponding DOS for six of these dynamically stable polymorphs are presented in Figure 3.20. As in the case of previously studied oxides, the Debye temperatures were also extracted from these calculations to analyze the heat capacity behavior at low temperatures. The resulting values are listed in Table 3.18.

TABLE 3.18 – Parameters of the Debye law for the dinamically stable Al_2O_3 polymorphs: the Debye temperature θ_D and the Debye frquency ν_D compared with experimental values found in the literature.

Polymorph	θ_D (K)	ν_D (THz)	θ_D (K) - Refe.
α-Al_2O_3	1025	134.2	1042 [a], 1044 [b] 1100 [c]
γ'-Al_2O_3	1259	164.8	–
θ-Al_2O_3	879	115.1	–
$\theta 2$-Al_2O_3	736	96.4	–
$\omega 1$-Al_2O_3	821	107.5	–
$\omega 2$-Al_2O_3	1012	132.5	–
$\omega 3$-Al_2O_3	1307	171.1	–
$\omega 4$-Al_2O_3	912	119.4	–
α'-Al_2O_3	969	126.9	–
δ-Al_2O_3	985	129.0	–

[a](VISWANATHAN, 1975), [b](CHUNG; SIMMONS, 1968), [c](SHI *et al.*, 2022).

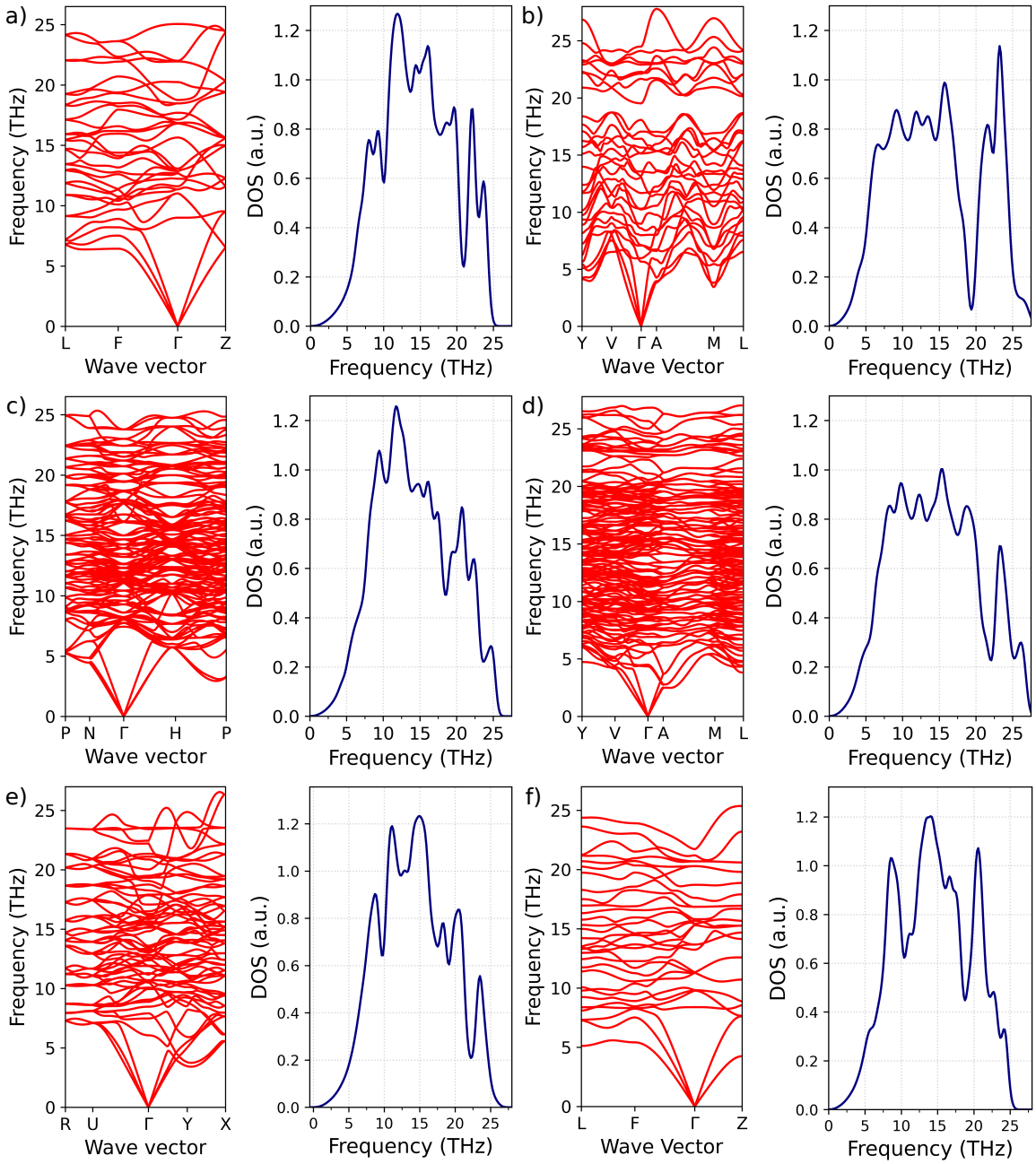

FIGURE 3.20 – Phonon dispersion relations vs. high-symmetry lines (left panels) and phonon density of states (DOS) vs. frequency for five statically and dynamical polymorphs: (a) α (R$\bar{3}$c, 10 atoms), (b) θ (C2/m, 10 atoms), (c) δ (Ia$\bar{3}$, 40 atoms), (d) $\theta 2$ (C2/c, 40 atoms), (e) $\omega 3$ (Pbcn, 20 atoms), and (f) $\omega 2$ (Pnnm, 10 atoms) with varying symmetry and number of atoms in the primitive unit cell. The DOS is normalized to a formula unit.

3.5.5 Al_2O_3 - Temperature-induced phase transitions

The total free energy $F(T)^{\text{tot}}$ and their differences $\Delta F(T)^{\text{tot}}$, used to analyze the temperature-induced phase transitions of thermodynamically stable polymorphs, are shown in Figure 3.21. From the Figure 3.18, three phase transitions are identified. At

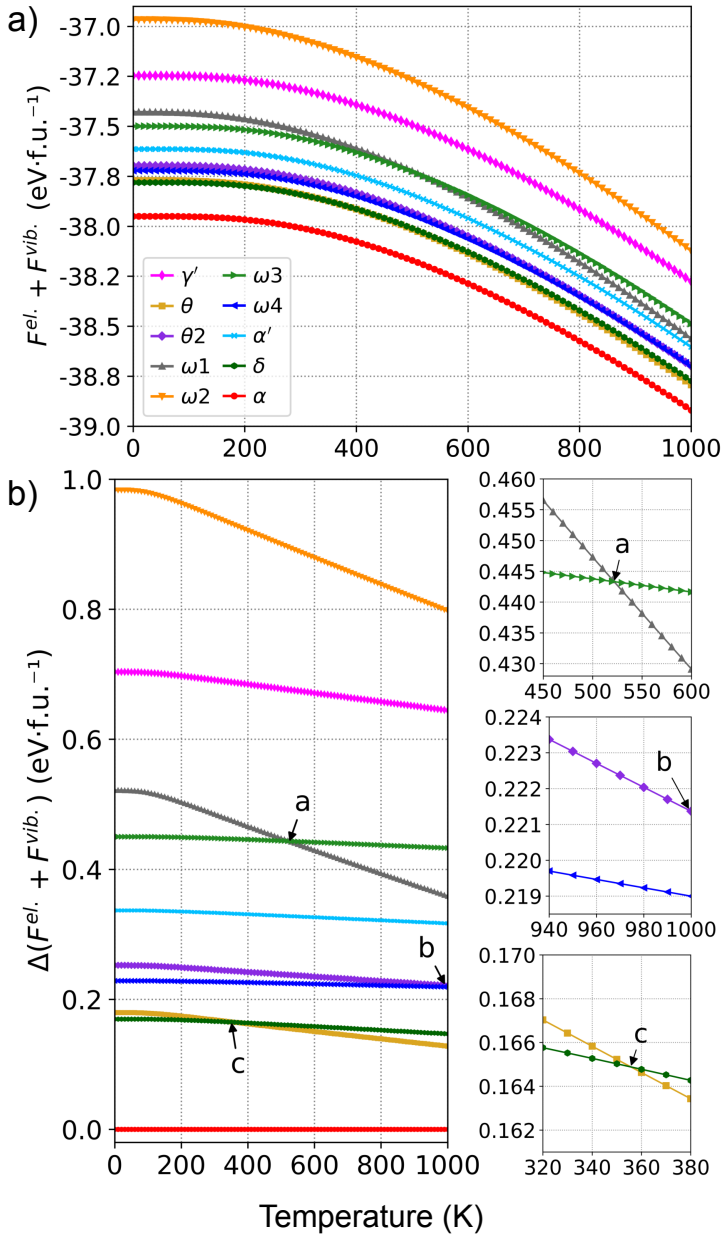

FIGURE 3.21 – Total free energy $F^{\mathrm{tot}}(T)$ as a function of temperature for the ten dynamically stable phases. (a) The total free energy, given by $F^{\mathrm{tot}}(T) = F^{\mathrm{el}} + F^{\mathrm{vib}}$, is shown in eV per formula unit as a function of temperature. (b) The energy variation, defined as $\Delta F^{\mathrm{tot}}(T) = F^{\mathrm{tot}}(T) - F^{\mathrm{tot}}\alpha(T)$, is presented in eV per formula unit, where $F^{\mathrm{tot}}\alpha(T)$ corresponds to the total free energy of the α-corundum polymorph, chosen as the reference (red zero line) since it is the most stable phase. Arrows indicate potential phase transitions between different polymorphs, with zoomed-in views of these transitions displayed in the right panels of (b).

524 K, the $\omega 1$ phase becomes more stable than $\omega 3$ (arrow "a"). At 357 K, the θ structure becomes more stable than the δ phase (arrow "c"). Extrapolating to higher temperatures, at 1109 K, the $\theta 2$ phase surpasses the stability of the $\omega 4$ polymorph (arrow "b"). While pressure drives an $\alpha \rightarrow \omega 3$ transition, temperature has little effect on this process. The analysis indicates that Al_2O_3 undergoes a phase transition at 3048 K,

from ω_2 to α–well above the α-corundum melting point ($\approx$ 2327 K). This underscores the exceptional thermal stability of α phase, as the thermal energy required to overcome the enthalpy barrier exceeds its melting point.

3.5.6 Al_2O_3 - Electronic structure

As expected, standard DFT underestimates fundamental band gaps. As noted in Sec. 3.5.1, for Al_2O_3 polymorphs, the electronic structure correction is simplified since only DFT$-1/2$ is used. Overall, the band structures closely resemble those of other studied oxides, differing mainly in band gap values, i.e., VBM and CBM. This similarity arises from the nature of group III atoms and the structural resemblance of sesquioxides within the same crystal system.

3.5.6.1 Al_2O_3 - Energy band gaps

Table 3.19 exhibits results of the energy band gaps obtained within DFT and DFT$-1/2$ approach for the ten dinamically stable polymorphs under study including reference values of the α phase. The electronic band structures are illustrated in Figure 3.19.

TABLE 3.19 – Energy band gaps in eV for all Al_2O_3 polymorphs. Indirect gaps are distinguished from direct ones in parenthesis. For the α phase a non-primitive cell was used. Refs: *a*) (SAKAGUCHI *et al.*, 2016) calculations using HSE03 and experiment using VUV transmittance; *b*) (SPENCER *et al.*, 2022) experiment using electron energy-loss spectroscopy.

	Band gap (eV)		Band gap (eV) - Refe.	
Polymorph	DFT	DFT$-1/2$	Calculated	Experimental
γ'-Al_2O_3	4.675	7.002	-	-
θ-Al_2O_3	4.911 (4.628)	7.463 (7.139)	-	-
δ-Al_2O_3	4.422	7.034	-	-
$\theta 2$-Al_2O_3	4.740	7.431	-	-
$\omega 1$-Al_2O_3	4.313 (4.312)	6.710	-	-
$\omega 2$-Al_2O_3	3.596	6.028 (6.028)	-	-
$\omega 3$-Al_2O_3	5.568	7.942	-	-
$\omega 4$-Al_2O_3	5.700	8.115	-	-
α'-Al_2O_3	5.947 (5.932)	8.414 (8.399)	-	-
α-Al_2O_3	6.128	8.523	8.0 [a]	8.5 [a], 8.8 [b]

Across all polymorphs, a pronounced dispersion is observed around the Γ point, whereas the O $2p$-derived uppermost valence bands display significantly weaker dispersion. The CBM exhibits significant hybridization between Al $3s$ and O $2s$ orbitals and is tipically composed of 57% Al $3s$ and 43% O $2s$, indicating a notable contribution

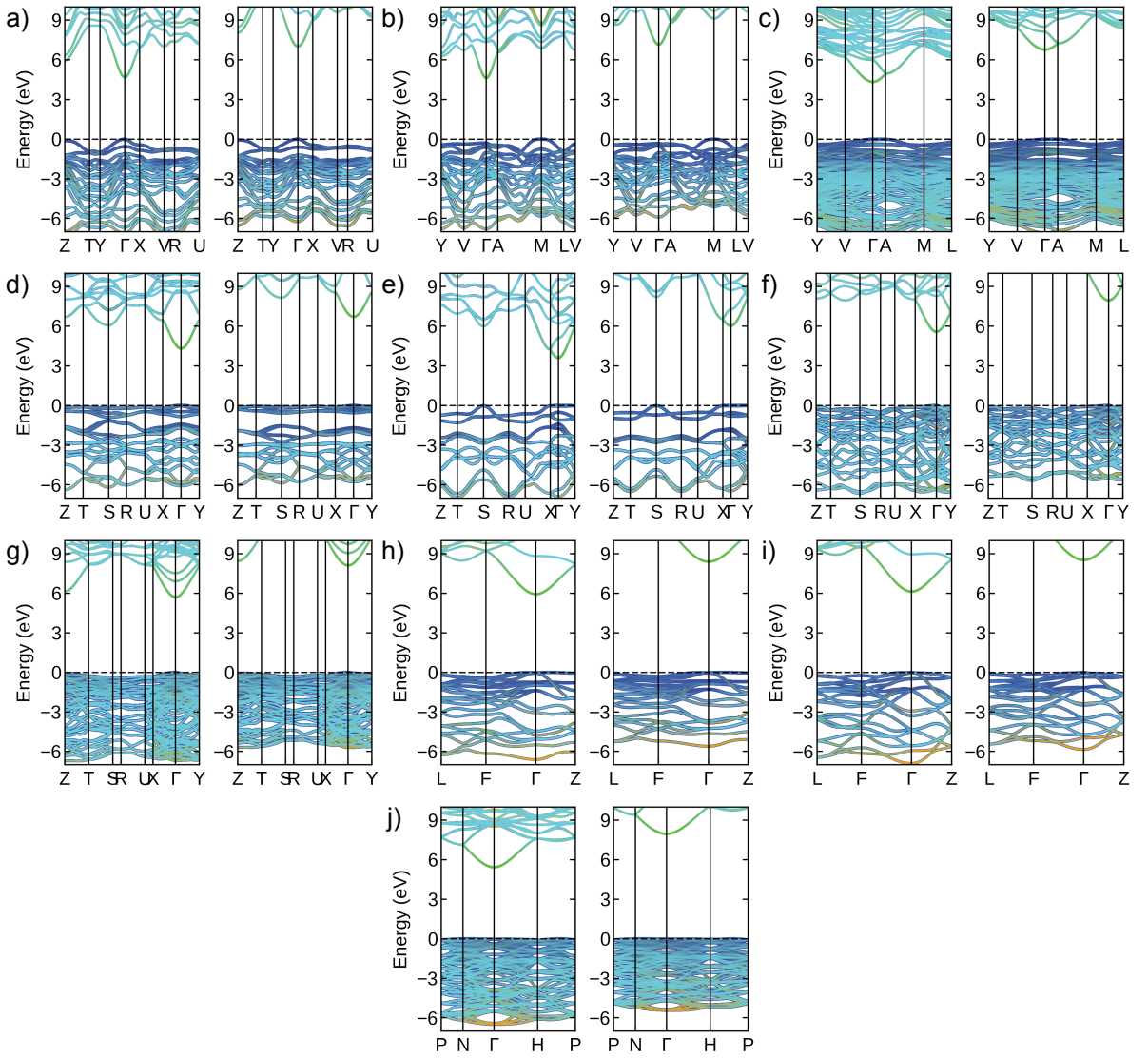

FIGURE 3.22 – Electronic band structure of the dinamically stable polymorphs of Al_2O_3. Al $3p$ and Al $3s$ levels are depicted in light blue and yellow respectivelly while O $2p$ states are illustrated in dark blue and O $2s$ states in green. The ten polymorphs are represented in standard DFT (left panels) and DFT$-1/2$ (right panels) as (a) γ'-, (b) θ-, (c) θ2-, (d) ω1-, (e) ω2-, (f) ω3-, (g) ω4-, (h) α'-, (i) α-, and (j) δ phases.

from oxygen suggesting that the electronic structure of is not solely dictated by the metal cation states but also involves the oxygen anion states. The presence of O $2s$ in the CBM is somewhat unusual in oxides, where conduction bands are typically dominated by metal-derived states (e.g., Al $3s$ and $3p$). This contribution may be attributed to the strong sp hybridization between Al and O, leading to an increased covalent character in the Al–O bonding.

Within the DFT$-1/2$ framework, most polymorphs exhibit direct band gaps, with the exception of θ-, ω2-, and α'-Al_2O_3. In the case of standard DFT calculations predict an indirect band gap for the ω1-phase but not for the ω2-phase. However, the largest

difference found between direct and indirect gaps was approximately 0.3 eV.

3.5.7 Al_2O_3 - Effective masses

Despite exhibit insulating properties being, the effective mass of charge carriers in Al_2O_3 remains relevant for various applications. In electronic devices, it influences dielectric properties in MOSFETs, charge carrier dynamics at semiconductor interfaces, and tunneling effects. In defect-related conduction, vacancy-induced states within the bandgap can enable hopping transport, where effective mass plays a key role in charge mobility. Radiation shielding applications rely on how charge carriers respond to high-energy excitations, impacting recombination and defect formation. Additionally, in photocatalysis and bandgap engineering, the effective mass affects charge transport efficiency (BORISOVA; CASTRO, 2013) (BORISOVA; CASTRO, 2013; CHOI *et al.*, 2020; NOVIKOV *et al.*, 2023). Thus, these results were considered and analyzed. Table 3.20 summarizes the effective masses and directions.

TABLE 3.20 – Electron effective masses m^* (in units of free electron mass m_0) for de In_2O_3 polymorphs provided for two directions in the BZ within DFT and DFT$-1/2$ framework. For comparison, theoretical and experimental values from the literature are also listed.

	Effective masses				Effective masses - Ref.	
Polymorph	Direction	DFT (DFT$-1/2$)	Direction	DFT (DFT$-1/2$)	Calculated	Experiment
γ'-Al_2O_3	ΓY	0.372 (0.494)	ΓX	0.391 (0.522)	–	–
θ-Al_2O_3	ΓV	0.391 (0.525)	ΓA	0.384 (0.527)	–	–
θ2-Al_2O_3	ΓV	0.390 (0.526)	ΓA	0.388 (0.530)	–	–
ω1-Al_2O_3	ΓS	0.462 (0.607)	ΓZ	0.421 (0.557)	–	–
ω2-Al_2O_3	ΓX	0.540 (0.706)	ΓY	0.446 (0.585)	–	–
ω3-Al_2O_3	ΓX	0.373 (0.497)	ΓY	0.370 (0.499)	–	–
ω4-Al_2O_3	ΓX	0.380 (0.502)	ΓY	0.384 (0.512)	–	–
α'-Al_2O_3	ΓF	0.398 (0.522)	ΓZ	0.422 (0.549)	–	–
α-Al_2O_3	ΓF	0.392 (0.512)	ΓZ	0.393 (0.513)	0.39–0.41 [a]	0.30-0.42 [a]
δ-Al_2O_3	ΓN	0.385 (0.515)	ΓH	0.388 (0.517)	–	–

[a] (PEREVALOV *et al.*, 2007)

Similarly to the other oxides, the calculation of the effective masses is challenging due to the dispersion of the flat VBM and low crystalline symmetry (low parabolicity of the VBM), and only the electron effective masses can be reliably provided using the standard calculation model.

3.5.8 Al_2O_3 - Optical, dielectric, and excitonic properties

To compute the excitonic properties of the analyzed polymorphs, their optical characteristics were extracted and examined. The dielectric functions $\varepsilon(\omega)$ were

evaluated over a broad energy spectrum, and the averaged high-frequency dielectric constants, ε_∞, were used to determine the corresponding excitonic binding energies (E_b in eV) and excitonic Bohr radii (r_B in Å). These values are presented in the Table 3.21.

TABLE 3.21 – Averaged electron effective masses m^* (in units of the free electron mass m_0), averaged electronic dielectric constants ε_∞ (derived exclusively from DFT+$A-1/2$), excitonic Bohr radii r_B (in Å), and exciton binding energies E_b (in eV) for the In_2O_3 polymorphs. For ε_∞, a comparison with the experimental reference value from the literature is also provided. These quantities are computed using the Wannier-Mott model without dynamical corrections to dielectric screening. Results from DFT+$A-1/2$ are presented, with standard DFT values given in parentheses.

Polymorph	$m^*(m_0)$	ε_∞	ε_∞ - Ref.	E_b (eV)	r_B (Å)
γ'-Al_2O_3	0.513 (0.382)	2.505 (3.310)	–	1.111 (0.474)	2.59 (4.59)
θ-Al_2O_3	0.523 (0.388)	2.416 (3.225)	–	1.218 (0.507)	2.45 (4.40)
θ2-Al_2O_3	0.528 (0.389)	1.756 (2.390)	–	2.330 (0.927)	1.76 (3.25)
ω1-Al_2O_3	0.605 (0.442)	1.983 (2.606)	–	2.092 (0.884)	1.74 (3.12)
ω2-Al_2O_3	0.563 (0.493)	1.967 (2.601)	–	1.979 (0.991)	1.85 (2.79)
ω3-Al_2O_3	0.494 (0.372)	2.631 (3.404)	–	0.971 (0.436)	2.82 (4.85)
ω4-Al_2O_3	0.514 (0.382)	2.504 (3.323)	–	1.116 (0.471)	2.58 (4.60)
α'-Al_2O_3	0.515 (0.410)	2.474 (3.229)	–	1.145 (0.535)	2.54 (4.17)
α-Al_2O_3	0.503 (0.393)	2.032 (2.720)	3.0 [a]	1.656 (0.722)	2.14 (3.67)
δ-Al_2O_3	0.515 (0.387)	2.428 (3.223)	–	1.188 (0.506)	2.49 (4.41)

[a] (SPENCER *et al.*, 2022)

4 Comparative analysis

In this chapter, the results obtained for the oxides and their respective polymorphs are systematically compared. The analysis aims to identify general trends, underlying physical mechanisms, and key differences among these materials. To ensure a more coherent comparison, only polymorphs sharing the same crystal structure and space group are considered to exemplify the general behavior. Particular emphasis is placed on the structural, electronic, and optical properties, examining how variations in cation species and crystal structure influence their behavior. Furthermore, the broader implications of these findings for potential applications are discussed.

4.1 General comparison

Table 4.1 explicitly indicates which polymorphs of the examined oxides share the same crystal system and space group. This classification provides a basis for a more direct comparison of their structural, electronic, and optical properties, helping to identify trends and correlations among different materials.

TABLE 4.1 – Comparison of polymorphs of In_2O_3, Ga_2O_3, and Al_2O_3 that share the same crystal structure and space group, with the stable phases of each oxide indicated in parentheses.

Polymorphs			Crystal system	Space-group
α-In_2O_3	α-Ga_2O_3	α-Al_2O_3 (stable)	Rhombohedral	$R\bar{3}c$
δ-In_2O_3 (stable)	δ-Ga_2O_3	δ-Al_2O_3	Cubic bixbyite	$Ia\bar{3}$
	β-Ga_2O_3 (stable)	θ-Al_2O_3	Monoclinic	C2/m
$\omega 1$-In_2O_3		$\omega 3$-Al_2O_3	Orthorhombic	Pbcn
$\omega 3$-In_2O_3		$\omega 4$-Al_2O_3	Orthorhombic	Pbca

4.1.1 Structural parameters

In Table 4.2, structural parameters are compared, revealing a general trend of decreasing lattice constants and, consequently, volume per formula unit, from In to Al in

all cases. With the exception of monoclinic polymorphs, another observed trend is that crystals with lower symmetry tend to exhibit a smaller volume per formula unit. This can be attributed to the fact that lower symmetry generally leads to less efficient atomic packing and, consequently, smaller volumes per formula unit. In contrast, higher symmetry promotes a more compact atomic arrangement and larger volume. Reduced symmetry can cause variations in bond angles and distances, stronger bonding constraints, and lattice distortions that further compress the structure. Notably, monoclinic polymorphs may exhibit exceptions due to specific atomic arrangements that allow for larger volumes despite lower symmetry.

Additionally, differences in atomic size and bond lengths among In, Ga, and Al play a significant role. As the atomic radius decreases from In to Al, packing efficiency increases, resulting in shorter, stronger bonds and a more compact structure. Indium's larger radius and longer bonds yield a less dense packing compared to aluminum's smaller, more tightly bonded structure.

TABLE 4.2 – Comparison of polymorphs of In_2O_3, Ga_2O_3, and Al_2O_3 that share the same crystal structure and space group, with the stable phases of each oxide indicated in parentheses.

	Lattice constants (Å)				Angles (°)		
Polymorphs	a	b	c	Volume (Å^3)	α	β	γ
α-In_2O_3	5.516	5.516	14.597	64.097	90.00	90.00	120.00
α-Ga_2O_3	5.002	5.002	13.467	48.637	90.00	90.00	120.00
α-Al_2O_3	4.774	4.774	13.027	42.851	90.00	90.00	120.00
δ-In_2O_3	10.169	10.169	10.169	65.732	90.00	90.00	90.00
δ-Ga_2O_3	9.303	9.303	9.303	50.314	90.00	90.00	90.00
δ-Al_2O_3	8.911	8.911	8.911	44.223	90.00	90.00	90.00
β-Ga_2O_3	12.295	3.050	5.815	52.935	90.00	103.74	90.00
θ-Al_2O_3	11.813	2.925	5.643	47.286	90.00	104.06	90.00
ω1-In_2O_3	5.621	5.529	7.976	61.970	90.00	90.00	90.00
ω3-Al_2O_3	4.953	4.812	7.032	41.899	90.00	90.00	90.00
ω3-In_2O_3	5.525	5.716	15.956	62.988	90.00	90.00	90.00
ω4-Al_2O_3	4.796	5.052	13.993	42.384	90.00	90.00	90.00

4.1.2 Equilibrium parameters

The thorough examination of the equilibrium parameter in Table 4.3 reveals consistent trends that can be attributed both to the nature of the cations (Al, Ga, or In) and to the particular crystal structures under consideration (trigonal corundum-like, cubic bixbyite, monoclinic, or orthorhombic). In terms of equilibrium energy ($-E_0$), Al_2O_3 consistently

displays the most negative values, reflecting higher energetic stability, whereas In_2O_3 shows the least negative values, indicative of comparatively lower stability. This ordering is closely tied to the ionic radii of the cations: Al^{3+} has the smallest ionic radius, resulting in stronger Al–O bonds and a more negative energy of formation, while In^{3+} has the largest ionic radius and thus weaker overall bonding and higher energy.

TABLE 4.3 – Equilibrium parameters (normalized per formula unit) of the selected polymorphs. E_0 represents the equilibrium energy, V_0 the equilibrium volume, B_0 the bulk modulus, and B' the pressure derivative of the bulk modulus.

	Equilibrium parameters			
Polymorph	$-E_0$	V_0	B_0	B'
α-In_2O_3	28.56	64.31	169.68	4.41
α-Ga_2O_3	30.83	48.74	215.72	4.55
α-Al_2O_3	38.40	42.92	242.73	3.95
δ-In_2O_3	28.69	66.09	161.23	4.70
δ-Ga_2O_3	30.78	50.31	205.54	4.75
δ-Al_2O_3	38.22	44.35	227.89	3.77
β-Ga_2O_3	30.91	53.05	193.66	4.51
θ-Al_2O_3	38.22	47.36	218.13	3.64
$\omega 1$-In_2O_3	28.47	62.12	175.16	4.47
$\omega 3$-Al_2O_3	37.95	41.94	247.31	3.95
$\omega 3$-In_2O_3	28.50	63.12	168.72	4.61
$\omega 4$-Al_2O_3	38.17	42.46	243.65	4.04

The equilibrium volume (V_0) follows an inverse trend with respect to ionic size, so Al_2O_3 tends to have the smallest volume and In_2O_3 the largest. However, structural factors also play a role: denser crystal structures often yield smaller equilibrium volumes. The bulk modulus (B0), which indicates the material's resistance to compression, is highest in Al_2O_3 and lowest in In_2O_3, with Ga_2O_3 occupying an intermediate position. This pattern is consistent with the relative strengths of metal–oxygen bonds and with the greater stiffness typically associated with smaller ionic radii. The derivative of the bulk modulus (B') usually lies between 3.6 and 4.7, tending to be slightly lower in Al_2O_3 and slightly higher in Ga_2O_3 and In_2O_3, which reflects how compressibility evolves under external pressure.

Within each oxide system, structural polymorphs (such as the α-, δ-, β-/θ-, and orthorhombic ωn- phases) exhibit variations in volume and rigidity that further highlight the interplay between crystal packing and cation size. Denser phases like α-Al_2O_3 or certain orthorhombic forms of Al_2O_3 generally show higher bulk moduli and lower compressibility. Overall, these trends can be ascribed to the combined effects of

cation size, metal–oxygen bond strength, and crystal packing density, with Al_2O_3 manifesting the strongest bonds and highest rigidity, In_2O_3 exhibiting more voluminous and compressible structures, and Ga_2O_3 demonstrating properties that bridge these two extremes.

From a technological perspective, the variations in the equilibrium parameters of Al_2O_3, Ga_2O_3, and In_2O_3 reflect differences in their chemical stability, mechanical rigidity, and density, which in turn influence their performance in a range of applications. Al_2O_3 exhibits the most negative formation energy, indicating high stability that makes it a preferred material for protective coatings, refractory components, and optical windows at elevated temperatures. Structural differences–such as the corundum-like α- phases, cubic bixbyite δ phases, and monoclinic or orthorhombic polymorphs–further influence material density and compressibility, with denser structures typically offering higher stiffness.

4.1.3 Electronic properties

Band gap and electron effective masses of the polymorphs in Table 4.4, calculated with both standard DFT and the DFT$-1/2$ or DFT$+A-1/2$ corrections, exhibit consistent trends governed by the nature of the cation and the crystal structure. In particular, Al_2O_3 shows the largest band gaps, Ga_2O_3 has intermediate values, and In_2O_3 features the smallest gaps. This outcome stems from the fact that the conduction band in these trivalent oxides arises primarily from the cation s-orbitals, which become increasingly diffuse as the cation radius grows. Al, having a smaller ionic radius, produces more localized orbitals and hence larger gaps, whereas In, with the largest radius, generates more delocalized orbitals and thus smaller gaps. Consequently, the effective masses follow a nearly opposite trend, since more diffuse orbitals typically result in broader conduction bands and smaller electron masses.

The crystal structure also plays a key role in determining both band gap and effective mass. The corundum-like rhombohedral phases (α) generally present higher gaps than the bixbyite (δ), monoclinc (β or θ), or orthorhombic (ωn) polymorphs. For instance, α-Al_2O_3 typically has a larger gap than other Al_2O_3 phases, and α-Ga_2O_3 also exceeds the gap values found in its β and δ counterparts. The orthorhombic and monoclinc phases of In_2O_3, in turn, exhibit the lowest band gaps among its polymorphs, whereas in Al_2O_3, the orthorhombic variants retain relatively high gaps, although not surpassing α-Al_2O_3. These structural differences reflect variations in density and coordination, which affect how the electronic bands are formed and consequently how wide or narrow they become.

Applying the DFT$-1/2$ correction for Al_2O_3 and the DFT$+A-1/2$ method for Ga_2O_3 and In_2O_3 substantially reduces the well-known underestimation of band gaps by

local or semilocal functionals. It also alters the curvature of the conduction band, thereby increasing the effective mass values slightly. These corrected results align more closely with experimental data and are of considerable importance when designing materials for electronic and optical applications. The general hierarchy of band gaps and effective masses remains the same after the correction, with Al_2O_3 consistently showing the highest gap and largest effective mass, Ga_2O_3 occupying an intermediate position, and In_2O_3 displaying the smallest gap and lowest mass. Such differences underscore the importance of carefully selecting both the oxide (Al_2O_3, Ga_2O_3, or In_2O_3) and its specific polymorph to optimize properties for applications such as high-voltage electronics, transparent conductive films, or insulating and protective layers.

TABLE 4.4 – Comparison of the energy band gaps (in eV) and average electron effective masses (in units of the electron rest mass, m_0) for the selected polymorphs. The results obtained using standard DFT, as well as DFT corrected with DFT+$A-1/2$ aor DFT$-1/2$ for Al_2O_3, are presented.

	Energy Band gap (eV)		Average m^* (m_0)	
Polymorph	DFT	DFT corrected	DFT	DFT corrected
α-In_2O_3	1.15	3.16	0.17	0.31
α-Ga_2O_3	3.01	5.09	0.23	0.40
α-Al_2O_3	6.13	8.52	0.39	0.51
δ-In_2O_3	1.21	3.21	0.18	0.33
δ-Ga_2O_3	2.55	4.71	0.24	0.40
δ-Al_2O_3	4.42	7.03	0.39	0.52
β-Ga_2O_3	2.30	4.64	0.23	0.41
θ-Al_2O_3	4.63	7.14	0.39	0.53
ω1-In_2O_3	0.96	2.98	0.15	0.30
ω3-Al_2O_3	5.57	7.94	0.37	0.50
ω3-In_2O_3	1.08	3.09	0.15	0.30
ω4-Al_2O_3	5.70	8.12	0.39	0.51

The systematic underestimation of band gaps by standard DFT methods is evident across all polymorphs, emphasizing the need for quasiparticle corrections while also highlighting the influence of structural and chemical factors. Notably, the corrected results reveal that α-Al_2O_3 exhibits a particularly large band gap (8.52 eV) and a relatively high effective mass (0.51 m_0), which reflects the strong ionic interactions and localized orbitals characteristic of the corundum-like phase. In contrast, the ω1- and ω3-In_2O_3 polymorphs display much smaller corrected gaps (approximately 3 eV) and lower effective masses (0.30 m_0), making them attractive for transparent conducting applications, provided that suitable doping strategies and growth techniques can be

established. The intermediate band gaps observed in β-Ga_2O_3 (4.64 eV) and δ-Ga_2O_3 (4.71 eV) further reinforce the growing interest in gallium oxide for high-voltage and high-frequency devices, where a balance between a larger band gap, reduced leakage currents, and moderate effective masses enables reasonable carrier mobilities. Similarly, the orthorhombic Al_2O_3 phases ($\omega 3$, $\omega 4$), with band gaps exceeding 7.9 eV, remain relatively unexplored but may hold promise for deep-ultraviolet optical elements or highly robust coatings requiring extreme chemical and thermal stability.

The variations in effective mass across these polymorphs follow a clear trend after quasiparticle correction, with a more pronounced enhancement in In_2O_3, followed by Ga_2O_3 and Al_2O_3. This trend arises from differences in the conduction band dispersion and the influence of quasiparticle self-energy corrections. In these group-13 oxides, the conduction band is primarily formed by the *s*orbitals of the cation, hybridized with the $2p$ orbitals of oxygen. The $5s$ orbitals of indium are more spatially extended than the $4s$ orbitals of gallium and the $3s$ orbitals of aluminum (HOUSECROFT; SHARPE, 2018), leading to a more dispersive conduction band within the DFT framework. Consequently, the quasiparticle correction, which generally reduces band dispersion, has a stronger impact on In_2O_3, resulting in a more significant increase in effective mass compared to Ga_2O_3 and Al_2O_3. In contrast, Al_2O_3 exhibits a less dispersive conduction band due to the more localized nature of the Al $3s$ orbitals and a stronger covalent character in Al–O bonding, which reduces the influence of quasiparticle corrections.

These trends emerge from the interplay between the cation's ionic radius, orbital hybridization, and the density of the crystal lattice, suggesting that further theoretical and experimental investigations could uncover new functionalities or improved performance in power electronics, optoelectronics, and protective materials. This is particularly relevant for the less-studied polymorphs, where unique combinations of high band gap, low density, or distinctive local coordination may enable unforeseen advances in device engineering.

4.1.4 Dielectric and excitonic properties

The analysis of the data in Table 4.5 reveals distinct trends related to both the cation characteristics and the crystal structures of the oxides. In terms of cation influence, the polarizability and the high-frequency dielectric constant (ε_∞) differ markedly among the materials. In_2O_3 exhibits consistently higher ε_∞ values–approximately 3.2 using standard DFT and up to around 5.2 with QP corrections–which can be attributed to the larger ionic radius and more diffuse orbitals of In^{3+}, resulting in increased polarizability. In contrast, Ga_2O_3 shows intermediate ε_∞ values (approximately 2.1–2.9 in DFT and 4.1–4.3 when QP-corrected), reflecting a moderate level of polarizability, while Al_2O_3 exhibits the lowest ε_∞ values (around 2.0–2.6 in DFT and 2.7–3.2 in the QP-corrected calculations) due to

the smaller size and reduced polarizability of the Al^{3+} ion.

TABLE 4.5 – Comparison of the high-frequency dielectric constant ε_∞, exciton binding energy (E_b in eV), and excitonic Bohr radius (r_B) for various polymorphs of In_2O_3, Ga_2O_3, and Al_2O_3 calculated using both standard DFT and DFT$-1/2$ or DFT$+A-1/2$ corrected methods (labeled as DFT corr.). Literature reference values for ε_∞ are also provided according values already cited in the previous chapter.

	ε_∞			E_b (eV)		r_B (Å)	
Polymorph	DFT	DFT corr.	Ref.	DFT	DFT corr.	DFT	DFT corr.
α-In_2O_3	3.17	4.94		0.09	0.17	15.56	8.38
α-Ga_2O_3	2.11	4.32		0.17	0.28	9.68	5.94
α-Al_2O_3	2.03	2.72	3.20	1.66	0.72	2.14	3.67
δ-In_2O_3	3.04	4.52	4.80	0.09	0.17	13.51	7.18
δ-Ga_2O_3	2.86	4.23		0.18	0.30	9.28	5.65
δ-Al_2O_3	2.43	3.22		1.19	0.51	2.49	4.41
β-Ga_2O_3	2.74	4.09	3.95	0.19	0.33	9.25	5.38
θ-Al_2O_3	2.42	3.22		1.22	0.51	2.45	4.40
ω1-In_2O_3	3.24	5.22		0.07	0.15	18.66	9.27
ω3-Al_2O_3	2.63	3.22		0.97	0.44	2.82	4.85
ω3-In_2O_3	3.19	5.09		0.08	0.16	17.48	8.86
ω4-Al_2O_3	2.50	3.22		1.12	0.47	2.58	4.60

Regarding excitonic properties, a higher ε_∞ generally leads to enhanced Coulomb screening, which in turn results in less strongly bound excitons characterized by lower binding energies (E_b) and larger excitonic Bohr radii (r_B). Consistent with this understanding, In_2O_3 shows very low exciton binding energies of (approximately 0.07–0.17 eV) and relatively large excitonic Bohr radii (about 15–18 in DFT, reducing to 8–9 in QP corrected calculations). Conversely, Al_2O_3, with its lower dielectric constant, exhibits significantly higher exciton binding energies (around 1–1.2 eV or greater depending on the method) along with much smaller excitonic Bohr radii (ranging from approximately 0.7 to 2.8). Ga_2O_3 falls between these two extremes, displaying intermediate values for both exciton binding energy and Bohr radius.

Structural factors also play a crucial role in determining the observed properties. Polymorphs with trigonal/rhombohedral symmetry and those with cubic bixbyite structures present only minor variations in ε_∞ values, maintaining the overall trend of In $>$ Ga $>$ Al. However, monoclinic and orthorhombic polymorphs exhibit anisotropic electronic distributions, which affect the degree of electronic screening. In some orthorhombic structures of In_2O_3 and Al_2O_3, the QP-corrected ε_∞ values are notably higher, a result likely due to specific bonding arrangements and angles that enhance

polarizability in particular directions.

The application of the QP correction generally increases the ε_∞ values, particularly for In_2O_3 and Ga_2O_3, suggesting a more accurate description of the electronic band gap and screening effects. This correction also influences the excitonic parameters, as the enhanced ε_∞ leads to a reduction in exciton binding energy and an adjustment of the excitonic Bohr radius. The impact of this correction is less pronounced in Al_2O_3, which may be attributed to its inherently lower polarizability.

The trends outlined have important implications for technological applications, particularly in the fields of optoelectronics and semiconductor device engineering. The observed variations in the high-frequency dielectric constant, exciton binding energy, and excitonic Bohr radius directly influence charge screening and exciton behavior. For instance, materials with higher dielectric constants and lower exciton binding energies, such as In_2O_3, may facilitate exciton dissociation, which is crucial for enhancing the efficiency of photovoltaic cells and photodetectors. Conversely, materials like Al_2O_3, which exhibit higher exciton binding energies and smaller excitonic Bohr radii, can be beneficial in applications where strong exciton confinement is desired, such as in light-emitting devices and high-performance sensors.

Moreover, the influence of crystal structure on these properties indicates that tuning the polymorphic form can optimize device performance. By selecting specific polymorphs that favor either greater dielectric screening or enhanced exciton stability, materials can be tailored for particular functionalities. The improved accuracy of the DFT$-1/2$ method in capturing these electronic properties also serves as a valuable predictive tool in the design and optimization of semiconductor materials.

4.1.5 Debye parameters

The data presented in Table 4.6, reveal a clear trend in which Al-based oxides exhibit higher Debye temperatures and frequencies than their Ga- and In-based counterparts, primarily because aluminum's lower atomic mass leads to stiffer bonds and higher phonon frequencies. Within each cation set, variations among the different polymorphs can be attributed to differences in crystal structure, which affect factors such as coordination environment, bond lengths, and atomic packing. For example, the α- and δ-phases generally show comparable Debye temperatures for a given cation, reflecting similar local bonding arrangements, whereas the orthorhombic ω-phases, particularly in Al_2O_3, can reach significantly higher Debye temperatures. This increase arises from the more rigid lattice framework and stronger Al–O bonds in those structures, which elevate the vibrational frequencies. The computed values are largely consistent with the referenced experimental or theoretical ranges, with minor discrepancies that may stem

from differences in measurement conditions, sample preparation, or the computational approximations used in the phonon calculations. Overall, the results underscore the interplay between crystal structure and cation identity, where both the lighter mass of aluminum and specific structural features collectively enhance the stiffness of the lattice, thereby raising the Debye temperature and frequency.

TABLE 4.6 – Comparison of the calculated Debye temperatures (θ_D) and corresponding Debye frequencies (ω_D) for selected polymorphs. Literature reference data presented in the previous chapter are also included for comparison.

	Debye parameters		
Polymorph	θ_D (K)	θ_D Ref. (K)	ω_D (THz)
α-In_2O_3	658.24		13.72
α-Ga_2O_3	787.50		16.41
α-Al_2O_3	1025.00	1042–1100	134.21
δ-In_2O_3	685.36	420–810	14.28
δ-Ga_2O_3	779.80		16.25
δ-Al_2O_3	985.00		129.02
β-Ga_2O_3	770.91	738.00	16.06
θ-Al_2O_3	879.03		115.04
ω1-In_2O_3	646.44		13.47
ω3-Al_2O_3	1307.00		171.12
ω3-In_2O_3	650.24		13.55
ω4-Al_2O_3	912.00		119.44

Understanding the Debye temperature and frequency of these oxides is technologically significant because they provide insight into lattice stiffness, thermal conductivity, and vibrational properties, all of which are critical for high-performance materials. For instance, Al_2O_3 is widely used in electronics as a robust substrate due to its mechanical hardness and good thermal stability, properties closely linked to its high Debye temperature. Similarly, Ga_2O_3 is emerging as a promising wide-bandgap semiconductor for power electronics, where knowledge of its phonon behavior is essential for efficient heat dissipation and device reliability. In_2O_3, often employed as a transparent conducting oxide, benefits from a thorough understanding of its lattice dynamics when optimizing transparency and conductivity. These examples illustrate how the Debye temperature and frequency data guide the design and integration of oxide materials in applications ranging from power devices and optoelectronics to sensors, where thermal management and mechanical stability are key to achieving long-term performance.

5 Conclusions

Using first-principles calculations combined with phonon analysis, this study investigates the structural, electronic, optical, excitonic, and thermodynamic properties of three group IIIA sesquioxides, which are highly promising for emerging applications in electronics, power electronics, and transparent electronics. The work examines five polymorphs of indium oxide, five polymorphs of gallium oxide, and twenty-four polymorphs of aluminum oxide, revealing trends associated with both cation type and crystal structure. These results underscore the critical influence of atomic composition and structural arrangement on the fundamental properties of these materials.

The study also examines relativistic effects, particularly spin-orbit coupling (SOC), and finds that SOC minimally affects the predicted band gaps, with differences on the order of 1 meV–below the accuracy threshold of standard DFT calculations. This minor influence is due to the low atomic numbers of oxygen and the cations (In, Ga, and Al), in contrast to heavier elements where strong relativistic interactions cause significant band splitting in d- and f-orbitals. In group III sesquioxides, the band-edge states are predominantly derived from O $2p$ orbitals in the valence band and metal s orbitals in the conduction band, both experiencing weak SOC.

Calculations employing the AM05 functional yielded results that closely align with experimental data, justifying its exclusive use throughout the study and underscoring the robustness of this computational approach. Furthermore, it was demonstrated that only the combination of a d-level correction–implemented via a self-energy potential modulated by amplitude A in indium and gallium oxides using DFT+A–with the quasi-particle correction DFT$-1/2$ can accurately reproduce band gaps consistent with experimental values. For Al_2O_3, which lacks d-levels, the DFT$-1/2$ correction alone was sufficient. Notably, even for polymorphs containing up to 160 atoms, this methodology reliably provided band gap values and electron effective masses that more computationally demanding approaches, such as GW and hybrid functionals, struggle to achieve efficiently.

Through the calculation of equilibrium parameters for various polymorphs, we studied the enthalpy curves and pressure-induced phase transitions of these materials. In the case

of In_2O_3, the properties of orthorhombic polymorphs with limited literature references ($\omega 1$ and $\omega 3$) and one with no reference ($\omega 2$) were characterized. The $\omega 2$ phase appears to be a transitional state between two metastable phases that stabilize at a specific temperature. The results confirm the δ phase as the most stable form of In_2O_3, while revising the stability hierarchy of its polymorphs, with phase transitions predicted at 8 and 12 GPa for most polymorphs, except for the $\omega 2$ phase, which transitions above 22 GPa.

A similar scenario was observed for Ga_2O_3 and Al_2O_3, where the β and α phases were confirmed as the most stable forms, respectively. Phase transitions were identified between 3 and 10 GPa in Ga_2O_3 (excluding the γ polymorph) and between 50 and 150 GPa for the orthorhombic polymorphs of Al_2O_3 (excluding $\omega 1$). Negative pressure transitions were also found in other polymorphs. From a materials science perspective, particularly for Al_2O_3, these negative pressure transitions are significant for understanding tensile stress. For example, less dense phases (e.g., γ-Al_2O_3) with open spinel-like structures may become energetically favored under expansion, while the denser α-Al_2O_3 resists deformation due to its compact hexagonal lattice.

These findings underscore the interplay between tensile strain, lattice dynamics, and phase energetics. Negative pressure alters the Gibbs free energy landscape, lowering energy barriers for transitions between metastable polymorphs. This behavior is especially relevant in extreme environments, such as high-stress regions in nanostructured coatings or thermally cycled materials, where phase coexistence influences mechanical integrity. For instance, tensile-induced amorphization or transitions to transient phases (e.g., θ-Al_2O_3) may precede fracture, providing insight into failure mechanisms in ceramic composites. Controlling the phase stability of Al_2O_3 under tension can inform the design of coatings with tailored hardness, catalytic properties, or radiation resistance, and also contribute to geophysical models of mineral interactions in planetary mantles and impact scenarios. In summary, negative pressure reshapes the phase diagram of Al_2O_3 polymorphs, revealing metastable pathways and structure–property relationships under non-equilibrium conditions.

Through the computation of dielectric and optical properties, a comprehensive set of parameters was obtained, including the dielectric function, absorption coefficients, and energy loss function, thereby enhancing our understanding of light–matter interactions in these materials. Given the extensive data produced, the study focused on the excitonic properties of the oxides by employing the Wannier–Mott model to derive both the exciton binding energy (E_b) and the excitonic Bohr radius (r_B). Since the binding energy quantifies the attraction between the electron and the hole, the highest E_b observed in Al_2O_3 indicates that its excitons are more stable and less prone to dissociation, directly influencing its optical and electronic properties, such as light emission and photovoltaic efficiency. Conversely, the excitonic Bohr radius reflects the

spatial extent of the exciton; a smaller r_B suggests a more confined exciton, which can enhance quantum effects like light absorption and luminescence. The analysis revealed that In-based oxides exhibit lower excitonic parameters compared to Al-based oxides, with Ga_2O_3 polymorphs displaying intermediate values; notably, the trend for the Bohr radius is reversed, largely due to the larger effective masses of charge carriers and, to a lesser extent, variations in the dielectric constant and chemical bonding. In summary, a small r_B combined with a high E_b is ideal for light emission, whereas a larger r_B with moderate E_b is optimal for photovoltaic conversion.

Phonon calculations and density of states analysis via the quasi-harmonic approximation enabled the derivation of several thermodynamic properties and the identification of temperature-induced phase transitions not previously reported. The exceptional resilience of the most stable Al_2O_3 polymorph was demonstrated, reinforcing its suitability for extreme temperature applications, while a similar, though less pronounced, behavior was observed in Ga_2O_3. Additionally, the study identified 10 dynamically stable polymorphs of Al_2O_3, 4 of In_2O_3, and 4 of Ga_2O_3, from which fundamental Debye parameters were computed. These parameters are critical for designing materials with elevated Debye temperatures (θ_D) for thermal dissipation, optimizing low electron–phonon interaction to enhance carrier mobility, and estimating the thermal properties of minerals in the Earth's mantle or extraterrestrial environments.

The relevance of this work lies in addressing critical knowledge gaps in understanding how the properties of these oxides vary with polymorphism, providing key insights into how such variations can be leveraged in practical applications. Simultaneously, it demonstrates that the computational methodology employed is both efficient and reliable, enabling the expansion of theoretical knowledge about these materials to applications beyond the specific oxides and polymorphs investigated here.

5.0.1 Future works

Future work will focus on exploring the properties of alloys formed from these different oxides. As an initial approach, only oxides that share the same space group will be considered. Given that the stable phase of Al_2O_3 adopts a trigonal (rhombohedral)/hexagonal structure with the same space group as the α-phase of In_2O_3 ($R\bar{3}c$) and that these oxides exhibit the widest and narrowest band gaps, respectively, this system represents the most natural starting point for investigation. The wide range of possible intermediate properties between these two materials further justifies this choice, and preliminary analyses are already underway.

The second system of interest is the β-Ga_2O_3 (C2/m) – θ-Al_2O_3 (C2/m) alloy, which

offers the potential for the development of ultra-wide bandgap semiconductor alloys. In both cases, the central approach involves combining the Generalized Quasichemical Approximation (GQCA) with machine learning techniques to predict the properties of these prospective alloys.

In a subsequent phase, a similar methodology will be applied to a broader range of polymorphs among these oxides. The goal is to identify new material combinations that could address the diverse demands of semiconductor technology, enabling the development of more cost-effective devices with tailored properties.

Appendix A - DFT and phonons

In order to avoid overburdening the main text, the proofs and other demonstrations regarding the density functional theory are demonstrated here.

A.0.1 Proofs of the Hohenberg and Kohn theorems

The first theorem states that:

i) The external potential $V(\vec{r})$ felt by the electrons is a unique functional of the electron density $n(\vec{r})$, apart from a trivial additive constant.

Here, we are assuming that the change between two potentials $v(\vec{r})$ and $v(\vec{r}\,')$ is consistently identical due to the comparable electron density of the ground state throughout the crystal, i.e.

$$v(\vec{r}\,') - v(\vec{r}) = \text{constant} \tag{A.1}$$

and the Hamiltonian operator $\hat{H}$ of the system is given by:

$$\hat{H} = \hat{T} + \hat{U} + \hat{V}_{\text{ext}}, \tag{A.2}$$

where $\hat{T}$ is the total kinetic energy of electrons,

$$\hat{T} = \frac{1}{2}\int \nabla\psi^*(\vec{r})\,\nabla\psi(\vec{r})\,d(\vec{r}), \tag{A.3a}$$

$\hat{U}$ is the Coulomb (repulsive) interaction,

$$\hat{U} = \frac{1}{2}\int \frac{1}{|\vec{r}-\vec{r}\,'|}\psi^*(\vec{r})\psi(\vec{r}\,')\,\psi(\vec{r}\,')\psi(\vec{r})\,d(\vec{r}), \tag{A.3b}$$

$\hat{V}_{ext}$ is the external potential,

$$\hat{V}_{ext} = \int v(\vec{r})\psi^*(\vec{r})\psi(\vec{r})d\vec{r}, \tag{A.3c}$$

and where it is assumed that the ground state is non-degenerate, and the electron density in this state is given by:

$$n(\vec{r}) = \int \Psi^*(\vec{r})\Psi(\vec{r})d\vec{r}. \tag{A.4}$$

The proof of this theorem can be illustrated through *reductio ad absurdum* as follows: The solution of Hamiltonian in Eq. (A.2) for a system containing N interacting particles and where $\psi(r_1, r_2, ..., r_N)$ is a ground state wave-function is:

$$\hat{H}\psi(r_1, r_2, ..., r_N) = E\psi(r_1, r_2, ..., r_N) \tag{A.5}$$

Consider an additional potential, denoted as $v'(\vec{r})$, leading to a modified Hamiltonian denoted as $\hat{H}'$ and a corresponding ground state wave-function ψ' and energy E'. It is a requirement that the ground state density, $n(\vec{r})$, remains unchanged in both scenarios and the Hamiltonian for this many-body system can be expressed as:

$$\hat{H}'\psi' = E'\psi'. \tag{A.6}$$

and

$$\hat{H}\,' = \hat{T} + \hat{U} + \hat{V}'_{\text{ext}} \tag{A.7}$$

In Eq. (A.1), for ψ to be distinct from $\psi\,'$, the result must not be a constant. Consequently, the wave functions must satisfy different Schrödinger equations. According to the variational principle, the energy of the ground state attains its minimum when employing the exact wave function associated with that state. Note that $E = \langle\psi|\,\hat{H}\,|\psi\rangle$, then:

$$E = \langle\psi|\,\hat{H}\,|\psi\rangle < \left\langle\psi'\right|\hat{H}\left|\psi'\right\rangle, \tag{A.8}$$

which yields to

$$E < E' + \int \left[v(\vec{r}) - v'(\vec{r})\right] n(\vec{r})d\vec{r}. \tag{A.9}$$

Swapping the labels leads to

$$E' < E + \int \left[v'(\vec{r}) - v(\vec{r})\right] n(\vec{r})d\vec{r}. \tag{A.10}$$

Now, adding Eq. (A.9) and Eq. (A.10) we get

$$E' + E < E + E'. \tag{A.11}$$

and consequenltly

$$0 < 0 \tag{A.12}$$

which is a clear inconsistency and confirms that different potentials provide different

densities. Since the complete ground state energy is a functional of the ground state electron density so must be its individual components and we can rewrite Eq. (A.2) as:

$$E[n(\vec{r})] = \hat{T}[n(\vec{r})] + \hat{U}[n(\vec{r})] + \hat{V}_{\text{ext}}[n(\vec{r})] \tag{A.13}$$

The second theorem is enunciated as:

ii) The density that minimises the total energy is the exact groundstate density.

The concept emphasizes a universal functional $F[n(\vec{r})]$, which determines the ground-state energy, achieving the lowest value when the density matches the true ground-state density. This enables using the variational principle to computationally solve for the ground-state density by minimizing the energy.

Considering the functional $F[n(\vec{r})]$, the ground-state density $n(\vec{r})$, and an alternate density $n'(\vec{r})$ – related to other state of a system – the second theorem states:

$$F[n(\vec{r})] = \hat{T}[n(\vec{r})] + \hat{U}[n(\vec{r})] \tag{A.14}$$

and the energy functional for a given potential $v(\vec{r})$

$$E_v[n(\vec{r})] = \int [v(\vec{r})n(\vec{r})]d\vec{r} + F[n(\vec{r})], \tag{A.15}$$

where

$$F[n(\vec{r})] \equiv \langle\psi|\, \hat{T} + \hat{U}\, |\psi\rangle \tag{A.16}$$

is referred to as universal functional. $E_v[n(\vec{r})]$ is equals to the ground state energy E if $n(\vec{r})$ is the exact density and

$$N = \int n(\vec{r})d\vec{r} \equiv N[n(\vec{r})], \tag{A.17}$$

where N is the number of particles. If ψ' is the ground state associated with the external potential $v'(r)$, the relation in Eq. A.16 is valid. From the variational method, the functional E_v of the wave function Ψ' for a system of N particles given by

$$E_v[\Psi'] \equiv \langle\Psi|'\, \hat{V}\, |\Psi'\rangle + \langle\Psi|'\, \hat{T} + \hat{U}\, |\Psi'\rangle\,, \tag{A.18}$$

is minimum for the ground state Ψ, relative to variations of Ψ' and a constant number of particles N. If Ψ' represents the ground state associated with a different external potential $v'(\vec{r})$, then, using Eq. A.18 and A.16, the following relationship is valid:

$$\int v(\vec{r})n'(\vec{r})d\vec{r} + F[n'(\vec{r})] > \int v(\vec{r})n(\vec{r})d\vec{r} + F[n(\vec{r})] \;\therefore \tag{A.19}$$

$$E_v[\Psi'] > E_v[\Psi] \tag{A.20}$$

and

$$E_v[n'(\vec{r})] > E_v[n(\vec{r})] \tag{A.21}$$

By knowing $F[n(\vec{r})]$, the ground-state density and energy under a specific external potential can be obtained by minimizing $E_v[n(\vec{r})]$. To address the long-range behavior of Coulomb interactions, a functional $G[n(\vec{r})]$ is introduced, encompassing the kinetic and exchange-correlation energies as:

$$F[n(\vec{r})] = \frac{1}{2}\int \frac{n(\vec{r})n'\vec{r}}{|\vec{r}-\vec{r'}|}d\vec{r}d\vec{r'} + G[n(\vec{r})] \tag{A.22}$$

This relation holds under the Born-Oppenheimer approximation, which assumes that nuclei (such as atoms) move much more slowly than electrons due to their significantly larger masses. Consequently, the positions of the nuclei are treated as fixed while the electrons move rapidly around them.

Despite the Born-Oppenheimer approximation, the theoretical framework remains precise up to this point, yet an analytical form for the $G[n(\vec{r})]$ functional is still unknown. To determine the ground-state electronic density, approximations must be introduced. In other words, while the theorems established by Hohenberg and Kohn are exact, they are difficult to apply in practical calculations (BURKE; WAGNER,). Our primary goal thus far has been to illustrate that a system can be effectively described by its electron density. The focus is not on exhaustive details but on providing a practical method to determine the density that characterizes the system. Practically, this is achieved through the Kohn-Sham equations.

A.0.2 Details of the Kohn-Sham equations

The mathematical form of the Kohn-Sham is as the following:

$$\hat{H}_{\mathrm{KS}}\psi_i(\vec{r}) = \left(-\frac{1}{2}\nabla^2 + v_{\mathrm{KS}}[n(\vec{r})]\right)\psi_i(\vec{r}) = \varepsilon_i\psi_i(\vec{r}), \tag{A.23a}$$

where v_{KS} is the effective potential, the functions $\psi_i(\vec{r})$ are the eigenfunctions of the Kohn-Sham equation, $\hat{H}_{KS}$ is the Kohn-Sham Hamiltonian, and v_{KS} is the Kohn-Sham effective external potential given by:

$$v_{\mathrm{KS}} = \frac{1}{2}\int \frac{n(\vec{r})n'\vec{r}}{|\vec{r}-\vec{r'}|}d\vec{r} + v_{\mathrm{xc}}[n(\vec{r})] \tag{A.23b}$$

In

$$\hat{H}_{\mathrm{KS}} = -\frac{1}{2}\nabla^2 + v_{\mathrm{ext}}(\vec{r}) + v_{\mathrm{H}}(\vec{r}) + v_{\mathrm{xc}}[n(\vec{r})], \tag{A.24}$$

the term $v_{\mathrm{xc}}(\vec{r})$ corrects the assumption of non-interacting electrons in the Kohn-Sham system. For interacting electrons, the density $n(\vec{r})$ is insufficient to fully describe the system's energy. $v_{\mathrm{xc}}(\vec{r})$, derived from the exchange-correlation energy functional $E_{\mathrm{xc}}[n]$, incorporates exchange (quantum symmetry) and correlation (spatial distribution) effects, refining the total energy as:

$$v_{\mathrm{xc}}(\vec{r}) = \frac{\delta E_{\mathrm{xc}}[n]}{\delta n(\vec{r})} \tag{A.25}$$

KS orbitals ψ_i and eigenvalues ε_i do not correspond to the wave functions or energies of the interacting system. Only the ground-state density $n(\vec{r})$ matches between real and fictitious systems. As v_{KS} depends on $n(\vec{r})$, the KS equation requires a self-consistent calculation, making it computationally viable.

A.0.3 Plane-wave basis

The Kohn-Sham orbitals can be given as a sum of periodic functions of the form of plane waves as:

$$\phi_{\vec{G}}(\vec{r}) = e^{i\vec{G}\cdot\vec{r}}, \tag{A.26}$$

where $\vec{G}$ is the reciprocal lattice vector and $\vec{r}$, as usual, is the position in real space. These functions $\phi_{\vec{G}}(\vec{r})$ form an orthonormal basis, allowing the expansion of a wave function $\psi_i(\vec{r})$ as a sum of plane waves such as:

$$\psi_i(\vec{r}) = \sum_{\vec{G}} c_{i,\vec{G}} e^{i\vec{G}\cdot\vec{r}}, \tag{A.27}$$

where $c_{i,\vec{G}}$ are the expansion coefficients that need to be determined.

Note that the Fourier transform of a function $f(\vec{r})$ from real space to reciprocal space is given by:

$$\tilde{f}(\vec{G}) = \int f(\vec{r}) e^{-i\vec{G}\cdot\vec{r}} d\vec{r} \tag{A.28}$$

and its inverse from reciprocal space to real space is:

$$f(\vec{r}) = \sum_{\vec{G}} \tilde{f}(\vec{G}) e^{i\vec{G}\cdot\vec{r}} \tag{A.29}$$

The parameters $f(\vec{r})$ and $\tilde{f}(\vec{G})$ correspond to the real-space function and its Fourier coefficients, respectively. Eq.A.29 mirrors Eq.A.27, enabling the determination of $c_{i,\vec{G}}$ via inverse Fourier transforms of ψ_i. This method is ideal for periodic systems, as plane waves naturally satisfy lattice periodicity and provide a universal basis. While $n(\vec{r})$,

v_{KS}, and other terms are evaluated in real space, reciprocal space simplifies intermediate calculations, facilitated by Fourier transforms.

In practice, the summation over $\vec{G}$ is finite, constrained by a maximum kinetic energy for plane waves, i.e.:

$$\frac{1}{2}\hbar^2|\vec{G}|^2 \leq E_{\mathrm{cut}}, \tag{A.30}$$

where E_{cut} (cutoff parameter) controls the number of plane waves and the calculation's accuracy.

Similarly, the convolution integral of the Coulomb interaction between electrons, the Hartree potential $v_{\mathrm{H}}(\vec{r})$, implicit in Eq. A.24, is given by:

$$v_H(\vec{r}) = \frac{1}{2}\int \frac{n(\vec{r})n'(\vec{r})}{|\vec{r}-\vec{r}'|}d\vec{r}, \tag{A.31}$$

it is difficult to solve in real space. However, by using the Fourier Transform, we have:

$$v_H(\vec{G}) = \frac{\tilde{n}(\vec{G})}{|\vec{G}|^2}, \tag{A.32}$$

where $\tilde{n}(\vec{G})$ is the charge density in reciprocal space, which is computationally more efficient to calculate.

Finally, using the wave functions $\psi_i(\vec{r})$ in Eq. A.27, the electronic density is recalculated as:

$$n(\vec{r}) = \sum_i f_i|\psi_i(\vec{r})|^2, \tag{A.33}$$

where f_i are the orbital occupations, determined by the Fermi-Dirac distribution.

The new density $n(\vec{r})$ is used to recalculate v_{KS} until self-consistency is achieved, at which point the final density is employed to calculate total energy, forces, stresses, and other properties.

A.0.4 Bloch's theorem

Consider a Hamiltonian $\hat{H}$ with a periodic potential,

$$\hat{H} = -\frac{\hbar^2}{2m}\nabla^2 + \hat{V}(\vec{r}) \tag{A.34}$$

where $\hat{V}(\vec{r}) = \hat{V}(\vec{r}+\vec{R})$ for any lattice vector $\vec{R}$. Since the Hamiltonian commutes with the translation operator $T_{\vec{R}}$, whose action is defined by

$$T_{\vec{R}}\psi(\vec{r}) = e^{i\vec{k}\cdot\vec{R}}\psi(\vec{r}), \tag{A.35}$$

where $\vec{r}$ is a vector in the reciprocal space. This result implies that the wavefunction can be expressed in the form

$$\psi_{n\vec{k}}(\vec{r}) = e^{i\vec{k}\cdot\vec{r}} u_{n\vec{k}}(\vec{r}), \tag{A.36}$$

with $u_{n\vec{k}}(\vec{r})$ being a function that inherits the periodicity of the lattice, i.e.,

$$u_{n\vec{k}}(\vec{r}+\vec{R}) = u_{n\vec{k}}(\vec{r}) \tag{A.37}$$

which directly links to the efficiency of the plane-wave basis in DFT by leveraging the inherent periodicity of the crystal lattice.

A.0.5 Phonons

Consider ω as the phonon frequency, $\mathbf{q}$ as the wavevector, and s denoting the phonon branch. Specifically, the phonon contribution to the internal energy U of a system is given by:

$$U = \sum_{\mathbf{q},s} \hbar\omega(\mathbf{q},s) \left(n_{\mathbf{q},s} + \frac{1}{2} \right), \tag{A.38}$$

where $n_{\mathbf{q},s}$ is the Bose-Einstein distribution function:

$$n_{\mathbf{q},s} = \frac{1}{e^{\hbar\omega(\mathbf{q},s)/k_B T} - 1} \tag{A.39}$$

with k_B denoting the Boltzmann constant and T the temperature in Kelvin. Note that this expression includes the zero-point energy term $\frac{1}{2}\hbar\omega(\mathbf{q},s)$, which accounts for quantum fluctuations.

Also, the Helmholtz free energy F is given by:

$$F = k_B T \sum_{\mathbf{q},s} \ln\left(1 - e^{-\hbar\omega(\mathbf{q},s)/k_B T}\right) \tag{A.40}$$

Similarly, the entropy S due to phonons is given by:

$$S = -\sum_{\mathbf{q},s} k_B \left[n_{\mathbf{q},s} \ln n_{\mathbf{q},s} - \left(1 + n_{\mathbf{q},s}\right) \ln\left(1 + n_{\mathbf{q},s}\right) \right]. \tag{A.41}$$

Moreover, the phonon heat capacity at constant volume, C_V, is obtained by differentiating the internal energy:

$$C_V = \left(\frac{\partial U}{\partial T} \right)_V = k_B \sum_{\mathbf{q},s} \left[\frac{\hbar\omega(\mathbf{q},s)}{k_B T} \right]^2 \frac{e^{\hbar\omega(\mathbf{q},s)/k_B T}}{\left(e^{\hbar\omega(\mathbf{q},s)/k_B T} - 1\right)^2} \tag{A.42}$$

Using the phonon density of states (DOS) given by

$$D(\omega) = \frac{1}{\hbar} \sum_{j,q} \delta \left[\omega - \omega_j(\mathbf{q}) \right], \tag{A.43}$$

the thermodynamic functions derived from $\omega(\mathbf{q}, s)$ can be expressed not only in terms of volume (V) but also as functions of temperature (T). Within the Born-Oppenheimer approximation, the Helmholtz free energy, $F(V,T)$, can be separated into an electronic term, $F^{\mathrm{el}}(V,T)$, and a vibrational term, $F^{\mathrm{vib}}(V,T)$, which originates from atomic vibrations:

$$F(V,T) = F^{\mathrm{el}}(V,T) + F^{\mathrm{vib}}(V,T) \tag{A.44}$$

For insulating materials such as Al_2O_3 polymorphs, electronic excitations and entropy contributions are insignificant at moderate temperatures. Under these conditions, the electronic free energy is well approximated by:

$$F^{\mathrm{el}}(V,T) \approx E_0(V_0), \tag{A.45}$$

where $E_0(V_0)$ corresponds to the total energy, typically determined by equations of state (EOS).

By using the quasi-harmonic approximation, the vibrational contribution to the free energy is given by:

$$F^{\mathrm{vib}}(V,T) = k_B T \int_0^\infty d(\hbar\omega) \ln \left[2 \sinh \left(\frac{\hbar\omega}{2k_B T} \right) \right] D(\omega). \tag{A.46}$$

In this approach, the phonon density of states (DOS) $D(\omega)$ depends on the volume V, as it is related to the Brillouin zone volume, which varies as $(2\pi)^3/V$.

The free energy

$$F^{\mathrm{vib}}(V,T) = U^{\mathrm{vib}}(V,T) - TS^{\mathrm{vib}}(V,T) \tag{A.47}$$

combines the internal energy, including the zero point energy (ZPE)

$$U^{\mathrm{vib}}(V,T) = F^{\mathrm{vib}} - T \left(\frac{\partial F^{\mathrm{vib}}}{\partial T} \right)_V = \frac{1}{2} \int_0^\infty d\hbar\omega \coth \left(\frac{\hbar\omega}{2k_B T} \right) D(\omega) \tag{A.48}$$

and the entropy of the vibrating lattice

$$S^{\mathrm{vib}}(V,T) = -\left(\frac{\partial F}{\partial T} \right)_V^{\mathrm{vib}}, \tag{A.49}$$

i.e.,

$$S^{\text{vib}}(V,T) = k_B \int_0^\infty d\hbar\omega \left\{ \frac{\hbar\omega}{2k_BT}\coth\left(\frac{\hbar\omega}{2k_BT}\right) - \ln\left[2\sinh\left(\frac{\hbar\omega}{2k_BT}\right)\right]\right\} D(\omega) \quad \text{(A.50)}$$

The internal energy allows the direct calculation of the heat capacity at constant volume as

$$C_V = \left(\frac{\partial U^{\text{vib}}}{\partial T}\right)_V = k_B \int_0^\infty d\hbar\omega \left(\frac{\hbar\omega}{2k_BT}\right)\left[\sinh^2\left(\frac{\hbar\omega}{2k_BT}\right)\right]^{-1} D(\omega) \quad \text{(A.51)}$$

Finally, in the low-temperature limit ($T \to 0$), the energies F^{vib} and U^{vib} are dominated by the ZPE and are given by:

$$\lim_{T\to 0} F^{\text{vib}} = \lim_{T\to 0} U^{\text{vib}} = \frac{1}{2}\int_0^\infty \hbar\omega D(\omega) d(\hbar\omega) \quad \text{(A.52)}$$

Additionally, by analyzing the limits of the heat capacity C_V, one can establish a connection between these thermal properties and the structural characteristics of a given polymorph. In the high-temperature limit, the Dulong-Petit law is established, leading to a constant C_V, i.e., it tends to stabilize. In this regime, C_V is given by:

$$C_V = k_B \int_0^\infty D(\omega) d(\hbar\omega) \quad \text{(A.53)}$$

Integrating the DOS $D(\omega)$ yields $3N_{\text{atom}p}N_p$. Here, $3N_{\text{atom}p}$ accounts for the total number of vibrational modes in a primitive unit cell of polymorph p (given that each atom contributes three degrees of freedom), and N_p is the number of these unit cells in the sample. Since each unit cell occupies a volume Ω_p, the product $N_p\Omega_p$ represents the total volume of the system. This total volume is a crucial parameter because it connects the microscopic structural details (i.e., the arrangement and number of atoms within each cell) to the macroscopic thermodynamic properties. In particular, it allows us to normalize the molar heat capacity per formula unit, ensuring that comparisons across different polymorphs or samples accurately reflect differences in both structure and size.

To express this quantity per formula unit, the product $3N_{\text{atom}p}N_p$ is replaced by $5n_L$, where 5 represents the number of atoms in the sesquioxides. In this context, n_L is the Loschmidt number, defined as $n_L = N_A/V_m$, with V_m representing the molar volume and v the volume occupied by a single molecule. This definition creates a bridge between a microscopic parameter (the volume of a molecule) and a macroscopic property. Moreover, considering that $V_m/v = N_A$ where N_A is Avogadro's number, and recognizing that $N_Ak_B = R$, with k_B being Boltzmann's constant and R the universal gas constant, it follows that $n_Lk_B = R$. Thus, substituting with $5n_L$ normalizes the

vibrational mode count per formula unit, integrating atomic-scale details with the system's macroscopic thermodynamic properties.

In the high-temperature limit, the normalized molar heat capacity converges to the classical Dulong-Petit value, i.e., the Dulong-Petit law (BÖTTGER, 1983; ASHCROFT; MERMIN, 1976) as

$$\lim_{T\to\infty} C_V(T) = 15R \tag{A.54}$$

At low temperatures, the thermal population of vibrational modes is restricted to the acoustic branches, as higher-energy optical modes remain largely unoccupied. Within the framework of the Debye model (BÖTTGER, 1983; ASHCROFT; MERMIN, 1976), these acoustic branches can be approximated by a linear dispersion relation, assuming an isotropic medium where the phonon frequency $\omega_j(\mathbf{q})$ varies proportionally with the magnitude of the wave vector, $q = |\mathbf{q}|$. This relationship is expressed as $\hbar\omega_j(\mathbf{q}) = \hbar\bar{v}q$, where $\bar{v}$ represents the averaged sound velocity of the material. To facilitate the integration over the BZ in reciprocal space, its intricate geometry is replaced by a sphere of equal volume, enabling a more manageable analytical treatment of vibrational properties. This approach leads to the following expression:

$$U^{\text{vib}} = \frac{\pi^2}{10}\frac{N_p\Omega_p}{(\hbar\bar{v})^3}(k_BT)^4, \tag{A.55}$$

where the radius of the sphere, q_{BZ} is defined by the cell volume Ω_p as

$$\Omega_p = \frac{(2\pi)^3}{\frac{4\pi}{3}q_{\text{BZ}}^3} = \frac{6\pi^2}{q_{\text{BZ}}^3} \tag{A.56}$$

This quantity gives the Debye frequency

$$\omega_D = \bar{v}q_{\text{BZ}} \tag{A.57}$$

and the Debye temperature

$$\theta_D = \frac{\hbar\omega_D}{k_B} = \frac{\hbar\bar{v}q_{\text{BZ}}}{k_B}, \tag{A.58}$$

resulting in an internal energy

$$U^{\text{vib}} = \frac{3\pi^4}{5}N_p\left(\frac{T}{\theta_D}\right)^3 k_BT \tag{A.59}$$

This leads to the Debye law, with a heat capacity C_V given by

$$C_V = \frac{12\pi^4}{5}N_p\left(\frac{T}{\theta_D}\right)^3 k_B \tag{A.60}$$

and a corresponding molar heat capacity, normalized to a formula unit

$$C_V(T) = \frac{12\pi^4}{N_{\mathrm{atom}p}} R \left(\frac{T}{\theta_D}\right)^3 \tag{A.61}$$

which depends on the polymorph p via the number of atoms $N_{\mathrm{atom}p}$ and the Debye frequency θ_D. Both quantities define a prefactor α of the T^3 -law, which varies depending on the polymorph. This prefactor is proportional to

$$\frac{1}{N_{\mathrm{atom}p}\theta_D^3} \approx \frac{\Omega_p}{N_{\mathrm{atom}p}} \tag{A.62}$$

representing the volume per formula unit. Consequently, the Debye law is recovered as

$$C_V(T) = \alpha T^3, \tag{A.63}$$

where slight variations in α enable the estimation of the Debye temperature or frequency within the range $T = 0$–100 K.

This connection between phonon dynamics and thermodynamic properties provides a framework for analyzing different polymorphs of oxides as a function of temperature, offering deeper insight into their thermal behavior.

Appendix B - Technical informations about methodology

This appendix provides detailed technical information about the methodology employed in this thesis.

B.1 k-point meshes

Tables B.1, B.2, and B.3 presents **k**-point sampling of the Brillouin zone (BZ) meshes for different oxides and polymorphs used in Self-Consistent (SC) and non-Self-Consistent (nSC) calculations.

TABLE B.1 – **k**-points sampling utilized for In_2O_3 polymorphs calculations.

In_2O_3 polymorph	Crystal structure	Name / denotation	Space group	**k**-points SC	**k**-points nSC
α-In_2O_3	Trigonal/rhombohedral	Corundum	$R\bar{3}c$	5 5 5	10 10 10
α-In_2O_3 (np)	Hexagonal	Corundum	$R\bar{3}c$	4 4 1	8 8 2
δ-In_2O_3	Cubic	Bixbyite	$Ia\bar{3}$	5 5 5	10 10 10
ω1-In_2O_3	Orthorhombic	-	Pbcn	5 5 5	10 10 10
ω2-In_2O_3	Orthorhombic	-	Pnma	5 5 5	10 10 10
ω3-In_2O_3	Orthorhombic	-	Pbca	5 5 5	10 10 10

TABLE B.2 – **k**-points sampling utilized for Ga_2O_3 polymorphs calculations.

Ga_2O_3 polymorph	Crystal structure	Name / denotation	Space group	**k**-points SC	**k**-points nSC
α-Ga_2O_3	Trigonal/rhombohedrall	Corundum	$R\bar{3}c$	5 5 5	10 10 10
α-Ga_2O_3 (np)	Hexagonal	Corundum	$R\bar{3}c$	4 4 1	8 8 2
β-Ga_2O_3	Monoclinic	-	C2/m	5 5 5	10 10 10
β-Ga_2O_3 (np)	Monoclinic	-	C2/m	2 8 4	4 16 8
γ-Ga_2O_3	Cubic	Defective spinel	$Fd\bar{3}m$	5 5 5	10 10 10
δ-Ga_2O_3	Cubic	Bixbyite	$Ia\bar{3}$	5 5 5	10 10 10
κ-Ga_2O_3	Orthorhombic	-	$Pna2_1$	5 5 5	10 10 10

TABLE B.3 – **k**-points sampling utilized for Al_2O_3 polymorphs calculations.

Al_2O_3 polymorph	Crystal structure	Name / denotation	Space group	**k**-points SC	**k**-points nSC
α-Al_2O_3	Trigonal/rhombohedrall	Corundum	$R\bar{3}c$	5 5 5	10 10 10
α-Al_2O_3 (np)	Hexagonal	Corundum	$R\bar{3}c$	4 4 1	8 8 2
γ'-Al_2O_3	Triclinic	-	P1	3 5 2	6 10 4
θ-Al_2O_3	Monoclinic	β	C2/m	5 5 5	10 10 10
θ-Al_2O_3 (np)	Monoclinic	β	C2/m	2 8 4	4 16 8
θ2-Al_2O_3	Monoclinic	β	C2/m	5 5 5	10 10 10
θ2-Al_2O_3 (np)	Monoclinic	β	C2/m	5 5 3	10 10 6
ω1-Al_2O_3	Orthorhombic	-	$Cmc2_1$	4 4 5	8 8 10
ω2-Al_2O_3	Orthorhombic	-	Pnnm	8 5 2	16 10 4
ω3-Al_2O_3	Orthorhombic	Rh_2O_3(II)	Pbcn	5 5 3	10 10 6
ω4-Al_2O_3	Orthorhombic	-	Pbca	5 4 1	10 8 2
α'-Al_2O_3	Trigonal/rhombohedrall	Corundum	$R\bar{3}c$	5 5 5	10 10 10
α'-Al_2O_3 (np)	Hexagonal	Corundum	$R\bar{3}c$	4 4 1	8 8 2
δ-Al_2O_3	Cubic	-	$Ia\bar{3}d$	5 5 5	10 10 10

B.2 CUT and amplitude values

Table B.4 present specific values of amplitude (A) and CUT values obtained for corrections of the d-levels in In_2O_3 and G_2O_3 and CUT values applied to O $2p$ levels for the energy band gap quasiparticle correction. Table B.5 presents the values of CUT applied to O $2p$ levels for the band gap correction in Al_2O_3.

TABLE B.4 – Amplitude and CUT applied to In $4d$ (Ga $3d$ levels) for DFT+A calculations and CUT applied to O $2p$ for DFT$-1/2$ calculations.

	DFT+A		DFT-1/2		DFT+A		DFT-1/2
Polymorph	Amplitude	CUT	CUT	Polymorph	Amplitude	CUT	CUT
α-In_2O_3	1.4	2.10	2.49	α-Ga_2O_3	3.2	1.23	2.39
δ-In_2O_3	1.4	2.10	2.48	β-Ga_2O_3	3.2	1.23	2.42
ω1-In_2O_3	1.4	2.10	2.49	γ-Ga_2O_3	3.2	1.23	2.42
ω2-In_2O_3	1.2	2.10	2.51	δ-Ga_2O_3	3.2	1.23	2.40
ω3-In_2O_3	1.4	2.10	2.49	κ-Ga_2O_3	3.2	1.23	2.42

TABLE B.5 – CUT values applied to O $2p$ for DFT$-1/2$ calculations of Al_2O_3 polymorphs.

Polymorph	Space group	CUT
γ'-Al_2O_3	P1	2.35
θ-Al_2O_3	C2/m	2.38
$\theta 2$-Al_2O_3	C2/c	2.43
$\omega 1$-Al_2O_3	$Cmc2_1$	2.46
$\omega 2$-Al_2O_3	Pnnm	2.47
$\omega 3$-Al_2O_3	Pbcn	2.33
$\omega 4$-Al_2O_3	Pbca	2.33
α'-Al_2O_3	$R\bar{3}$	2.34
α-Al_2O_3	$R\bar{3}c$	2.32
δ-Al_2O_3	$Ia\bar{3}$	2.35

B.3 Derivation of the expression for $H(p)$

The expression of enthalpy as function of the pressure $H = H(p)$ was obtained by considering

$$H(p) = E(V) + pV, \tag{B.1}$$

where $E(V)$ is the energy as function of volume V and p is the pressure as usual. Considering the quadratic expansion with respect to equilibrium as

$$E \approx E_0 + \left(\frac{\partial E}{\partial V}\frac{\partial V}{\partial p}\right)_{=0} p \tag{B.2}$$

and from

$$p = -\frac{\partial E}{\partial V} \;\; \therefore \;\; \frac{\partial E}{\partial V} = -p, \tag{B.3}$$

and

$$B = -V\frac{\partial p}{\partial V} \;\; \therefore \;\; -\frac{V}{B} = \frac{\partial V}{\partial p} \tag{B.4}$$

in Eq (B.2), one can obtain

$$E \approx E_0 + \frac{V_0}{B_0}p^2, \tag{B.5}$$

also considering that

$$pV \approx pV_0. \tag{B.6}$$

Now, appying Eq (B.5) in Eq (B.1) it is easy to see that

$$H(p) = E_0 + pV_0\left(1 + \frac{p}{B_0}\right). \tag{B.7}$$

Appendix C - Application of DFT+$A-1/2$ methodology

This appendix provides an bird's eye view about the practical application of the method DFT+$A-1/2$.

C.1 Sequencial procedures

For the calculation of properties of a given polymorph, the following steps be prompted:

i) Standard DFT calculation;

ii) Generate the amplitude-modulated potentials and perform standard DFT calculations for each new potentials;

iii) Analyse the relative position of the level of interest for calculation using the averaging procedure of finding the position of the level as demonstrated in Chap. 2, section 2.3.1;

iv) Choice of the potential which provides the desired position of the level relative with the Fermi level set at zero;

v) It is recomended to choose a level position below the desired position (usually from the experimental results) due the tendency of increasing the binding energy of the level after the application of the DFT-1/2 correction on the VBM;

vii) With the level positioned proceed the analysis of the band character and perform the DFT-1/2 procedures as usual;

viii) Analyse and evaluate if the level positioned in the desired point (energy). In negative, back to the step iv).

A schematic representation of the steps envolved in a DFT+$A-1/2$ is given in the Fig. F.1.

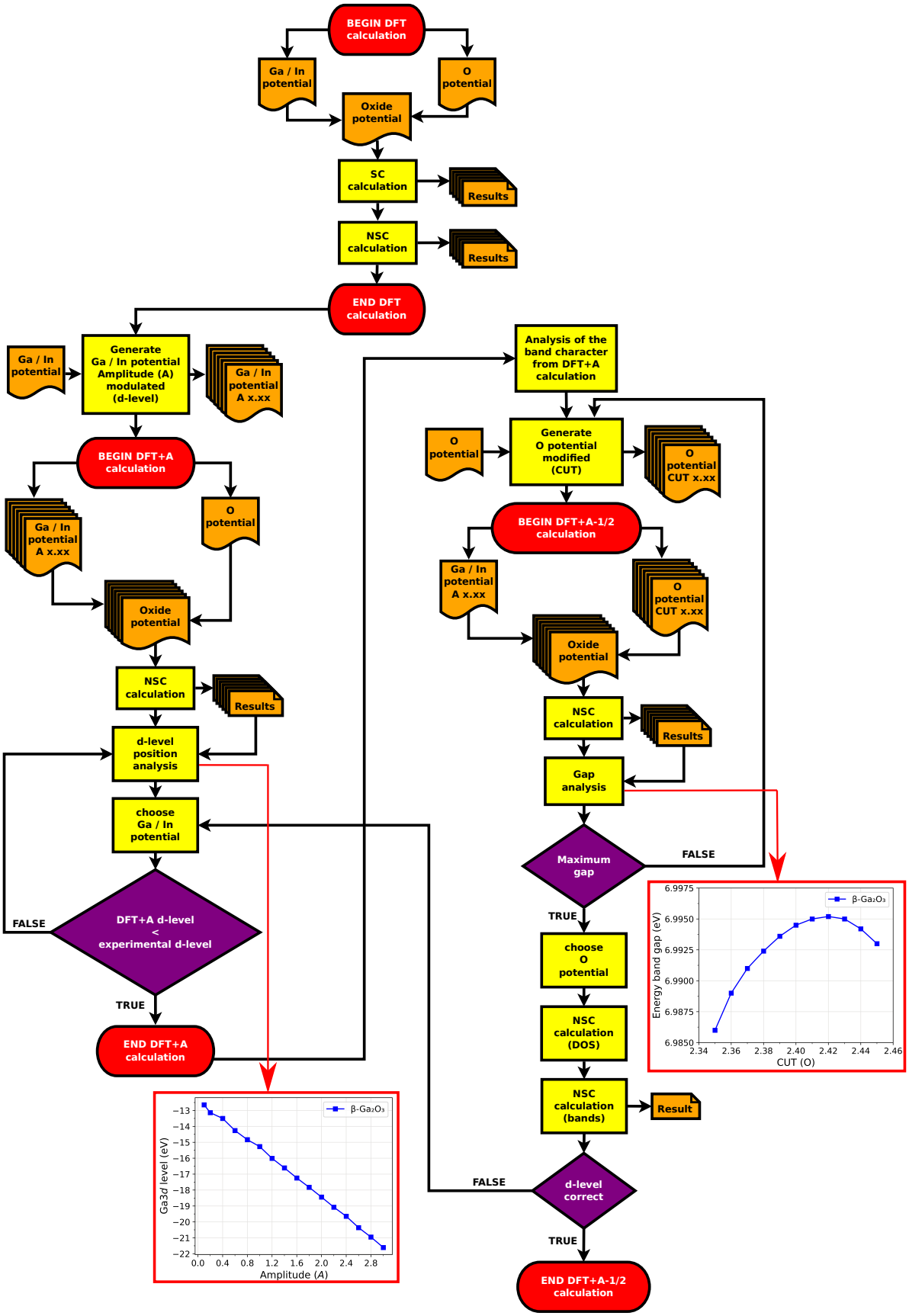

FIGURE C.1 – Schematic representation of a complete cycle of calculations.

Appendix D - Supplementary informations of In_2O_3 polymorphs

This appendix provides supplemenatary informations about the results obtained for the In_2O_3 polymorphs.

D.1 Density of states

Figure F.1 shows the position of the d level before and after the DFT+A correction, where the DOS peak associated with the d level is adjusted to a final position based on experimental data. The application of this method demonstrates how the shallow d level (closer to the VBM) affects the band gap, reducing it in such a way that quasiparticle correction alone is insufficient to provide accurate results for the electronic structure of this material.

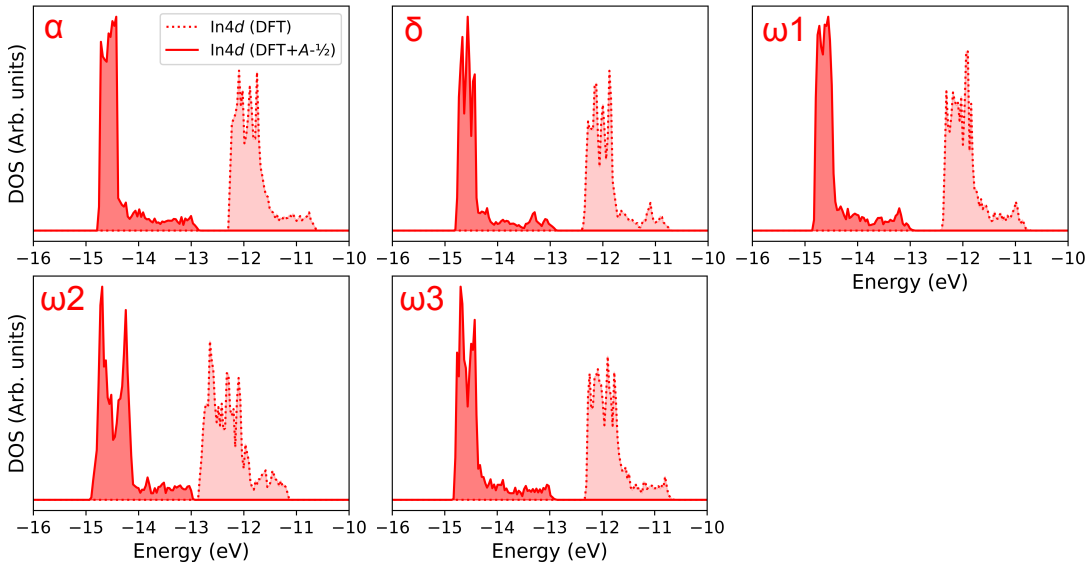

FIGURE D.1 – Density of states of the In 4d level calculated using standard DFT (light red, dashed line) and after the DFT+$A-1/2$ correction. The labels for each polymorph are indicated in red in each panel.

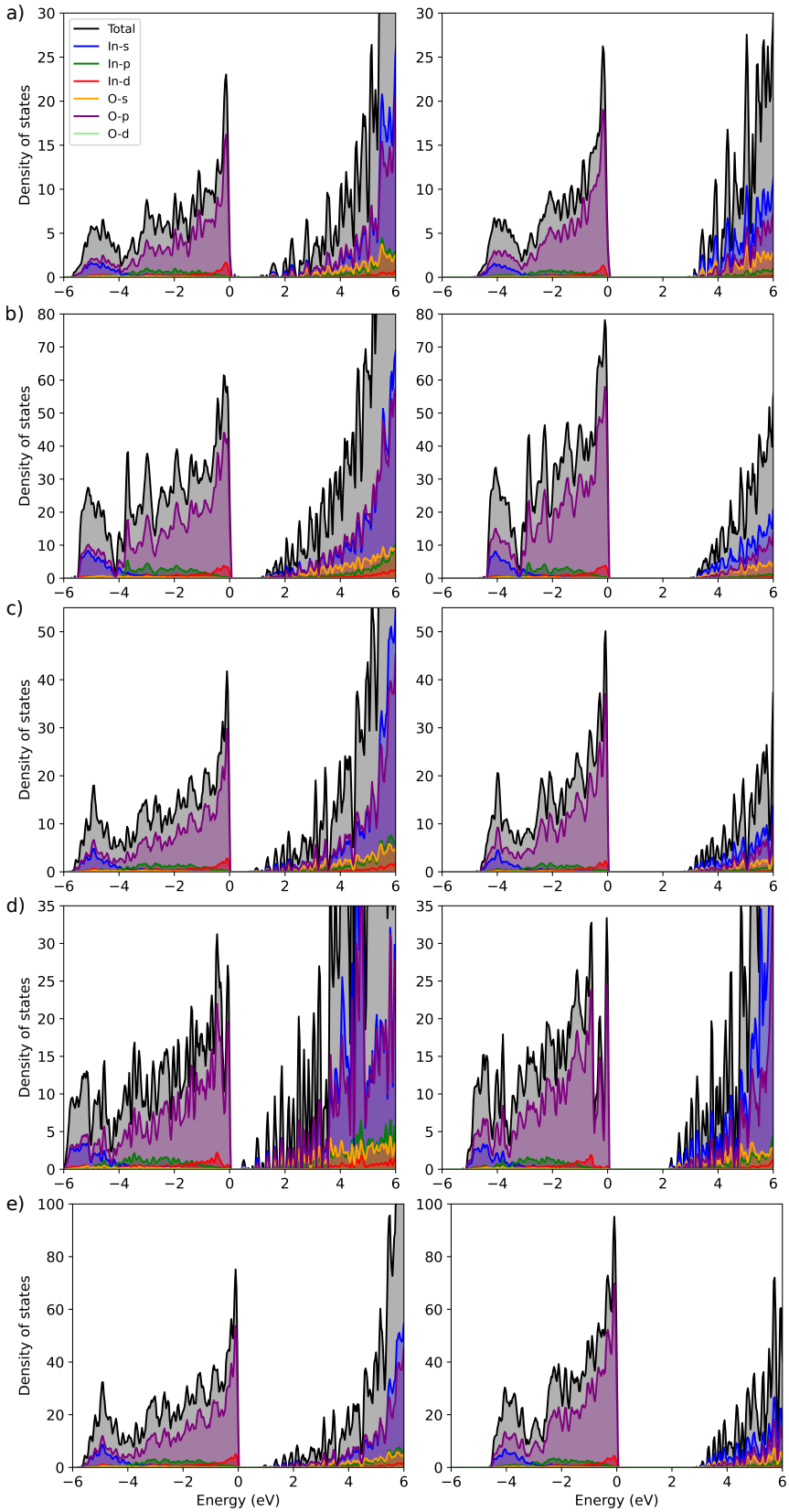

FIGURE D.2 – Density of states near the gap region. The panels on the left show results from standard DFT calculations, while the panels on the right present results with the DFT+$A-1/2$ correction. The conduction bands have been artificially scaled by a factor of 10 for better visualization. The panels correspond to: (a) α phase, (b) δ phase, (c) $\omega 1$ phase, (d) $\omega 2$ phase, and (e) $\omega 3$ phase.

Figure F.2 illustrates the behavior of the DOS after the QP correction and the d-level correction. In general, while these corrections lead to a narrowing of the energy distribution and a relative increase in the DOS at the VBM, no significant changes are observed in the DOS distribution of the other energy levels.

D.2 Dielectric and optical properties

The zero-crossing of the real part of the dielectric function ($\mathrm{Re}\,\varepsilon$) in the 13–20 eV range, computed using DFT+$A-1/2$ exhibited in Figure F.4, underscores critical optoelectronic behavior in the material. This energy range, spanning the ultraviolet to soft X-ray regime, signifies the bulk plasma frequency (ω_p), where collective electron oscillations (plasmons) dominate. At these energies, the material transitions from metallic reflectance ($\varepsilon < 0$) to dielectric transparency ($\varepsilon > 0$), enabling applications such as UV-transparent coatings or optical components for high-energy regimes. The DFT+$A-1/2$ method ensures precise modeling of electronic contributions, revealing how the zero-crossing arises from the interplay between free-electron (Drude-like) responses and interband transitions, consistent with Kramers-Kronig relations. The 13–20 eV result highlights the material's potential for plasmonic devices (e.g., UV sensors) or low-loss metamaterials in advanced photonics, particularly for extreme UV lithography or spectroscopy.

The Energy Loss Function (ELF) peaks observed consistently above 15 eV across all analyzed cases in Figure F.5 (right panels) are intrinsically tied to the high-energy electronic behavior of the material. These ELF peaks, which correspond to maxima in $\mathrm{Im}[-1/\varepsilon(\omega)]$, signify dominant collective electronic excitations–specifically bulk plasmons–and interband transitions within the 13–20 eV range. Such peaks reflect strong contributions from high-energy plasmonic oscillations and electronic transitions between deeper valence and conduction bands, while simultaneously indicating reduced optical losses in this spectral region. This low-loss characteristic makes the material promising for applications in high-energy regimes, such as UV photodetectors or next-generation photonic devices operating at extreme frequencies.

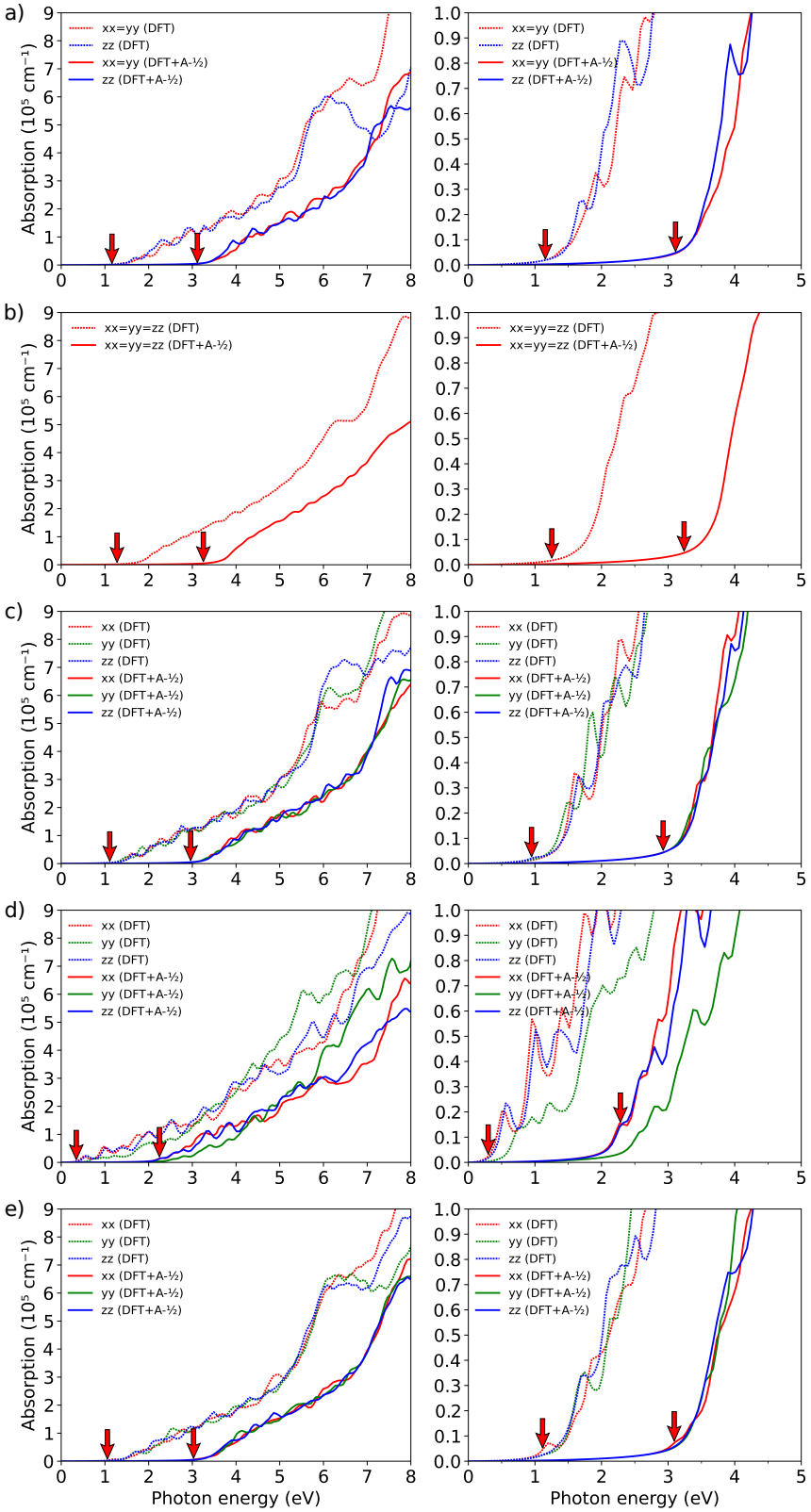

FIGURE D.3 – Absorption curves obtained using standard DFT (dashed lines) and DFT+$A-1/2$ correction (solid lines), along with an expanded view (right panels) providing a detailed look at the absorption in the region up to 5 eV. Direct band gaps are indicated by red arrows. The panels correspond to: (a) α phase, (b) δ phase, (c) $\omega 1$ phase, (d) $\omega 2$ phase, and (e) $\omega 3$ phase.

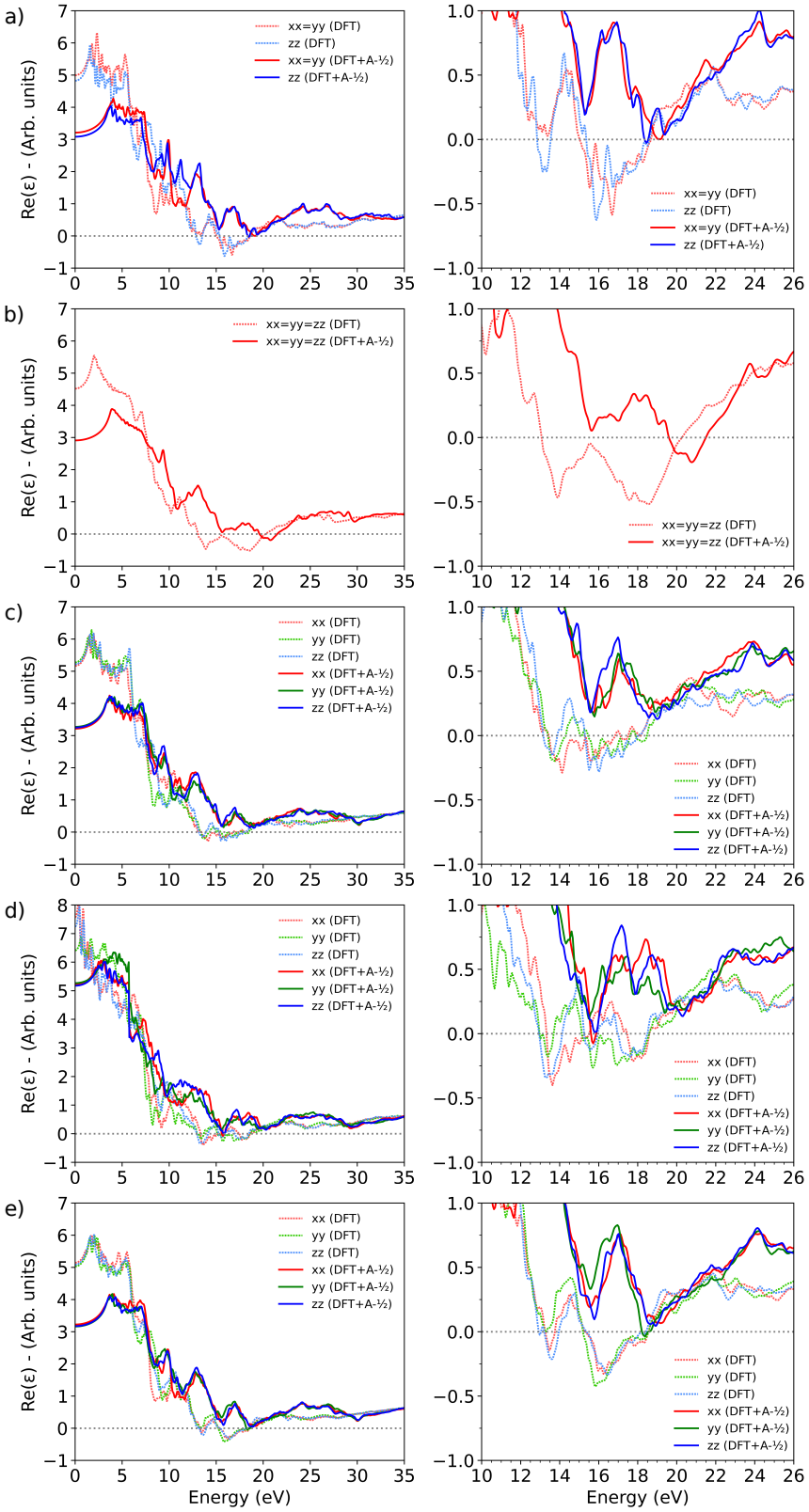

FIGURE D.4 – Components of the real part of the dielectric function for the five polymorphs. The left panels show zoomed-in views of the region where the function crosses zero. The panels correspond to: (a) α phase, (b) δ phase, (c) ω_1 phase, (d) ω_2 phase, and (e) ω_3 phase

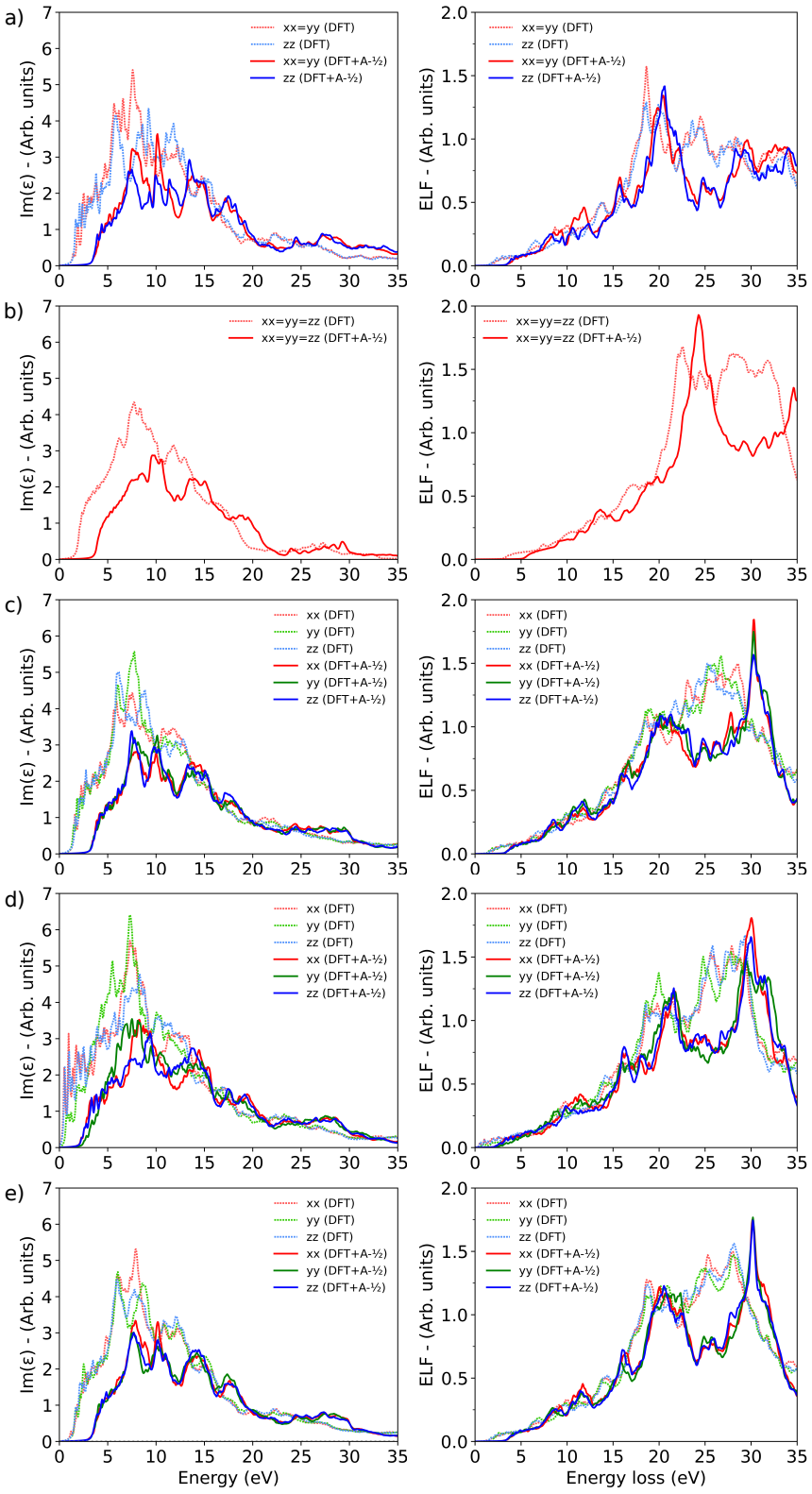

FIGURE D.5 – Components of the imaginary part of the dielectric function ($\mathrm{Im}\,\varepsilon$) for the five polymorphs (left panels) and the corresponding Electron Energy Loss Function (ELF), i.e., the $\mathrm{Im}[-1/\varepsilon(\omega)]$. The panels correspond to: (a) α phase, (b) δ phase, (c) ω_1 phase, (d) ω_2 phase, and (e) ω_3 phase

Appendix E - Supplementary informations of Ga_2O_3 polymorphs

This appendix provides supplemenatary informations about the results obtained for the Ga_2O_3 polymorphs.

E.1 Density of states

Figure F.1 illustrates the position of the d level before and after the DFT+A correction, where the DOS peak associated with the d level is shifted to align with experimental data. The deeper position of Ga 3d levels compared to In 4d levels is due to the stronger localization of Ga 3d orbitals. This difference primarily arises from two factors: the higher binding energy of Ga 3d electrons and, more importantly, their stronger hybridization with oxygen O 2p states.

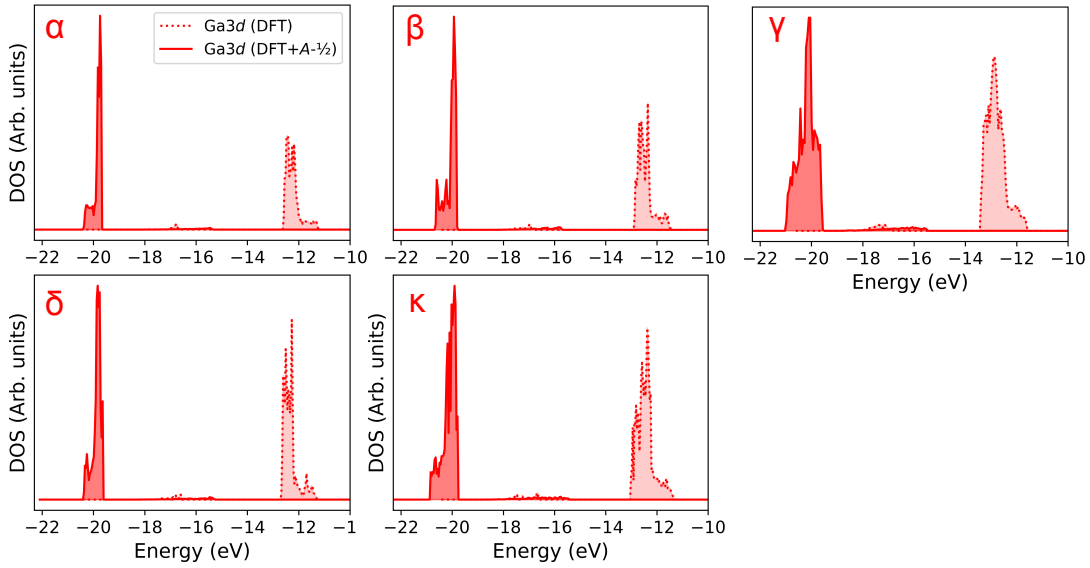

FIGURE E.1 – Density of states of the Ga 3d level calculated using standard DFT (light red, dashed line) and after the DFT+$A-1/2$ correction (red, solid lines). The labels for each polymorph are indicated in red in each panel.

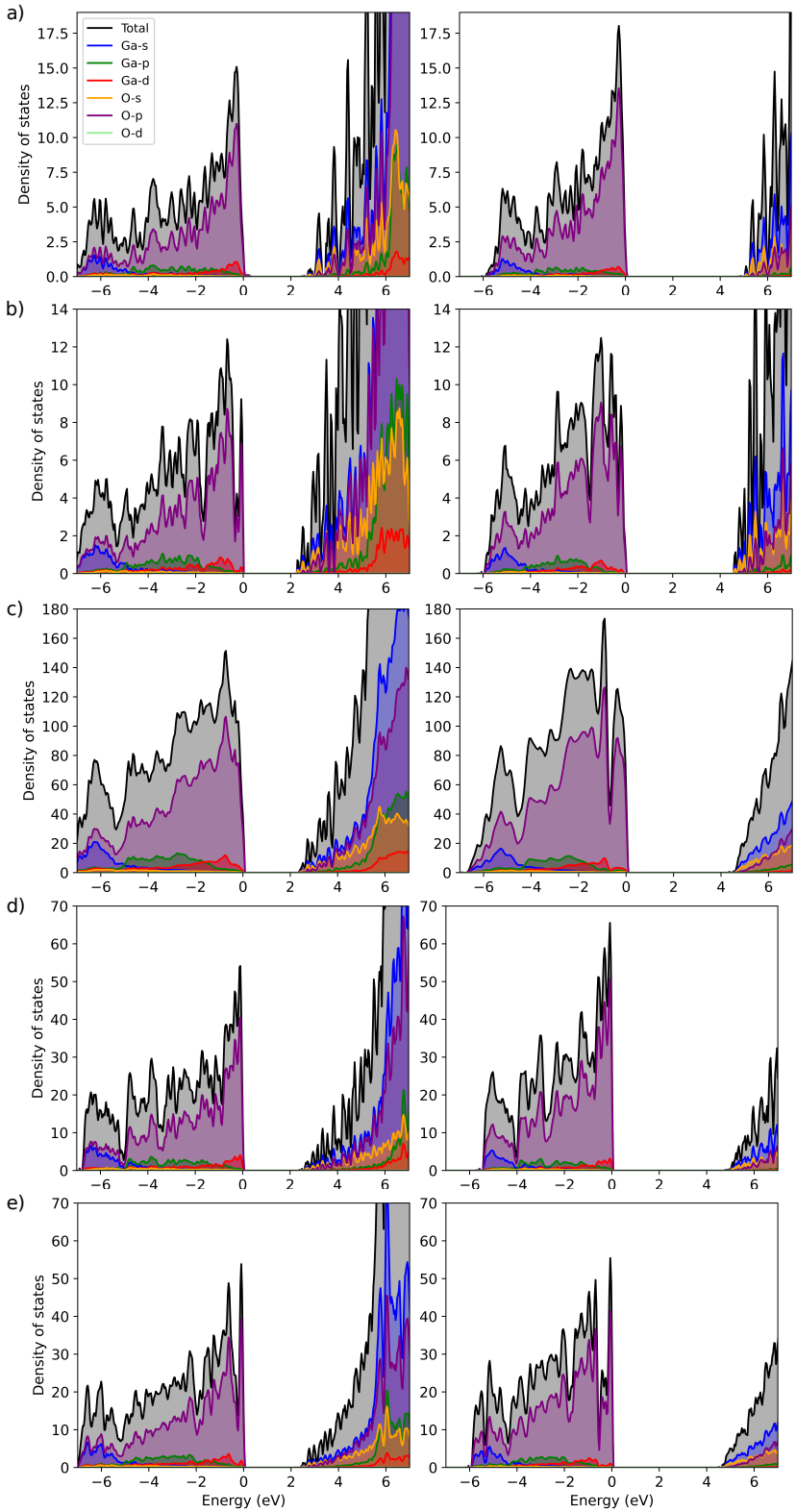

FIGURE E.2 – Density of states near the gap region. The panels on the left show results from standard DFT calculations, while the panels on the right present results with the DFT+$A-1/2$ correction. The conduction bands have been artificially scaled by a factor of 10 for better visualization. The panels correspond to: (a) α phase, (b) β phase, (c) γ phase, (d) δ phase, and (e) κ phase.

E.2 Dielectric and optical properties

The zero-crossing of the $\mathrm{Re}\,\varepsilon$ in high-energy regions, such as the 14–24 eV range calculated for Ga_2O_3 using the DFT+A − 1/2 method, plays a pivotal role in determining its optical and plasmonic properties. Compared to In_2O_3, Ga_2O_3 exhibits this crossover at significantly higher energies, a consequence of its wider electronic bandgap and stronger interband transitions. This higher energy range for Ga_2O_3 implies a correspondingly elevated plasma frequency (ω_p), marking its transition from metallic reflectance to dielectric transparency at deeper ultraviolet UV energies. Additionally, the 14–24 eV range suggests potential for exciting high-energy plasmonic modes, relevant for advanced spectroscopic techniques like electron energy-loss spectroscopy (EELS) or UV photodetection, distinguishing it from materials like In_2O_3, which operate at lower plasmonic energies. These results underscore highest-energy responses.

The high-energy ELF peaks at energies exceeding 20 eV, as determined via DFT+A − 1/2, and exhibited in Figure F.4, correspond to collective excitations of electrons (plasmons) or strong interband transitions, which dominate in this energy regime, reinforcing the material's high-energy response. These values are likely linked to bulk plasmon excitations or interband transitions involving deeper electronic states. These excitations require higher energy due to elevated bandgap and strong bonding between gallium and oxygen, which elevates the threshold for electronic transitions compared to narrower-gap oxides like In_2O_3. In the other hand, also suggest Ga_2O_3 supports plasmons in the extreme ultraviolet (EUV) or soft X-ray regimes, enabling applications in high-resolution spectroscopy (e.g., electron energy-loss spectroscopy, EELS) or radiation-hardened optical coatings. Simillarly, the suppression of low-energy plasmonic losses (due to fewer free carriers) enhances Ga_2O_3's suitability for high-frequency, high-power optoelectronic devices, such as UV photodetectors or transparent electrodes in harsh environments.

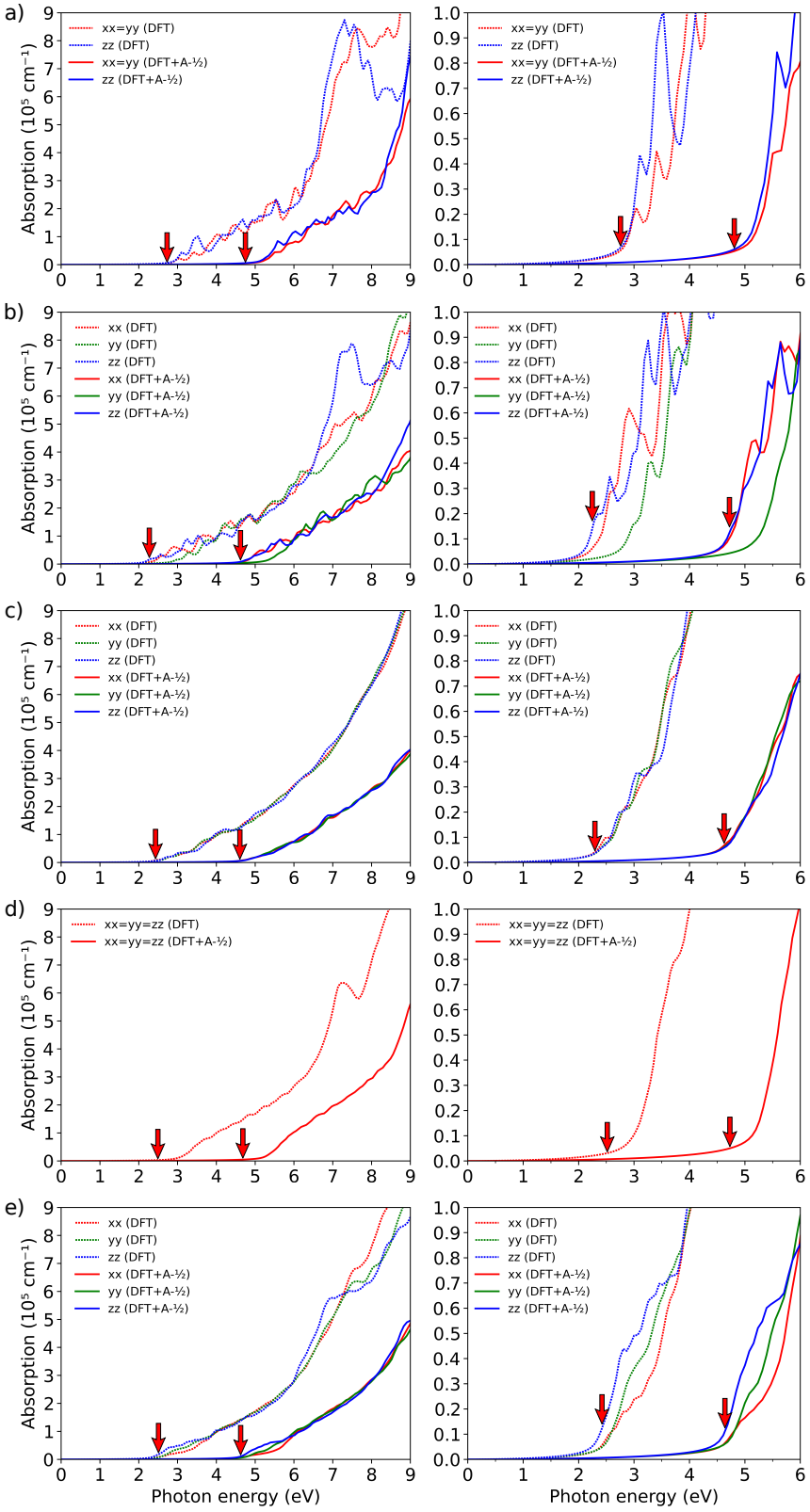

FIGURE E.3 – Absorption curves calculated using standard DFT (dashed lines) and the DFT+$A-1/2$ correction (solid lines) are presented, with an expanded view in the right panels highlighting the absorption features up to 5 eV. Red arrows indicate the direct band gaps. The panels correspond to (a) the α phase, (b) the β phase, (c) the γ phase, (d) the δ phase, and (e) the κ phase.

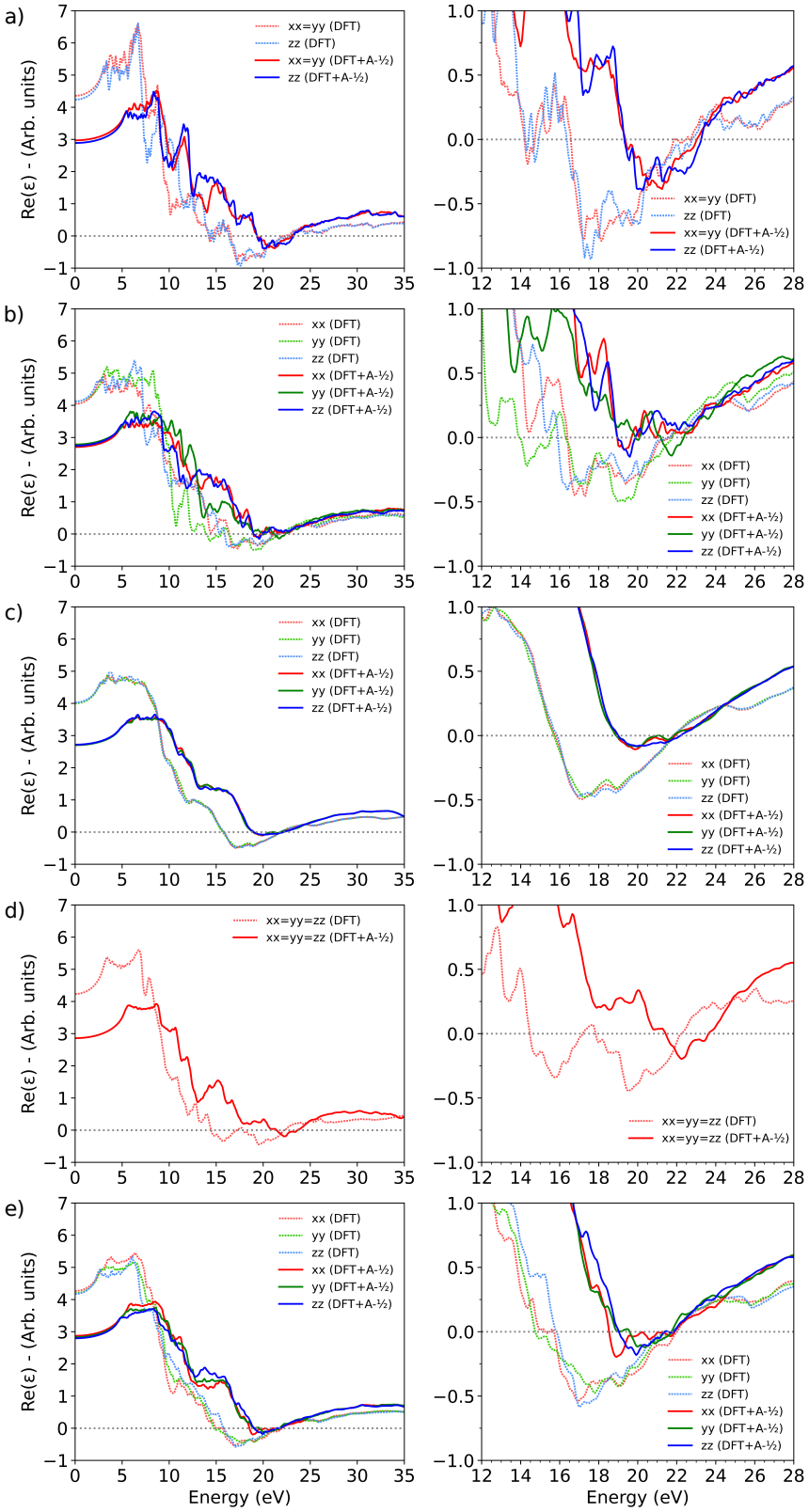

FIGURE E.4 – Components of the real part of the dielectric function for the five polymorphs. The left panels show zoomed-in views of the region where the function crosses zero. The panels correspond to: (a) α phase, (b) β phase, (c) γ phase, (d) δ phase, and (e) κ phase.

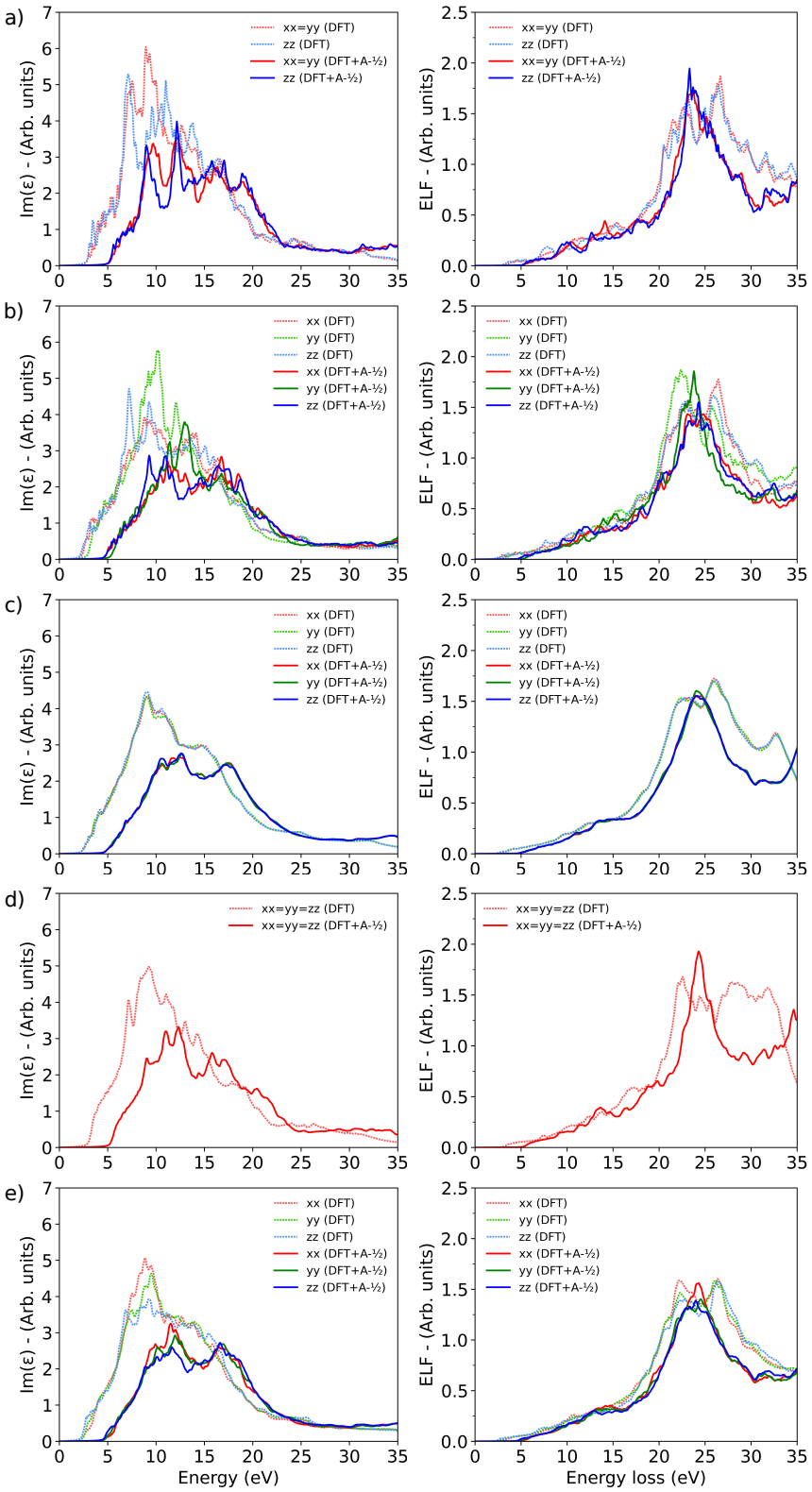

FIGURE E.5 – Components of the imaginary part of the dielectric function ($\mathrm{Im}\,\varepsilon$) for the five polymorphs (left panels) and the corresponding Electron Energy Loss Function (ELF), i.e., the $-\mathrm{Im}[1/\varepsilon(\omega)]$. The panels correspond to: (a) α phase, (b) δ phase, (c) ω_1 phase, (d) ω_2 phase, and (e) ω_3 phase

Appendix F - Supplementary informations of Al_2O_3 polymorphs

This appendix provides supplemenatary informations about the results obtained for the Al_2O_3 polymorphs.

F.1 Density of states

For Al_2O_3 polymorphs, only the QP correction is required. By analyzing their DOS, one can determine the contributions of specific atomic orbitals and elements to the overall electronic structure, gaining insight into the roles of oxygen and aluminum orbitals in shaping the valence and conduction bands. Figure F.1 highlights the similarities in the DOS of polymorphs with the same crystal structure or similar space groups, such as the resemblance between the α and α' phases, θ and $\theta 2$ phases, and $\omega 1$ and $\omega 2$ phases. Additionally, this analysis provides a visual comparison–beyond the electronic band structure–of how the QP correction increases the band gap from approximately 4.5–6 eV to over 7.6.

The VBM is predominantly influenced by oxygen states, which is mainly attributed to the bonding nature of the material. Oxygen's higher electronegativity leads to a stronger contribution from the oxygen $2p$ orbitals to the electronic structure, especially in the valence band, where bonding electrons are primarily localized on the oxygen atoms. The oxygen $2p$ orbitals are energetically closer to the Fermi level compared to the aluminum $3p$ orbitals, making them more involved in the formation of the valence band. Furthermore, the highly ionic bonding character of Al_2O_3, combined with the arrangement of oxygen atoms in the crystal lattice, further reinforces the dominance of oxygen states in the valence band. In contrast, aluminum plays a more significant role in the conduction band, where its $3s$ and $3p$ orbitals contribute more substantially to the electronic structure.

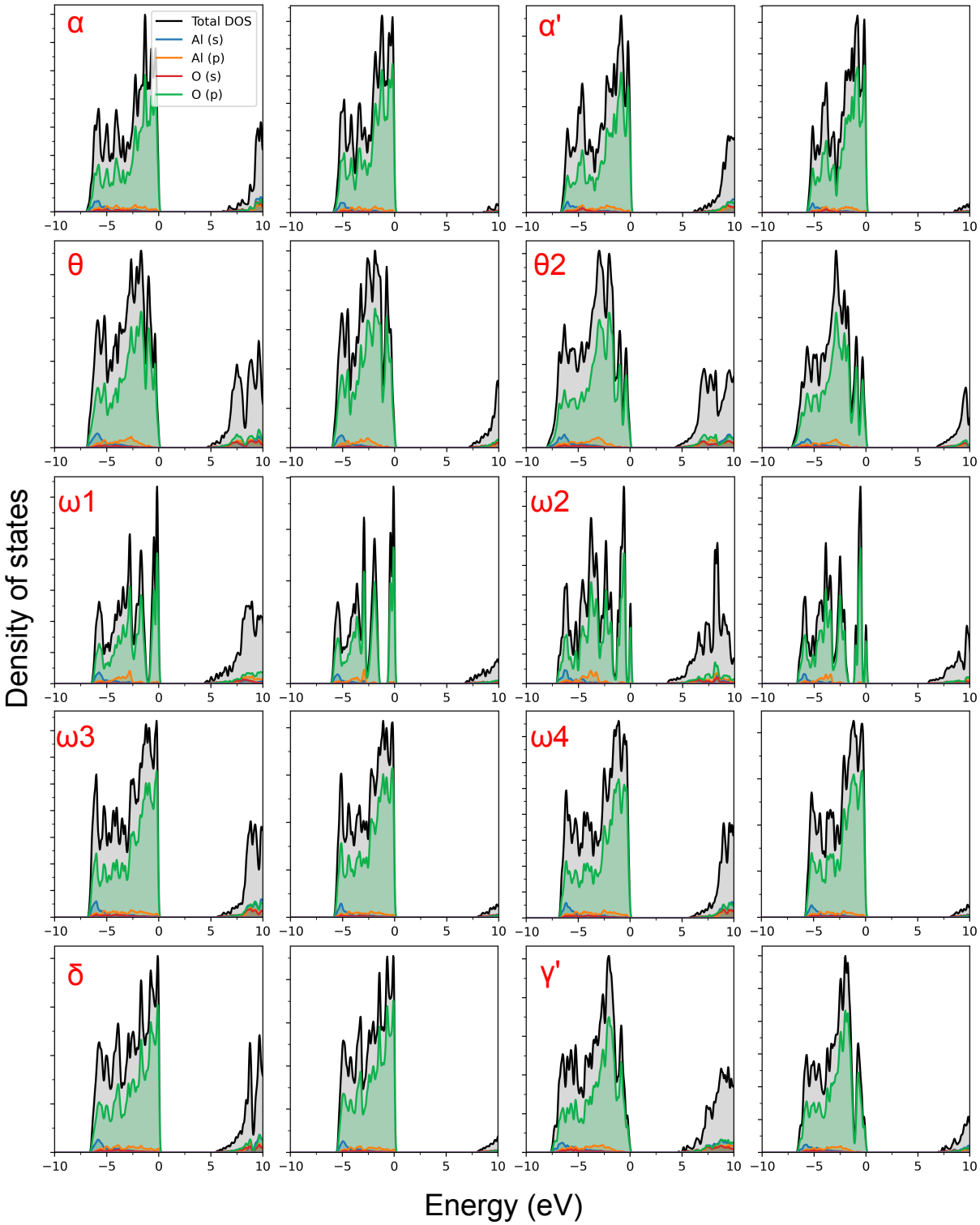

FIGURE F.1 – Density of states near the gap region for the ten dynamically stable Al_2O_3 polymorphs. The polymorphs are indicated by their labels in red. The panels with labels correspond to calculations using standard DFT, while the panels immediately to their right represent calculations using DFT−1/2.

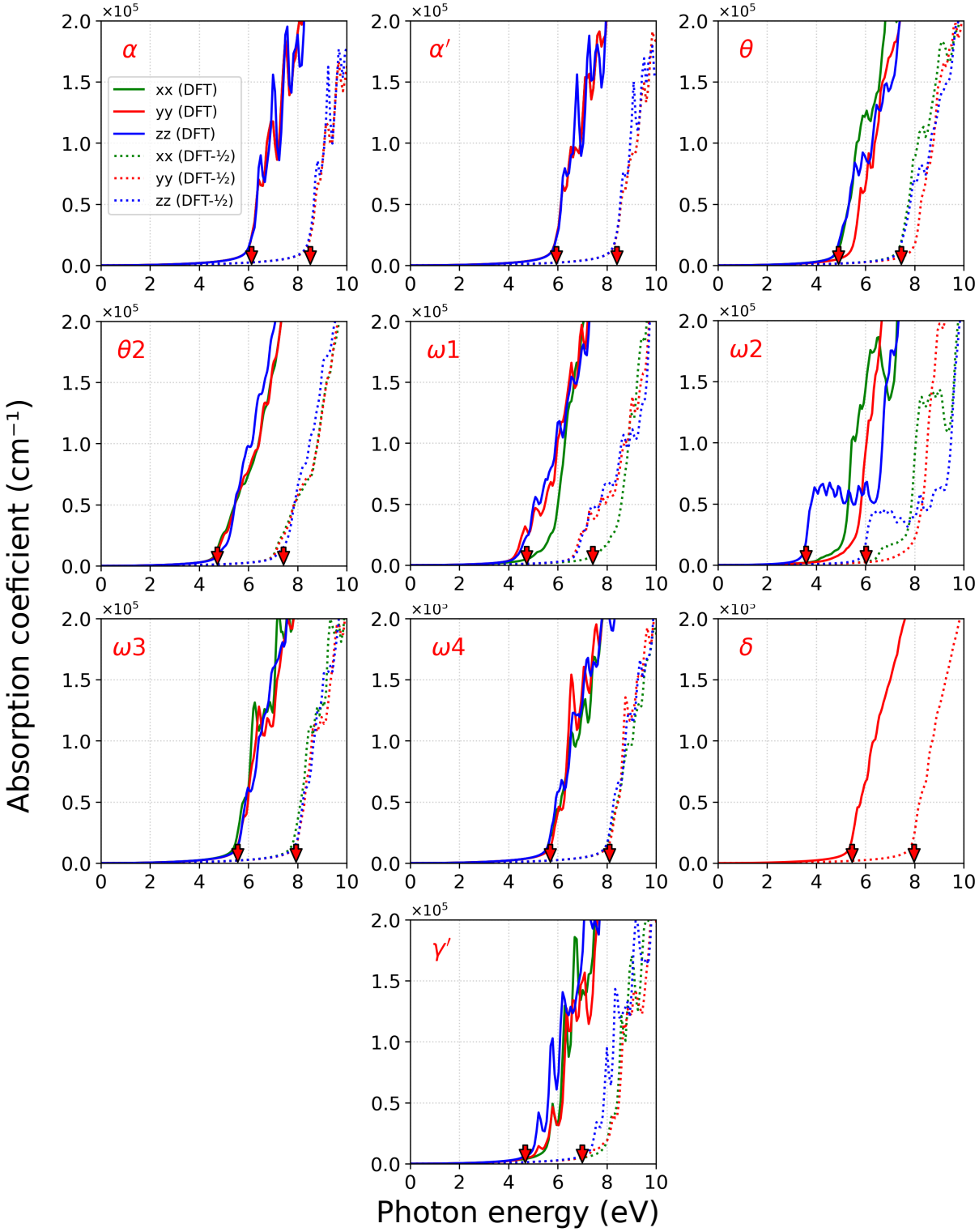

FIGURE F.2 – Absorption curves obtained using standard DFT (dashed lines) and DFT−1/2 correction (solid lines). Direct band gaps are indicated by red arrows. The polymorphs are indicated by their labels in red.

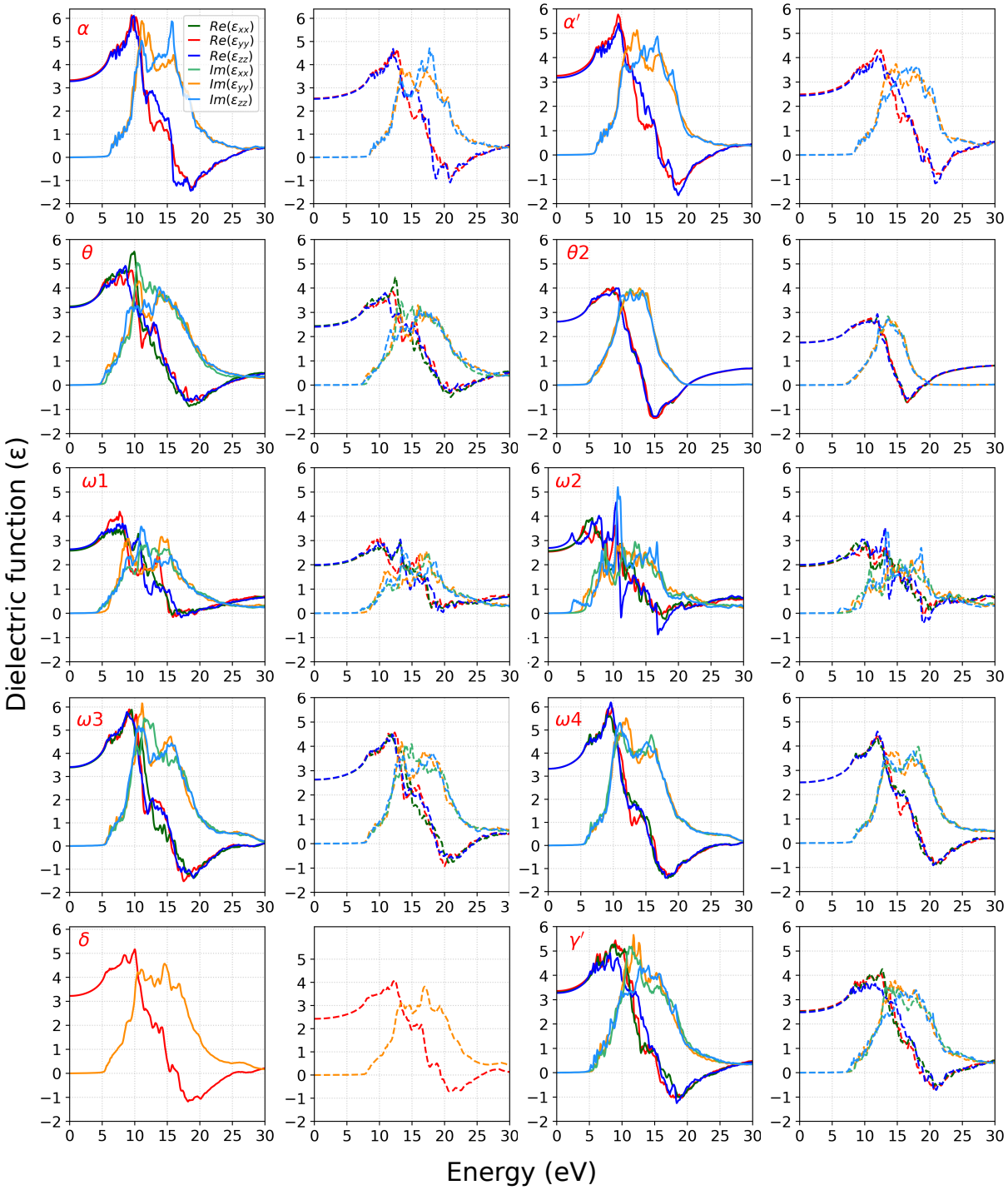

FIGURE F.3 – Real [Re (ω)] and imaginary [Im (ω)] components of the dielectric function for the ten dynamically stable polymorphs. Re (ω) is shown in dark green (xx), red (yy), and blue (zz), while Im (ω) is represented in green (xx), orange (yy), and light blue (zz). The labeled panels correspond to calculations using standard DFT (solid lines), whereas the adjacent panels to their right (dashed lines) depict calculations using DFT$-1/2$.

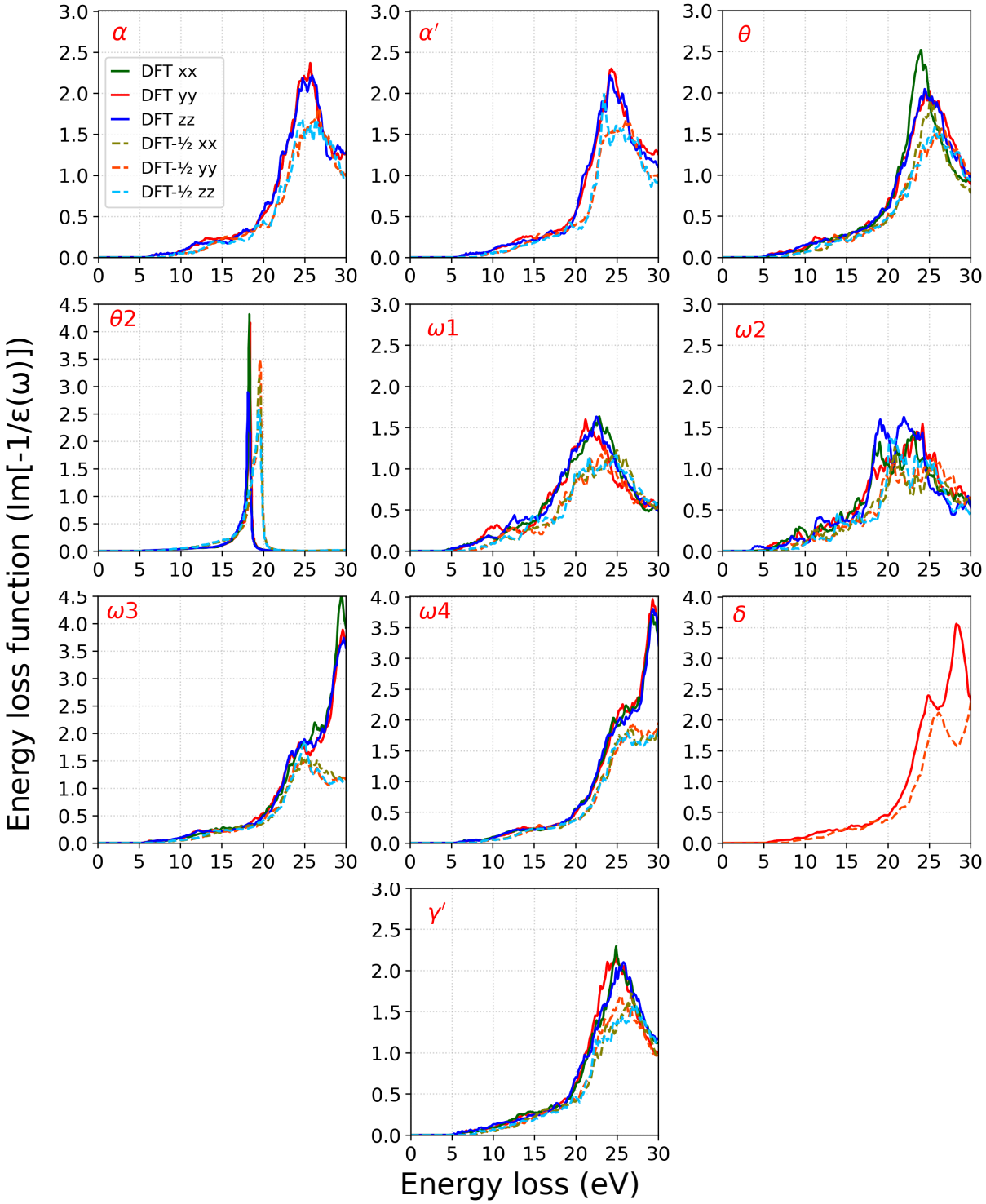

FIGURE F.4 – Components of the Electron Energy Loss Function (ELF) $\mathrm{Im}[-1/\varepsilon(\omega)]$ for the ten dynamically stable polymorphs. The components calculated using standard DFT are shown in dark green (xx), red (yy), and blue (zz), while those obtained with DFT$-1/2$ are represented in green (xx), orange (yy), and light blue (zz). The labeled panels correspond to standard DFT calculations (solid lines), whereas the adjacent panels to their right (dashed lines) represent the results from DFT$-1/2$.

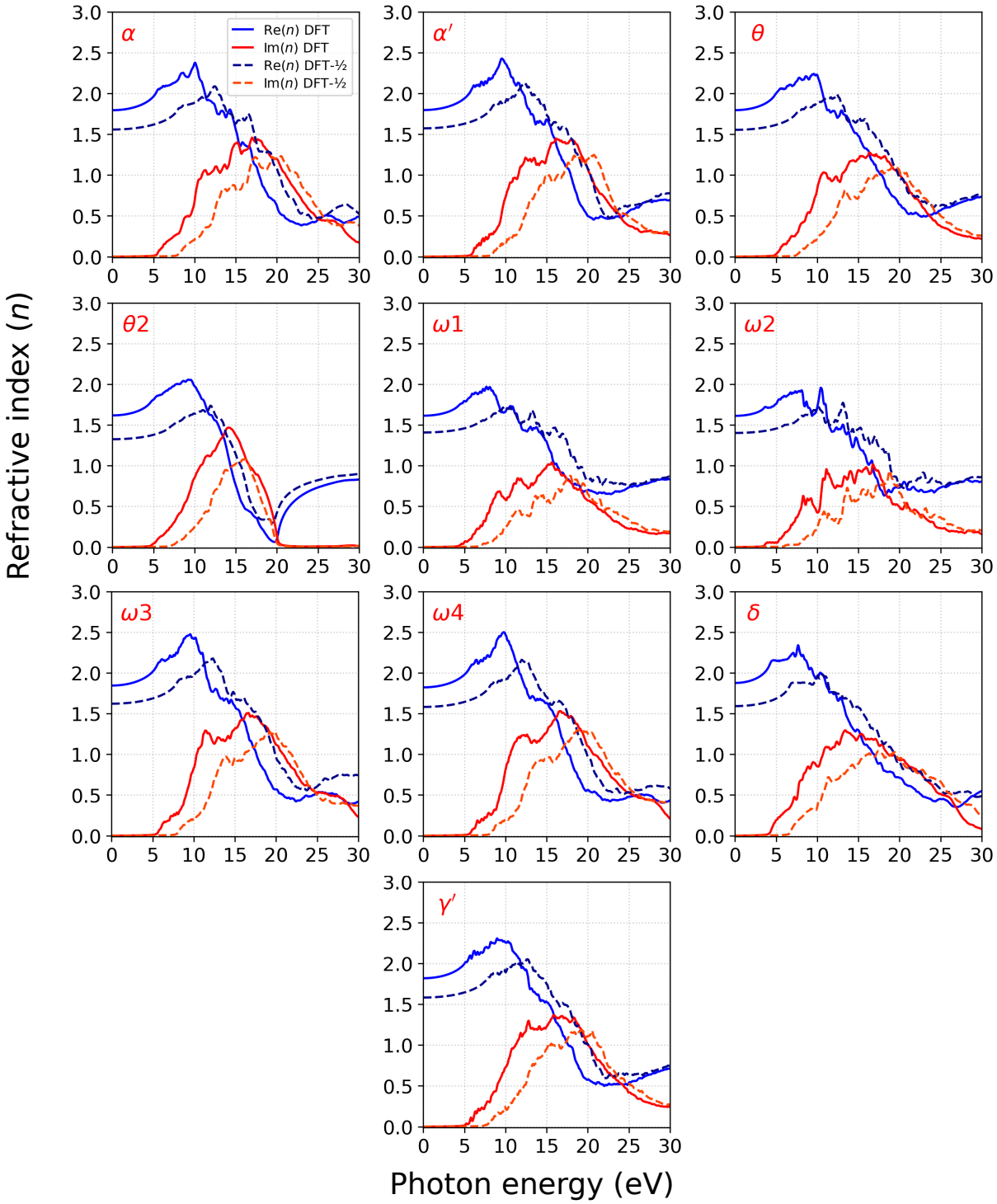

FIGURE F.5 – Average refractive index (n) for the ten dynamically stable polymorphs. The real part [Re (n)] is shown in blue and imaginary part [Im (n)] in red. Calculations using standard DFT are exhibited in solid lines, whereas the calculations using DFT$-1/2$ are depicted in dashed lines.

F.2 Dielectric and optical properties

The analysis of the absorption curves i Figure F.2 reveals anisotropy in all cases except for the unique cubic phase, which can be identified as thermodynamically stable, namely the δ phase. The absorptive regions preceding the red arrows indicating the gap are attributable to the applied Lorentzian broadening.

The curves of the real and imaginary components (Figure F.3) reflect the similarities between phases belonging to the same crystal system or similar space groups. In general, with the exception of the $\theta 2$, $\omega 1$, and $\omega 2$ phases, all other phases display similar functional behavior. Likewise, the zero crossings of $\mathrm{Re}, \varepsilon(\omega)$ are observed between 15 and 18 eV with standard DFT and between 17 and 21 eV with QP correction, except for the $\theta 2$ phase, where these values range from 14.5 to 15.5 eV without QP correction and from 16.5 to 17.5 eV with QP correction. This indicates that the $\theta 2$ phase may exhibit distinct screening properties or electron correlation effects compared to the other phases, suggesting a different degree of electronic localization or hybridization that merits further investigation.

Similarly, the analysis of the electron loss function (ELF) in Figure F.4 reveals peaks around 25 eV for the α, α', and θ' phases when computed with standard DFT, and around 27 eV with QP correction. This suggests that these phases possess characteristic electronic transitions or bonding interactions at these energies, likely reflecting a subtle balance between ionic and covalent contributions to the bonding environment.

In the $\omega 3$, $\omega 4$, and δ phases, these ELF peaks are found near 28 eV with standard DFT and shift to beyond 30 eV with QP correction, indicating that the application of QP corrections systematically modifies the energy landscape, likely by enhancing the electron-electron interaction effects and altering the screening response of the system.

On the other hand, for the $\omega 1$ and $\omega 2$ phases, standard DFT calculations show more pronounced anisotropy, with ELF peaks occurring between 22 and 24 eV in the $\omega 1$ phase and between 17 and 28 eV in the $\omega 2$ phase. With QP correction, these peaks are shifted to approximately 23–25 eV in the $\omega 1$ phase and 20–25 eV in the $\omega 2$ phase. In the case of the $\theta 2$ phase, the peak is considerably more pronounced than in the other phases, occurring around 17 eV and 19 eV when using DFT$-1/2$. These findings suggest that the $\theta 2$ phase may have a more complex or stronger localization of electronic states, which could influence its optical and electronic properties, warranting further detailed study to clarify the underlying mechanisms.

The refractive indices presented in Figure F.5 without QP correction align more closely with the experimental values for sapphire (around 1.7), with the exception of the $\theta 2$, $\omega 1$, and $\omega 2$ phases, which exhibit lower n values–approximately 1.4 with QP correction and 1.6

without. Nonetheless, apart from these exceptions, the experimental reference consistently falls within the range of n obtained with and without the QP correction. These results imply that, while the QP correction tends to refine the optical properties by adjusting the electronic structure, it generally preserves the overall trend observed in experiments. This consistency reinforces the validity of the theoretical approach for predicting the optical behavior of these phases, although further experimental and theoretical work is necessary to fully understand the discrepancies observed in the $\theta 2$, $\omega 1$, and $\omega 2$ phases.

Annex A - Published works

- Electronic and Optical Properties of Highly Complex Ga_2O_3 and In_2O_3 Polymorphs Using Approximate Quasiparticle DFT+$A-1/2$. Authors: C. R. Silva, F. Bechstedt, L. K. Teles, and M. Marques. J. Phys. Chem. C 2025, 129, 6, 3179–3198, https://doi.org/10.1021/acs.jpcc.4c06718. **Published** January 31, 2025.

- Phonons and Thermal Properties of α-, β-, δ-, and κ-Ga_2O_3 Polymorphs from First Principles Studies. Authors: C. R. Silva, F. Bechstedt, D. N. Freitas, L. K. Teles, and M. Marques. Submitted to Journal of Vacuum Science and Technology A on February 15, 2025. Current status: **Accepted** (JVA25-AR-GOX2025-00127).

- Pronounced Polymorphism of Alumina Al_2O_3: First-Principles Studies of 24 Crystal Structures on Stability, Lattice Vibrations and Thermal Properties. Authors: C. R. Silva, F. Bechstedt, L. K. Teles, R. N. Costa Filho and M. Marques. **To be submitted**.

- Dielectric, Optical and Excitonic Properties of 10 Thermodynamically Stable Al_2O_3 Polymorphs. Authors: C. R. Silva, F. Bechstedt, L. K. Teles, R. N. Costa Filho and M. Marques. **To be submitted**.

Annex B - Participation in scientific congresses and conferences

- Approximation of Quasi-particle Correction Applied to Ga_2O_3 and In_2O_3 and Their Polymorphs. Authors: C. R. Silva, F. Bechstedt, L. K. Teles, I. Guilhon, R. N. Costa Filho, and M. Marques. Congress: 2023 Autum Meeting of the Brazilian Physical Society. May 21 to 25, 2023, Ouro Preto/MG. Type: Poster presentation;

- First Principles Study of Electronic and Thermodynamic Properties of $(Ga_xIn_{1-x})_2O_3$ Alloys Using DFT-1/2 and GQCA. Authors: C. R. Silva, F. Bechstedt, L. K. Teles, I. Guilhon, R. N. Costa Filho, and M. Marques. Congress: 20th Brazilian Workshop on Semiconductor Physics (BWSP). September 12 to 16, 2023, São José dos Campos/SP Type: Poster presentation.

- First principles study of Ga_2O_3 and In_2O_3 polymorphs using approximate quasiparticle DFT+$A-1/2$ method. Authors: C. R. Silva, F. Bechstedt, L. K. Teles, and M. Marques. Congress: XVIII Brazilian School of Electronic Structure. October 8 to 11, 2023, Campinas/SP. Type: Poster presentation;

- Approximate Quasiparticle DFT+$A-1/2$ Method Applied to Ga_2O_3 and In_2O_3 Polymorphs. Authors: C. R. Silva, F. BechstedtL. K. Teles, and M. Marques. Authors: C. R. Silva, F. Bechstedt, L. K. Teles, and M. Marques. Congress: 2023 MRS (Materials Reseach Society) Fall Meeting (EL11: Ultra-Wide Bandgap Materials, Devices and Applications). December 5 to 7, 2023 - Virtual. Type: Oral presentation.

- First Principles Study of Structural, Electronic, and Optical Characteristics of Ga_2O_3 and In_2O_3 Polymorphs Using DFT+$A-1/2$ Quasiparticle Approximation for Power Electronics Applications. Authors: C. R. Silva, F. Bechstedt, L. K. Teles, and M. Marques. Congress: II Ibero-American Meeting on Quantum Materials and Electronic Structure (QMES). April 2 to 4, 2024, Vitória/ES. Type: Poster presentation;

- Phase transitions, Optical, and Electronic Properties of Ga_2O_3 and In_2O_3 polymorphs - A First-Principles-Based Study for Power Electronics. Authors: C. R. Silva, F. Bechstedt, L. K. Teles, and M. Marques. Congress: 2024 Autum Meeting of the Brazilian Physical Society. May 19 to 23, 2024, Florianópolis/SC. Type: Poster presentation;

Bibliography

ANDERSEN, O. K. Linear methods in band theory. **Phys. Rev. B**, American Physical Society, v. 12, p. 3060–3083, Oct 1975.

ANISIMOV, V. I.; ZAANEN, J.; ANDERSEN, O. K. Band theory and Mott insulators: Hubbard U instead of Stoner I. **Phys. Rev. B**, American Physical Society, v. 44, p. 943–954, Jul 1991.

ARMIENTO, R.; MATTSSON, A. E. Functional designed to include surface effects in self-consistent density functional theory. **Phys. Rev. B**, American Physical Society, v. 72, p. 085108, Aug 2005.

ASHCROFT, N.; MERMIN, N. **Solid State Physics**. [*S.l.*]: Holt, Rinehart and Winston, 1976. (HRW international editions).

ATAIDE, C. A.; PELÁ, R. R.; MARQUES, M.; TELES, L. K.; FURTHMÜLLER, J.; BECHSTEDT, F. Fast and accurate approximate quasiparticle band structure calculations of ZnO, CdO, and MgO polymorphs. **Phys. Rev. B**, American Physical Society, v. 95, p. 045126, Jan 2017.

BACHMANN, K. J.; HSU, F. S. L.; REMEIKA, J. P. The low temperature heat capacities of SnO_2 and In_2O_3. **Physica Status Solidi (a)**, v. 67, n. 1, p. K39–K42, 1981.

BARONI, S.; GIRONCOLI, S. de; CORSO, A. D.; GIANNOZZI, P. Phonons and related crystal properties from density-functional perturbation theory. **Rev. Mod. Phys.**, American Physical Society, v. 73, p. 515–562, Jul 2001.

BECHSTEDT, F. **Many-Body Approach to Electronic Excitations: Concepts and Applications**. [*S.l.*]: Springer Berlin Heidelberg, 2014. (Springer Series in Solid-State Sciences). ISBN 9783662445938.

BECKE, A. D. Density-functional exchange-energy approximation with correct asymptotic behavior. **Physical Review A**, APS, v. 38, n. 6, p. 3098, 1988.

BECKE, A. D. A new mixing of Hartree–Fock and Local Density Functional Theories. **The Journal of Chemical Physics**, American Institute of Physics, v. 98, n. 2, p. 1372–1377, 1993.

BEKHEET, M. F.; SCHWARZ, M. R.; LAUTERBACH, S.; KLEEBE, H.-J.; KROLL, P.; RIEDEL, R.; GURLO, A. Orthorhombic In_2O_3: A Metastable Polymorph of Indium Sesquioxide. **Angewandte Chemie International Edition**, v. 52, n. 25, p. 6531–6535, 2013.

BLÖCHL, P. E. Projector augmented-wave method. **Phys. Rev. B**, American Physical Society, v. 50, p. 17953–17979, Dec 1994.

BOER, T. de; BEKHEET, M. F.; GURLO, A.; RIEDEL, R.; MOEWES, A. Band gap and electronic structure of cubic, rhombohedral, and orthorhombic in_2o_3 polymorphs: Experiment and theory. **Phys. Rev. B**, American Physical Society, v. 93, p. 155205, Apr 2016.

BORISOVA, T. M.; CASTRO, R. A. Mechanism of charge transport in $si/al_2o_3/al$ structures. **Journal of Physics: Conference Series**, v. 461, n. 1, p. 012017, aug 2013.

BORLIDO, P.; AULL, T.; HURAN, A. W.; TRAN, F.; MARQUES, M. A. L.; BOTTI, S. Large-Scale Benchmark of Exchange-Correlation Functionals for the Determination of Electronic Band Gaps of Solids. **Journal of Chemical Theory and Computation**, v. 15, n. 9, p. 5069–5079, 2019. Available at: https://doi.org/10.1021/acs.jctc.9b00322.

BORN, M.; HUANG, K. **Dynamical Theory of Crystal Lattices**. [*S.l.*]: Oxford: Clarendon Press, 1988. (International series of monographs on physics). ISBN 9780198503699.

BÖTTGER, H. **Principles of the Theory of Lattice Dynamics**. [*S.l.*]: Weinheim: Physik-Verlag, 1983. ISBN 9783876640648.

BURKE, K.; WAGNER, L. O. DFT in a nutshell. **International Journal of Quantum Chemistry**, v. 113, n. 2, p. 96–101. Available at: https://onlinelibrary.wiley.com/doi/abs/10.1002/qua.24259.

CALZOLARO, A.; MIKOLAJICK, T.; WACHOWIAK, A. Status of Aluminum Oxide Gate Dielectric Technology for Insulated-Gate GaN-Based Devices. **Materials**, v. 15, n. 3, 2022. ISSN 1996-1944.

CAPELLE, K. A bird's-eye view of density-functional theory. **Brazilian Journal of Physics**, Sociedade Brasileira de Física, v. 36, n. 4a, p. 1318–1343, Dec 2006. ISSN 0103-9733.

CARVALHO, L. C. de; SCHLEIFE, A.; BECHSTEDT, F. Influence of exchange and correlation on structural and electronic properties of AlN, GaN, and InN polytypes. **Phys. Rev. B**, American Physical Society, v. 84, p. 195105, Nov 2011.

CHAIWONG, C.; YU, L.; SCHINARAKIS, K.; VILAITHONG, T. Optical property modification of ruby and sapphire by n-ion implantation. **Surface and Coatings Technology**, v. 196, n. 1, p. 108–112, 2005.

CHOI, J. I.; KIM, H. S.; SHIN, Y. S.; JOHNSON, C.; FOMINA, N.; STALEY, R. P.-A.; LANG, C.; JANG, S. S. Electron-Transport Characteristics Through Aluminum Oxide (100) and (012) in a Metal-insulator-metal Junction System: Density Functional Theory: Nonequilibrium green function approach. **ACS Omega**, v. 5, n. 3, p. 1717–1724, 2020.

CHUNG, D. H.; SIMMONS, G. Pressure and Temperature Dependences of the Isotropic Elastic Moduli of Polycrystalline Alumina. **Journal of Applied Physics**, v. 39, n. 11, p. 5316–5326, Oct. 1968. ISSN 0021-8979.

COHEN, A. J.; MORI-SÁNCHEZ, P.; YANG, W. Fractional charge perspective on the band gap in density-functional theory. **Physical Review B**, APS, v. 77, n. 11, p. 115123, 2008.

CORTES-VEGA, F. D.; YANG, W.; ZARATE-MEDINA, J.; BRANKOVIC, S. R.; RAMíREZ, J. M. H.; HERNANDEZ, F. C. R. Room-temperature synthesis of χ-Al_2O_3 and ruby (α-Cr:Al_2O_3). **CrystEngComm**, Royal Society of Chemistry, v. 20, p. 3505–3511, 2018.

CROWLEY, J. M.; TAHIR-KHELI, J.; III, W. A. G. Resolution of the band gap prediction problem for materials design. **The journal of physical chemistry letters**, ACS Publications, v. 7, n. 7, p. 1198–1203, 2016.

ERVINE, G.; OSBORN, E. F. The system Al_2O_3-H_2O. **The Journal of Geology**, v. 59, n. 4, p. 381–394, 1951.

FAN, Q.; ZHAO, R.; ZHANG, W.; SONG, Y.; SUN, M.; SCHWINGENSCHLÖGL, U. Low-energy Ga_2O_3 polymorphs with low electron effective masses. **Phys. Chem. Chem. Phys.**, The Royal Society of Chemistry, v. 24, n. 11, p. 7045–7049, 2022.

FENEBERG, M.; NIXDORF, J.; LIDIG, C.; GOLDHAHN, R.; GALAZKA, Z.; BIERWAGEN, O.; SPECK, J. S. Many-electron effects on the dielectric function of cubic In_2O_3: Effective electron mass, band nonparabolicity, band gap renormalization, and burstein-moss shift. **Phys. Rev. B**, American Physical Society, v. 93, p. 045203, Jan 2016.

FENEBERG, M.; NIXDORF, J.; NEUMANN, M. D.; ESSER, N.; ARTÚS, L.; CUSCÓ, R.; YAMAGUCHI, T.; GOLDHAHN, R. Ordinary dielectric function of corundumlike α-ga_2o_3 from 40 mev to 20 ev. **Phys. Rev. Mater.**, American Physical Society, v. 2, p. 044601, Apr 2018.

FERMI, E. Un metodo statistico per la determinazione di alcune proprietà dell-atome. **Rend. Accad. Naz. Lincei**, v. 6, n. 602-607, p. 32, 1927.

FERREIRA, L. G.; MARQUES, M.; TELES, L. K. Approximation to density functional theory for the calculation of band gaps of semiconductors. **Phys. Rev. B**, American Physical Society, v. 78, p. 125116, Sep 2008.

FERREIRA, L. G.; MARQUES, M.; TELES, L. K. Slater half-occupation technique revisited: the LDA-1/2 and GGA-1/2 approaches for atomic ionization energies and band gaps in semiconductors. **AIP Advances**, v. 1, n. 3, p. 032119, 07 2011. ISSN 2158-3226. Available at: https://doi.org/10.1063/1.3624562.

FRIEDRICH, C.; BETZINGER, M.; SCHLIPF, M.; BLÜGEL, S.; SCHINDLMAYR, A. Hybrid functionals and GW approximation in the FLAPW method. **Journal of Physics: Condensed Matter**, IOP Publishing, v. 24, n. 29, p. 293201, Jul. 2012.

FUCHS, F.; BECHSTEDT, F. Indium-oxide polymorphs from first principles: Quasiparticle electronic states. **Phys. Rev. B**, American Physical Society, v. 77, p. 155107, Apr 2008.

FURTHMÜLLER, J.; BECHSTEDT, F. Quasiparticle bands and spectra of Ga_2O_3 polymorphs. **Phys. Rev. B**, American Physical Society, v. 93, p. 115204, Mar 2016.

GACHOVSKA, T. K.; HUDGINS, J. L. 5 - SiC and GaN Power Semiconductor Devices. *In*: RASHID, M. H. (Ed.). **Power Electronics Handbook (Fourth Edition)**. Fourth edition. [*S.l.*]: Butterworth-Heinemann, 2018. p. 95–155. ISBN 978-0-12-811407-0.

GAJDOŠ, M.; HUMMER, K.; KRESSE, G.; FURTHMÜLLER, J.; BECHSTEDT, F. Linear optical properties in the projector-augmented wave methodology. **Phys. Rev. B**, American Physical Society, v. 73, p. 045112, jan. 2006.

GARCíA-DOMENE, B.; SANS, J. A.; GOMIS, O.; MANJóN, F. J.; ORTIZ, H. M.; ERRANDONEA, D.; SANTAMARíA-PéREZ, D.; MARTíNEZ-GARCíA, D.; VILAPLANA, R.; PEREIRA, A. L. J.; MORALES-GARCíA, A.; RODRíGUEZ-HERNáNDEZ, P.; MUñOZ, A.; POPESCU, C.; SEGURA, A. Pbca-type In_2O_3: The High-Pressure Post-Corundum Phase at Room Temperature. **The Journal of Physical Chemistry C**, v. 118, n. 35, p. 20545–20552, 2014.

GOEDECKER, S.; MASCHKE, K. Transferability of pseudopotentials. **Phys. Rev. A**, American Physical Society, v. 45, p. 88–93, Jan 1992.

GUILLOD, T.; FAERBER, R.; ROTHMUND, D.; KRISMER, F.; FRANCK, C. M.; KOLAR, J. W. Dielectric Losses in Dry-Type Insulation of Medium-Voltage Power Electronic Converters. **IEEE Journal of Emerging and Selected Topics in Power Electronics**, v. 8, n. 3, p. 2716–2732, 2020.

GUO, Z.; VERMA, A.; WU, X.; SUN, F.; HICKMAN, A.; MASUI, T.; KURAMATA, A.; HIGASHIWAKI, M.; JENA, D.; LUO, T. Anisotropic thermal conductivity in single crystal β-gallium oxide. **Applied Physics Letters**, v. 106, n. 11, p. 111909, mar. 2015. ISSN 0003-6951.

HARSHA, G.; ABRAHAM, V.; ZGID, D. Challenges with relativistic gw calculations in solids and molecules. **Faraday Discussions**, The Royal Society of Chemistry, v. 254, p. 216–238, 2024.

HEDIN, L. New Method for Calculating the One-Particle Green's Function with Application to the Electron-Gas Problem. **Phys. Rev.**, American Physical Society, v. 139, p. A796–A823, Aug 1965.

HEDIN, L. On correlation effects in electron spectroscopies and the GW approximation. **Journal of Physics: Condensed Matter**, IOP Publishing, v. 11, n. 42, p. R489, 1999.

HIGASHIWAKI, M.; KAPLAR, R.; PERNOT, J.; ZHAO, H. Ultrawide bandgap semiconductors. **Applied Physics Letters**, v. 118, n. 20, p. 200401, May 2021. ISSN 0003-6951. Available at: https://doi.org/10.1063/5.0055292.

HILFIKER, M.; KILIC, U.; STOKEY, M.; JINNO, R.; CHO, Y.; XING, H. G.; JENA, D.; KORLACKI, R.; SCHUBERT, M. Anisotropic dielectric function, direction

dependent bandgap energy, band order, and indirect to direct gap crossover in α-$(Al_xGa_{1-x})_2O_3$ ($\leq x \leq$1). **Applied Physics Letters**, v. 121, n. 5, p. 052101, Aug. 2022. ISSN 0003-6951.

HIMMETOGLU, B.; FLORIS, A.; GIRONCOLI, S. de; COCOCCIONI, M. Hubbard-corrected DFT energy functionals: The LDA+U description of correlated systems. **International Journal of Quantum Chemistry**, v. 114, n. 1, p. 14–49.

HOHENBERG, P.; KOHN, W. Inhomogeneous Electron Gas. **Phys. Rev.**, American Physical Society, v. 136, p. B864–B871, Nov 1964.

HOUSECROFT, C.; SHARPE, A. **Inorganic Chemistry** . 5^{th} ed.. ed. [*S.l.*]: Pearson Deutschland, 2018. 1298 p.

HUANG, F.; ZHU, S.; WANG, F.; LI, T.; ZHENG, W. Can We Transform Any Insulators into Semiconductors? Theory, Strategy, and Example in ZnO. **Matter**, v. 2, n. 5, p. 1091–1105, 2020. ISSN 2590-2385.

ITO, H.; KANEKO, K.; FUJITA, S. Growth and Band Gap Control of Corundum-Structured α-$(AlGa)_2O_3$ Thin Films on Sapphire by Spray-Assisted Mist Chemical Vapor Deposition. **Japanese Journal of Applied Physics**, v. 51, n. 10R, p. 100207, Oct. 2012.

JANAK, J. F. Proof that $\frac{\partial e}{\partial n_i} = \varepsilon$ in density-functional theory. **Phys. Rev. B**, American Physical Society, v. 18, p. 7165–7168, Dec. 1978.

JEURGENS, L. P. H.; SLOOF, W. G.; TICHELAAR, F. D.; MITTEMEIJER, E. J. Growth kinetics and mechanisms of aluminum-oxide films formed by thermal oxidation of aluminum. **Journal of Applied Physics**, v. 92, n. 3, p. 1649–1656, 08 2002.

JUNIOR, M. E. T. S.; FREITAS, L. C. G. Power Electronics for Modern Sustainable Power Systems: Distributed Generation, Microgrids and Smart Grids–a Review. **Sustainability**, v. 14, n. 6, 2022. ISSN 2071-1050.

KATO, T.; NISHINAKA, H.; SHIMAZOE, K.; KANEGAE, K.; YOSHIMOTO, M. Demonstration of Bixbyite-Structured δ-Ga_2O_3 Thin Films Using β-Fe_2O_3 Buffer Layers by Mist Chemical Vapor Deposition. **ACS Applied Electronic Materials**, v. 5, n. 3, p. 1715–1720, 2023.

KHANDELWAL, V.; RAJBHAR, M. K.; GARCíA, G. I. M.; TANG, X.; SARKAR, B.; LI, X. Demonstration of β-Ga_2O_3 nonvolatile flash memory for oxide electronics. **Japanese Journal of Applied Physics**, IOP Publishing, v. 62, n. 6, p. 060902, Jun. 2023.

KING, P. D. C.; VEAL, T. D.; FUCHS, F.; WANG, C. Y.; PAYNE, D. J.; BOURLANGE, A.; ZHANG, H.; BELL, G. R.; CIMALLA, V.; AMBACHER, O.; EGDELL, R. G.; BECHSTEDT, F.; MCCONVILLE, C. F. Band gap, electronic structure, and surface electron accumulation of cubic and rhombohedral In_2O_3. **Phys. Rev. B**, American Physical Society, v. 79, p. 205211, May 2009.

KNEIß, M.; HASSA, A.; SPLITH, D.; STURM, C.; WENCKSTERN, H. von; LORENZ, M.; GRUNDMANN, M. Epitaxial Stabilization of Single Phase κ-$(In_xGa_{1-x})_2O_3$ Thin Films up to $x = 0.28$ on c-sapphire and κ-$Ga_2O_3(001)$ templates by tin-assisted VCCS-PLD. **APL Materials**, v. 7, n. 10, p. 101102, 10 2019. ISSN 2166-532X.

KNIGHT, S.; MOCK, A.; KORLACKI, R.; DARAKCHIEVA, V.; MONEMAR, B.; KUMAGAI, Y.; GOTO, K.; HIGASHIWAKI, M.; SCHUBERT, M. Electron effective mass in Sn-doped monoclinic single crystal β-gallium oxide determined by mid-infrared optical hall effect. **Applied Physics Letters**, v. 112, n. 1, p. 012103, jan. 2018.

KOHN, W.; SHAM, L. J. Self-Consistent Equations Including Exchange and Correlation Effects. **Phys. Rev.**, American Physical Society, v. 140, p. A1133–A1138, Nov. 1965.

KRESSE, G.; FURTHMÜLLER, J. Efficient iterative schemes for ab initio total-energy calculations using a plane-wave basis set. **Phys. Rev. B**, American Physical Society, v. 54, p. 11169–11186, Oct 1996.

KRESSE, G.; FURTHMüLLER, J. Efficiency of ab-initio total energy calculations for metals and semiconductors using a plane-wave basis set. **Computational Materials Science**, v. 6, n. 1, p. 15–50, 1996. ISSN 0927-0256.

KRESSE, G.; FURTHMüLLER, J.; HAFNER, J. Ab initio Force Constant Approach to Phonon Dispersion Relations of Diamond and Graphite. **Europhysics Letters**, v. 32, n. 9, p. 729, dec 1995.

KRESSE, G.; HAFNER, J. Ab initio molecular dynamics for liquid metals. **Phys. Rev. B**, American Physical Society, v. 47, p. 558–561, Jan 1993.

KRESSE, G.; HAFNER, J. Norm-conserving and ultrasoft pseudopotentials for first-row and transition elements. **Journal of Physics: Condensed Matter**, v. 6, n. 40, p. 8245, oct 1994.

LATIMER, K.; DWARAKNATH, S.; MATHEW, K.; WINSTON, D.; PERSSON, K. A. Evaluation of thermodynamic equations of state across chemistry and structure in the materials project. **npj Computational Materials**, v. 4, n. 1, p. 40, Jul 2018. ISSN 2057-3960.

LEE, C.; YANG, W.; PARR, R. G. Development of the Colle-Salvetti correlation-energy formula into a functional of the electron density. **Physical review B**, APS, v. 37, n. 2, p. 785, 1988.

LEVIN, I.; BRANDON, D. Metastable alumina polymorphs: Crystal structures and transition sequences. **Journal of the American Ceramic Society**, v. 81, n. 8, p. 1995–2012, 1998.

LI, P.; SHAN, X.; LIN, Y.; MENG, X.; MA, J.; WANG, Z.; ZHAO, X.; LI, B.; LIU, W.; XU, H.; LIU, Y. Tin Doping Induced High-Performance Solution-Processed Ga_2O_3 Photosensor toward Neuromorphic Visual System (adv. funct. mater. 46/2023). **Advanced Functional Materials**, v. 33, n. 46, p. 2370273, 2023.

LIESHOUT, R. van; MIN, M.; DOMINIK, C.; BROGI, M.; GRAAFF, T. de; HEKKER, S.; KAMA, M.; KELLER, C. U.; RIDDEN-HARPER, A.; WERKHOVEN, T. I. M. van. Dusty tails of evaporating exoplanets - II. physical modelling of the kic 12557548b light curve. **Astronomy & Astrophysics**, v. 596, p. A32, 2016.

MAIMAN, T. H. Stimulated optical radiation in ruby. **Nature**, v. 187, n. 4736, p. 493–494, 1960.

MATTSSON, A. E.; ARMIENTO, R.; PAIER, J.; KRESSE, G.; WILLS, J. M.; MATTSSON, T. R. The AM05 density functional applied to solids. **The Journal of Chemical Physics**, v. 128, n. 8, p. 084714, 02 2008. ISSN 0021-9606.

MAZUMDER, S. K.; VOSS, L. F.; DOWLING, K. M.; CONWAY, A.; HALL, D.; KAPLAR, R. J.; PICKRELL, G. W.; FLICKER, J.; BINDER, A. T.; CHOWDHURY, S.; VELIADIS, V.; LUO, F.; KHALIL, S.; AICHINGER, T.; BAHL, S. R.; MENEGHINI, M.; CHARLES, A. B. Overview of Wide/Ultrawide Bandgap Power Semiconductor Devices for Distributed Energy Resources. **IEEE Journal of Emerging and Selected Topics in Power Electronics**, v. 11, n. 4, p. 3957–3982, 2023.

MENGLE, K. A.; SHI, G.; BAYERL, D.; KIOUPAKIS, E. First-principles calculations of the near-edge optical properties of β-Ga_2O_3. **Applied Physics Letters**, v. 109, n. 21, p. 212104, 11 2016. ISSN 0003-6951.

MILISAVLJEVIC, I.; WU, Y. Current status of solid-state single crystal growth. **BMC Materials**, v. 2, n. 1, p. 2, Jan. 2020. ISSN 2524-8138.

MIYAZAKI, Y.; KORENAGA, J. A wet heterogeneous mantle creates a habitable world in the hadean. **Nature**, v. 603, n. 7899, p. 86–90, 2022.

NAKAMURA, S.; KRAMES, M. R. History of Gallium-Nitride-Based Light-Emitting Diodes for Illumination. **Proceedings of the IEEE**, v. 101, n. 10, p. 2211–2220, 2013.

NAVARRO-QUEZADA, A.; ALAMÉ, S.; ESSER, N.; FURTHMÜLLER, J.; BECHSTEDT, F.; GALAZKA, Z.; SKURIDINA, D.; VOGT, P. Near valence-band electronic properties of semiconducting β-Ga_2O_3 (100) single crystals. **Phys. Rev. B**, American Physical Society, v. 92, p. 195306, Nov. 2015.

NOVIKOV, Y.; GISMATULIN, A.; HALLAC, B.; ROIZIN, Y.; GRITSENKO, V. Bipolar charge transport and contact phenomena in Al_2O_3. **Thin Solid Films**, v. 781, p. 140004, 2023. ISSN 0040-6090.

OKUMURA, H. A roadmap for future wide bandgap semiconductor power electronics. **MRS Bulletin**, v. 40, n. 5, p. 439–444, 2015.

PARK, C. H.; KIM, J. Y.; SUNG, S.-J.; KIM, D.-H.; DO, Y. S. Design of Grating Al_2O_3 Passivation Structure Optimized for High-Efficiency Cu(In,Ga)Se_2 Solar Cells. **Sensors**, v. 21, n. 14, 2021.

PARLINSKI, K.; LI, Z. Q.; KAWAZOE, Y. First-principles determination of the soft mode in cubic ZrO_2. **Phys. Rev. Lett.**, American Physical Society, v. 78, p. 4063–4066, May 1997.

PAVESI, M.; FABBRI, F.; BOSCHI, F.; PIACENTINI, G.; BARALDI, A.; BOSI, M.; GOMBIA, E.; PARISINI, A.; FORNARI, R. ε-Ga_2O_3 epilayers as a material for solar-blind UV photodetectors. **Materials Chemistry and Physics**, v. 205, p. 502–507, 2018. ISSN 0254-0584.

PEARTON, S. J.; YANG, J.; CARY, P. H. I.; REN, F.; KIM, J.; TADJER, M. J.; MASTRO, M. A. A review of Ga_2O_3 materials, processing, and devices. **Applied Physics Reviews**, v. 5, n. 1, p. 011301, Jan. 2018.

PELÁ, R. R.; MARQUES, M.; FERREIRA, L. G.; FURTHMÜLLER, J.; TELES, L. K. GaMnAs: Position of Mn-d levels and majority spin band gap predicted from GGA-1/2 calculations. **Applied Physics Letters**, v. 100, p. 202408, 2012.

PERDEW, J. P.; BURKE, K.; ERNZERHOF, M. Generalized Gradient Approximation Made Simple. **Phys. Rev. Lett.**, American Physical Society, v. 77, p. 3865–3868, Oct 1996.

PERDEW, J. P.; ERNZERHOF, M.; BURKE, K. Rationale for mixing exact exchange with density functional approximations. **The Journal of chemical physics**, American Institute of Physics, v. 105, n. 22, p. 9982–9985, 1996.

PEREVALOV, T. V.; SHAPOSHNIKOV, A. V.; GRITSENKO, V. A.; WONG, H.; HAN, J. H.; KIM, C. W. Electronic structure of α-Al_2O_3: Ab initio Simulations and Comparison with Experiment. **JETP Letters**, v. 85, n. 3, p. 165–168, 2007.

PREISSLER, N.; BIERWAGEN, O.; RAMU, A. T.; SPECK, J. S. Electrical transport, electrothermal transport, and effective electron mass in single-crystalline In_2O_3 films. **Phys. Rev. B**, American Physical Society, v. 88, p. 085305, Aug 2013.

RAHM, M.; HOFFMANN, R.; ASHCROFT, N. W. Atomic and Ionic Radii of Elements 1–96. **Chemistry - A European Journal**, v. 22, n. 41, p. 14625–14632, 2016.

RATCLIFF, L. E.; OSHIMA, T.; NIPPERT, F.; JANZEN, B. M.; KLUTH, E.; GOLDHAHN, R.; FENEBERG, M.; MAZZOLINI, P.; BIERWAGEN, O.; WOUTERS, C.; NOFAL, M.; ALBRECHT, M.; SWALLOW, J. E. N.; JONES, L. A. H.; THAKUR, P. K.; LEE, T.-L.; KALHA, C.; SCHLUETER, C.; VEAL, T. D.; VARLEY, J. B.; WAGNER, M. R.; REGOUTZ, A. Tackling Disorder in γ-Ga_2O_3. **Advanced Materials**, v. 34, n. 37, p. 2204217, 2022.

ROUQUEROL, F.; ROUQUEROL, J.; SING, K. Adsorption by metal oxides. *In*: ROUQUEROL, F.; ROUQUEROL, J.; SING, K. (Ed.). **Adsorption by Powders and Porous Solids**. London: Academic Press, 1999. p. 287–354.

SAKAGUCHI, N.; TANDA, L.; KUNISADA, Y. Measurement of the dielectric function of α-Al_2O_3 by transmission electron microscopy – electron energy-loss spectroscopy without cerenkov radiation effects. **Ultramicroscopy**, v. 169, p. 37–43, 2016.

SAMSONIDZE, G.; PARK, C.-H.; KOZINSKY, B. Insights and challenges of applying the GW method to transition metal oxides. **Journal of Physics: Condensed Matter**, IOP Publishing, v. 26, n. 47, p. 475501, Oct. 2014.

SCHERER, V.; JANOWITZ, C.; KRAPF, A.; DWELK, H.; BRAUN, D.; MANZKE, R. Transport and angular resolved photoemission measurements of the electronic properties of In_2O_3 bulk single crystals. **Applied Physics Letters**, v. 100, n. 21, p. 212108, 2012.

SCHLEIFE, A.; FUCHS, F.; FURTHMÜLLER, J.; BECHSTEDT, F. First-principles study of ground- and excited-state properties of MgO, ZnO, and CdO polymorphs. **Phys. Rev. B**, American Physical Society, v. 73, p. 245212, Jun 2006.

SCHOBER, H.; STRAUCH, D.; DORNER, B. Lattice dynamics of sapphire (al_2o_3). **Zeitschrift für Physik B Condensed Matter**, v. 92, n. 3, p. 273–283, Sep 1993.

SCHUBERT, M.; KORLACKI, R.; KNIGHT, S.; HOFMANN, T.; SCHÖCHE, S.; DARAKCHIEVA, V.; JANZÉN, E.; MONEMAR, B.; GOGOVA, D.; THIEU, Q.-T.; TOGASHI, R.; MURAKAMI, H.; KUMAGAI, Y.; GOTO, K.; KURAMATA, A.; YAMAKOSHI, S.; HIGASHIWAKI, M. Anisotropy, phonon modes, and free charge carrier parameters in monoclinic β-gallium oxide single crystals. **Physical Review B**, American Physical Society, v. 93, n. 12, p. 125209, mar. 2016.

SHI, J.; ZHANG, J.; YANG, L.; QU, M.; QI, D.-C.; ZHANG, K. H. L. Wide Bandgap Oxide Semiconductors: from Materials Physics to Optoelectronic Devices. **Advanced Materials**, v. 33, n. 50, p. 2006230.

SHI, S.; QIAN, S.; HOU, X.; MU, J.; HE, J.; CHOU, X. Structural and Optical Properties of Amorphous Al_2o_3 Thin Film Deposited by Atomic Layer Deposition. **Advances in Condensed Matter Physics**, v. 2018, n. 1, p. 7598978, 2018.

SHI, W.; WEI, W.; SUN, N.; MAO, Z.; PRAKAPENKA, V. B. Thermal Equations of State of Corundum and Rh_2O_3 (II)-type Al_2O_3 up to 153 GPa and 3400 K. **Journal of Geophysical Research: Solid Earth**, v. 127, n. 4, p. e2021JB023805, 2022.

SILVA, C. R.; BECHSTEDT, F.; Kühl Teles, L.; MARQUES, M. Electronic and Optical Properties of Highly Complex Ga_2O_3 and In_2O_3 Polymorphs Using Approximate Quasiparticle DFT+$A-1/2$. **The Journal of Physical Chemistry C**, v. 129, n. 6, p. 3179–3198, 2025.

SLATER, J. C. The Self Consistent Field and the Structure of Atoms. **Phys. Rev.**, American Physical Society, v. 32, p. 339–348, Sep 1928.

SLOBODYAN, O.; FLICKER, J.; DICKERSON, J.; SHOEMAKER, J.; BINDER, A.; SMITH, T.; GOODNICK, S.; KAPLAR, R.; HOLLIS, M. Analysis of the dependence of critical electric field on semiconductor bandgap. v. 37, n. 4, 2 2022.

SOBOTTA, H.; NEUMANN, H.; KÜHN, G.; RIEDE, V. Infrared lattice vibrations of In_2O_3. **Crystal Research and Technology**, v. 25, n. 1, p. 61–64, 1990.

SPENCER, J. A.; MOCK, A. L.; JACOBS, A. G.; SCHUBERT, M.; ZHANG, Y.; TADJER, M. J. A review of band structure and material properties of transparent conducting and semiconducting oxides: Ga_2O_3, Al_2O_3, In_2O_3, ZnO, SnO_2, CdO, NiO, CuO, and Sc_2O_3. **Applied Physics Reviews**, v. 9, n. 1, p. 011315, 03 2022.

STEPHENS, P. J.; DEVLIN, F. J.; CHABALOWSKI, C. F.; FRISCH, M. J. Ab-initio calculation of vibrational absorption and circular dichroism spectra using density functional force fields. **The Journal of physical chemistry**, ACS Publications, v. 98, n. 45, p. 11623–11627, 1994.

SWALLOW, J. E. N.; VORWERK, C.; MAZZOLINI, P.; VOGT, P.; BIERWAGEN, O.; KARG, A.; EICKHOFF, M.; SCHöRMANN, J.; WAGNER, M. R.; ROBERTS, J. W.; CHALKER, P. R.; SMILES, M. J.; MURGATROYD, P.; RAZEK, S. A.; LEBENS-HIGGINS, Z. W.; PIPER, L. F. J.; JONES, L. A. H.; THAKUR, P. K.; LEE, T.-L.; VARLEY, J. B.; FURTHMüLLER, J.; DRAXL, C.; VEAL, T. D.; REGOUTZ, A. Influence of Polymorphism on the Electronic Structure of Ga_2O_3. **Chemistry of Materials**, v. 32, n. 19, p. 8460–8470, 2020.

TANG, Z.; YANG, Y.; BLAABJERG, F. Power electronics: The enabling technology for renewable energy integration. **CSEE Journal of Power and Energy Systems**, v. 8, n. 1, p. 39–52, 2022.

THOMAS, L. H. The calculation of atomic fields. **Mathematical Proceedings of the Cambridge Philosophical Society**, v. 23, n. 5, p. 542–548, 1927.

TOGO, A. First-principles Phonon Calculations with Phonopy and Phono3py. **J. Phys. Soc. Jpn.**, v. 92, n. 1, p. 012001, 2023.

TOGO, A.; CHAPUT, L.; TADANO, T.; TANAKA, I. Implementation strategies in Phonopy and Phono3py. **J. Phys. Condens. Matter**, v. 35, n. 35, p. 353001, 2023.

TSAO, J. Y.; CHOWDHURY, S.; HOLLIS, M. A.; JENA, D.; JOHNSON, N. M.; JONES, K. A.; KAPLAR, R. J.; RAJAN, S.; WALLE, C. G. Van de; BELLOTTI, E.; CHUA, C. L.; COLLAZO, R.; COLTRIN, M. E.; COOPER, J. A.; EVANS, K. R.; GRAHAM, S.; GROTJOHN, T. A.; HELLER, E. R.; HIGASHIWAKI, M.; ISLAM, M. S.; JUODAWLKIS, P. W.; KHAN, M. A.; KOEHLER, A. D.; LEACH, J. H.; MISHRA, U. K.; NEMANICH, R. J.; PILAWA-PODGURSKI, R. C. N.; SHEALY, J. B.; SITAR, Z.; TADJER, M. J.; WITULSKI, A. F.; WRABACK, M.; SIMMONS, J. A. Ultrawide-Bandgap Semiconductors: Research Opportunities and Challenges. **Advanced Electronic Materials**, v. 4, n. 1, p. 1600501, 2018.

VANDERBILT, D. Soft self-consistent pseudopotentials in a generalized eigenvalue formalism. **Phys. Rev. B**, American Physical Society, v. 41, p. 7892–7895, Apr 1990.

VINET, P.; FERRANTE, J.; ROSE, J. H.; SMITH, J. R. Compressibility of solids. **Journal of Geophysical Research: Solid Earth**, v. 92, n. B9, p. 9319–9325, 1987.

VISWANATHAN, R. Heat capacity of sapphire between 2 and 10 K by ac technique. **Journal of Applied Physics**, v. 46, n. 9, p. 4086–4087, sep 1975. ISSN 0021-8979.

WALUKIEWICZ, W.; ZIDE, J. M. O. Highly Mismatched Semiconductor Alloys: From Atoms to Devices. **Journal of Applied Physics**, v. 127, n. 1, p. 010401, 01 2020. ISSN 0021-8979.

WAN, T.; LIU, Y.; ZHOU, C.; CHEN, X.; LI, Y. Fabrication, properties, and applications of open-cell aluminum foams: A review. **Journal of Materials Science & Technology**, v. 62, p. 11–24, 2021.

WANG, C.-Y.; CHANG, S.-P.; HUANG, W.-L. Enhanced Ga_2O_3-based RRAM via stacked bilayer ZnO/Ga_2O_3. **ECS Advances**, IOP Publishing, v. 1, n. 2, p. 023501, jun 2022. Available at: https://dx.doi.org/10.1149/2754-2734/ac79bf.

WANG, X.; FAIZAN, M.; NA, G.; HE, X.; FU, Y.; ZHANG, L. Discovery of new polymorphs of gallium oxides with particle swarm optimization-based structure searches. **Advanced Electronic Materials**, v. 6, p. 2000119, may 2020.

WEN, M.; ABRAHAM, V.; HARSHA, G.; SHEE, A.; WHALEY, K. B.; ZGID, D. Comparing Self-Consistent GW and Vertex-Corrected G_0W_0 ($G_0W_0\gamma$) Accuracy for Molecular Ionization Potentials. **Journal of Chemical Theory and Computation**, v. 20, n. 8, p. 3109–3120, 2024.

WONG, M. H.; BIERWAGEN, O.; KAPLAR, R. J.; UMEZAWA, H. Ultrawide-bandgap semiconductors: An overview. **Journal of Materials Research**, v. 36, n. 23, p. 4601–4615, Dec.

YANG, J.; GASSE, K. V.; LUKIN, D. M.; GUIDRY, M. A.; AHN, G. H.; WHITE, A. D.; VUčKOVIĆ, J. Titanium:sapphire-on-insulator integrated lasers and amplifiers. **Nature**, v. 630, n. 8018, p. 853–859, June 2024. ISSN 1476-4687.

YOSHIOKA, S.; HAYASHI, H.; KUWABARA, A.; OBA, F.; MATSUNAGA, K.; TANAKA, I. Structures and energetics of Ga_2O_3 polymorphs. **Journal of Physics: Condensed Matter**, v. 19, n. 34, p. 346211, Jul. 2007.

ZHOU, H.; JI, Y.; WANG, Y.; FENG, K.; LUAN, B.; ZHANG, X.; CHEN, L.-Q. First-principles lattice dynamics and thermodynamic properties of α-, θ-, κ- and γ-Al_2O_3 and solid state temperature-pressure phase diagram. **Acta Materialia**, v. 263, p. 119513, 2024.

ZHU, R.; LIANG, H.; HU, S.; WANG, Y.; MEI, Z. Amorphous-Ga_2O_3 Optoelectronic Synapses with Ultra-low Energy Consumption. **Advanced Electronic Materials**, v. 8, n. 1, p. 2100741, 2022.

ZIMAN, J. **Electrons and Phonons: The Theory of Transport Phenomena in Solids**. [*S.l.*]: OUP Oxford, 2001. (International series of monographs on physics).

FOLHA DE REGISTRO DO DOCUMENTO

1. CLASSIFICAÇÃO/TIPO	2. DATA	3. REGISTRO N°	4. N° DE PÁGINAS
TD	23 de abril de 2025	DCTA/ITA/TD-007/2025	155

5. TÍTULO E SUBTÍTULO:

Theoretical study of electronic, optical, and thermodynamic properties of group IIIA sesquioxides In_2O_3, Ga_2O_3, Al_2O_3 , and their polymorphs.

6. AUTOR:

Claudio Ribeiro da Silva

7. INSTITUIÇÃO(ÕES)/ÓRGÃO(S) INTERNO(S)/DIVISÃO(ÕES):

Instituto Tecnológico de Aeronáutica – ITA

8. PALAVRAS-CHAVE SUGERIDAS PELO AUTOR:

Semiconductor Physics; First Principles Calculations; Density Functional Theory; Semiconducor Oxides; Computational Simulations; Solid-State Physics

9.PALAVRAS-CHAVE RESULTANTES DE INDEXAÇÃO:

Semicondutores; Teoria de densidade funcional; Óxidos; Estrutura eletrônica; Física do estado sólido; Física.

10. APRESENTAÇÃO: **(X) Nacional ( ) Internacional**

ITA, São José dos Campos. Curso de Doutorado. Programa de Pós-Graduação em Física. Área de Física Atômica e Molecular. Orientador: Prof. Dr. Marcelo Marques; coorientador: Prof. Dr. Raimundo Nogueira da Costa Filho. Defesa em 16/04/2025. Publicada em 2025.

11. RESUMO:

Transparent semiconducting oxides and insulating metal oxides, particularly wide and ultra-wide band gap transparent semiconductors, have gained significant academic interest for their potential in emerging technologies. Key research focuses include band gap engineering to tailor material properties, along with performance and availability, which enhance their technological relevance. This study employs first-principles calculations based on Density Functional Theory (DFT) to investigate the structural, electronic, optical, excitonic, and thermodynamic properties of In_2O_3, Ga_2O_3, and Al_2O_3 polymorphs. A known limitation of DFT is the underestimation of the band gap, particularly in semiconductors, which is further complicated in Ga_2O_3 and In_2O_3 due to delocalized *d* levels. Accurate quasiparticle corrections, such as GW and hybrid functionals, are computationally expensive, restricting their application to simpler polymorphs. Consequently, more comprehensive studies often overlook complex aspects of these materials. To overcome the challenges posed by polymorphism in these oxides, a combination of techniques is employed. Firstly, an analysis of structural and equilibrium parameters is conducted, followed by enthalpy calculations to investigate pressure-induced phase transitions. This approach reveals previously unreported phase transitions. In the second part, the DFT+A technique is used to correct the relative positions of the In 3*d* and Ga 3*d* levels in In_2O_3 and Ga_2O_3 polymorphs by adjusting a modified self-energy potential (V_S) to align with available experimental data. Using the principle of transferability, this potential is then applied to polymorphs for which no experimental data are yet available for the aforementioned levels. With this first approximation, the DFT−1/2 quasiparticle correction is applied to determine the energy band gaps. Combined, such approaches ensure an accurate description not only of the energy band gap but also of the electronic structure. Additionally, electronic, optical, and excitonic properties are extracted and compared with standard DFT calculations across all polymorphs. From the structural properties obtained in the first part, together with phonon calculations, the vibrational properties of the polymorphs are extracted, from which their dynamic stabilities are inferred. Similarly, important thermodynamic properties such as total free energy, vibrational entropy, and constant-volume heat capacity are derived, as well as their frequencies and Debye temperatures. Temperature-induced phase transitions, not previously identified in other works, are also observed. Finally, the results are compared across different oxides and similar structures to provide a broader perspective on how the combination of parameters related to the polymorphism of these materials governs their properties and serves as a foundation for various applications.

12. GRAU DE SIGILO:

(X) OSTENSIVO **( ) RESERVADO** **( ) SECRETO**